Geochemical evolution of the permeable-impermeable boundary within the Earth's crust revealed by silica precipitation

Graduate School of Environmental Studies, Tohoku University

Ph.D. thesis

GEOCHEMICAL EVOLUTION OF THE PERMEABLE-IMPERMEABLE BOUNDARY WITHIN THE EARTH'S CRUST REVEALED BY SILICA PRECIPITATION

シリカ鉱物析出による地殻の透水‐不透水境界の地球化学的発展

Geomaterial and Energy Laboratory

Solar and Terrestrial Systems and Energy Sciences

Graduate School of Environmental Studies, Tohoku University

B1GD1202 Hanae Saishu

January 20th, 2014

ABSTRACT

Silica is one of the dominant constituents of the Earth's crust. Silica minerals are generically called "silica polymorphs" that have the same chemical composition, SiO_2, but its crystal structure is different each other. Quartz is the most stable phase of silica in the Earth's crust and also a common mineral in hydrothermal veins. Diagenesis of silica polymorphs has been expected as the change of amorphous silica (opal-A) → cristobalite (opal-C/CT) → quartz. The transition zone of the rock strength is known as the brittle-plastic transition (BPT). Temperature at the BPT is mainly 300–450 °C. The boundaries of the seismic-aseismic and the permeable-impermeable zones correspond to the BPT. Ubiquitous occurrence of quartz vein is one of the evidences that the spatial and temporal variations in permeability within the Earth's crust are affected by silica precipitation in aqueous fluids. However, the role of dissolution and precipitation of silica minerals on fracture permeability and earthquakes is still unclear.

The hydrothermal flow-through experiments were conducted to investigate the temperature dependence and the effect of minor components in the solution on silica precipitation in the supercritical conditions of water. No rock/mineral substrate was set in the precipitation vessel. The experiments of temperature dependence revealed that large amount of silica precipitation occur only in supercritical condition at 24 and 31

MPa, whereas less precipitation of silica minerals occurs in liquid phase. Strong temperature dependence can be explained by the homogeneous nucleation of quartz in the surface energy of quartz, σ = 130 mJ/m^2. The experiments of minor components in the solution revealed that the dominant precipitates changes systematically with increasing Al concentration in the input solution from 0 to 29 mg/kg(H_2O): amorphous silica → cristobalite → quartz → albite and analcite. In the experiments of Al concentration in the input solution of 6 and 7 mg/kg(H_2O), no relics of precipitation of amorphous silica was found within quartz crystals. The precipitation rate increases with increasing of Al concentration in the input solution from 0 to 7 mg/kg(H_2O). The accompanying change in the solution chemistry and the composition of the precipitated products indicates that Al coupled with Na is incorporated into the silica minerals.

The empirical kinetic equation of overall silica-water interaction, including surface reaction of quartz and nucleation of silica minerals, was proposed. The first term of the new kinetic equation is the kinetic equation of surface reaction determined in the previous study. The parameters of nucleation rate order, a nucleation parameter, and the nucleation rate constant were derived by the hydrothermal flow-through experiments. Based on the precipitation experiments of flow rate, the nucleation-controlled precipitation of silica minerals is expressed in a first order rate equation. The nucleation

parameter is 1 only in the Si supersaturated solution with respect to quartz and in the supercritical conditions of water. The rate constant of nucleation is derived as a function of Al concentration in the solution. The experimental results of silica precipitation without rock/mineral substrates could be simulated well by the new kinetic equation.

The hydrological system within Earth's crust is divided into the permeable zone and the underlying, much less permeable zone. The Kakkonda geothermal field, Japan, has the well WD-1a that penetrated the boundary between the hydrothermal convection zone and the heat conduction zone. Calculation of quartz solubility along the well WD-1a revealed that the depth of a local minimum of quartz solubility correlates with that of the hydrological boundary at ~3100 m depth (380 °C, 24 MPa), in either case of hydrostatic conditions or of fluid pressure increase above hydrostatic at deeper levels. The results of the hydrothermal experiments of silica precipitation and the calculation of silica solubility in this study suggested that rapid quartz precipitation could occur via nucleation when fluids are brought from the liquid region to the supercritical region. The preferential precipitation of quartz at a specific depth plays a significant role in forming and sustaining the permeable-impermeable boundary in the Earth's crust.

Simulation of dissolution and precipitation of silica minerals along the well WD-1a of the Kakkonda geothermal field was conducted by using the new kinetic equation of

overall silica-water interaction derived in this study. Amount of dissolution and precipitation of silica minerals increases with decreasing of the fracture permeability from 1×10^{-9} to 1×10^{-13} m^2. The largest amount of silica precipitation could occur in the downward-fluid at 3150 m depth regardless of the permeability. At the shallower part, the time for fracture sealing at the fracture permeability of 1×10^{-13} m^2 correlates with the estimated ages in the previous studies of the Kakkonda geothermal field, whereas that at the permeable-impermeable boundary is ~100 times larger than the results in the previous works, indicating that the division of the permeable and impermeable area might occur at the early stage in the evolution of the Kakkonda geothermal field.

CONTENTS

NOMENCLATURE

Parameters

a_i	[-]	Activity of element *i*
A_{Qtz}	[m^2]	Interfacial area of quartz
A_x	[m^2]	Cross section area
b_i	[mol/kg]	Molality of component *i*
B	[-]	Frequency factor in the Arrhenius equation
$C_{i,in}$	[mg/kg(H_2O)]	Concentration of element *i* in the input solution
$C_{i,out}$	[mg/kg(H_2O)]	Concentration of element *i* in the output solution
C_i	[mg/kg(H_2O)]	Concentration of element *i* in the solution
$C_{Si,Qtz,eq}$	[mg/kg(H_2O)]	Solubility of quartz, Si
D	[cm^2/s]	Aqueous diffusion coefficient (10^{-5} cm^2/s)
d	[Å]	Molecular diameter of quartz (5 Å)
dC_i	[mg/kg(H_2O)]	Difference of concentration of element *i* between the input and output solution
dL	[m]	Distance between the start and the end points in the model of Kakkonda geothermal field
dP	[MPa]	Difference of pressure between the depth of the start and the end points
E_{act}	[kJ/mol]	Activation energy
E_{surf}	[ergs/cm^2]	Surface energy
I	[cm^{-3} s^{-1}]	Nucleation rate of quartz
k_N	[kg m^{-2} s^{-1}]	Reaction rate constant of nucleation
k_S	[kg m^{-2} s^{-1}]	Reaction rate constant of dissolution and precipitation on quartz surfaces

K	[-]	Equilibrium constant
M_{H_2O}	[kg]	Mass of water
m_{Si}	[mol/kg]	Molecular mass of Si (28.09 g/mol)
n	[-]	Reaction order of nucleation of silica minerals
P	[MPa]	Pressure
Q	[-]	Reaction quotient
Q_f	[m^3/s]	Flow rate
R	[J K^{-1} mol^{-1}]	Gas constant (8.31 J K^{-1} mol^{-1})
t	[sec]	Time
T	[K]	Temperature
V_{sp}	[cm^3/kg]	Specific volume of pure water
x	[km]	Depth
α	[-]	Nucleation parameter in the kinetic equation of the overall silica-water interaction
γ_i	[-]	Activity coefficient of component *i*
κ	[m^2]	Permeability
λ	[-]	Correlation coefficient in integrated methods
μ	[Pa s]	Viscosity
ρ_{H_2O}	[kg/m^3]	Density of water
σ_n	[MPa]	Normal stress
τ	[MPa]	Shear stress
υ	[cm^3/mol]	Molar volume of quartz (22.688 cm^3/mol)
Φ_i	[-]	Parameter as a function of temperature in the equation of quartz solubility (Fournier and Potter, 1982)

Ψ_i	[-]	Parameter as a function of temperature in the equation of quartz solubility (Manning, 1994)
Ω_{Qtz}	[-]	Si saturation ratio with respect to quartz (C_{Si} / $C_{Si,Qtz,eq}$)

Minerals and Rocks

Ab	Albite
AmSil, AS, A	Amorphous Silica (Opal-A)
Ah	Anhydrite
Anl	Analcite (Analcime)
C	Calcite
Qtz, Q	Quartz
Gr, G	Granite
Xtb, X	Cristobalite (Opal-C/CT)
Wk	Wairakite

Experiments

HAl	Precipitation experiments of high Al concentration in the input solution, $C_{Al,in}$ >10 mg/kg(H_2O). (section 2.4)
LAl	Precipitation experiments of low Al concentration in the input solution, $C_{Al,in}$ <10 mg/kg(H_2O). (section 2.4)
P24-Gr	Precipitation experiments of temperature dependence at 24 MPa. The input solution was made by dissolution of granite (Gr). (section 2.3)
P31-GA	Precipitation experiments of temperature dependence at 31 MPa. The input solution was made by dissolution of granite (G) mixed with amorphous silica (A). (section 2.3)
V_f	Precipitation experiments of flow rate. (section 3.3)

1. INTRODUCTION

1.1. Background

1.1.1. Universal observations of silica minerals

Silica (SiO_2) is one of the dominant constituents of the Earth's crust. The mass of the continental crust is 60.6 % silica (Rudnick and Gao, 2005). Silica minerals are generically called as "silica polymorphs" that have the same chemical composition, SiO_2, but its crystal structure is different each other (Mason and Moore, 1982). Silica polymorphs include quartz, tridymite, cristobalite, coesite, stishovite, and others depending on temperature and pressure (Mason and Moore, 1982; Fig. 1-1).

Among silica polymorphs, the most stable phase of silica in the Earth's crust is quartz (Fig. 1-1). Quartz is one of the main constituents of various igneous, sedimentary, and metamorphic rocks. Some rocks (i.e., quartzite, chert) are only composed of quartz. Quartz is also a common mineral in hydrothermal veins. Microcrystaline or cryptocrystaline quartz is called as calcedony. Textures of quartz vein are classified into four types: blocky, elongate-blocky, fibrous, and stretched crystal (Bons, 2000). Stretched-crystal veins and elongate (fibrous) veins show the epitaxial growth of quartz from the surfaces of quartz crystals in the wall rocks (Fig. 1-2a), whereas other veins filled by equant quartz grains are called as blocky veins (Fig. 1-2b) (Fisher and Brantley,

1992; Bons, 2000; Oliver and Bons, 2001; Morohashi *et al*., 2008; Okamoto *et al.*, 2008; Okamoto and Tsuchiya 2009).

Opal, the hydrated amorphous silica, is mainly classified into three types: opal-A, opal-CT, and opal-C. The composition of opal is usually quoted as $SiO_2 \cdot nH_2O$ where *n* is 0.5–2 implying that water is essential in opal (Smith, 1998). Opal-A is divided in two phases: opal-A_G is characterized by spherical structures with the silica linkage of gel-like (finite), and opal-A_N has the silica linkage of network-like (infinite). The X-ray pattern of opal-A is broad, whereas that of opal-CT and C shows a well-defined broad hump at $2\theta = 22°$ (Smith, 1998). Precipitation of opal, especially opal-A, occurs commonly in low-temperature surface environments such as hot springs (e.g., White *et al.*, 1956; Walter, 1976; Hinman and Lindstrom, 1996; Jones and Renaut, 2003; Lynne *et al.*, 2008), eukaryotes (plants, diatoms, and sponges) (e.g., Uriz *et al*, 2000; Weaver *et al*., 2003; Schröder *et al*., 2008), and marine sediments (e.g., Volpi *et al*., 2003; Neagu *et al*., 2009). Silica sinter is typically formed at hot spring with nearly neutral pH and alkali-chloride thermal waters, which is derived from deep reservoirs with temperatures >175 °C (Fournier and Rowe, 1966). Precipitation of non-crystalline opal-A occurs below 100 °C on biotic and abiotic surfaces (Guidry and Chafetz, 2003). Formation of silica deposits generally also occurs in the systems of the geothermal plants, which is

known as scale (Fig. 1-3). The production and the injection wells of the geothermal power station are sealed by silica precipitation, which is induced by changes in fluid temperature and/or pressure. The sealing of the facilities presents the serious problem for the utilization of geothermal energy (e.g., Yanagisawa, 2008).

Cristobalite and trydymite are one of the typical minerals of volcanic rocks. These are also formed commonly in industry due to high firing temperatures and dry environment. The occurrences of cristobalite and tridymite are metastable in terms of temperature and pressure of these crystallizations (Fig. 1-1). While some microcrystaline or cryptocrystaline quartz has been recognized as opal-C/CT (Frondel, 1962), the form of opal is hydrous and without distinct crystallites, whereas that of cristobalite is anhydrous and shows distinct crystallites (Smith, 1998). Coesite and stishovite are rare minerals that require high pressure (Fig. 1-1).

The diagenetic sequence of opal-A has been documented geologically (e.g., Siever, 1962; Mizutani, 1970). Opal-A is considered to transform to opal-CT → quartz, which follow the pathways of dissolution and re-precipitation (Williams *et al*., 1985). The transformation of silica follows the Ostwald step role, which is that the phase of higher entropy of amorphous silica changes to that of opal-C/CT and to that of lowest entropy of quartz (Robie *et al*., 1978; Williams and Crerar, 1985). The chert has been expected

to be largely replaced by crystalline quartz based on the observations of opal-CT to quartz conversion below ~170 °C in various geologic environments (e.g., Graetsch, 1994).

In this paper, the term “amorphous silica” and “cristobalite” is used for opal-A and opal-C/CT, respectively.

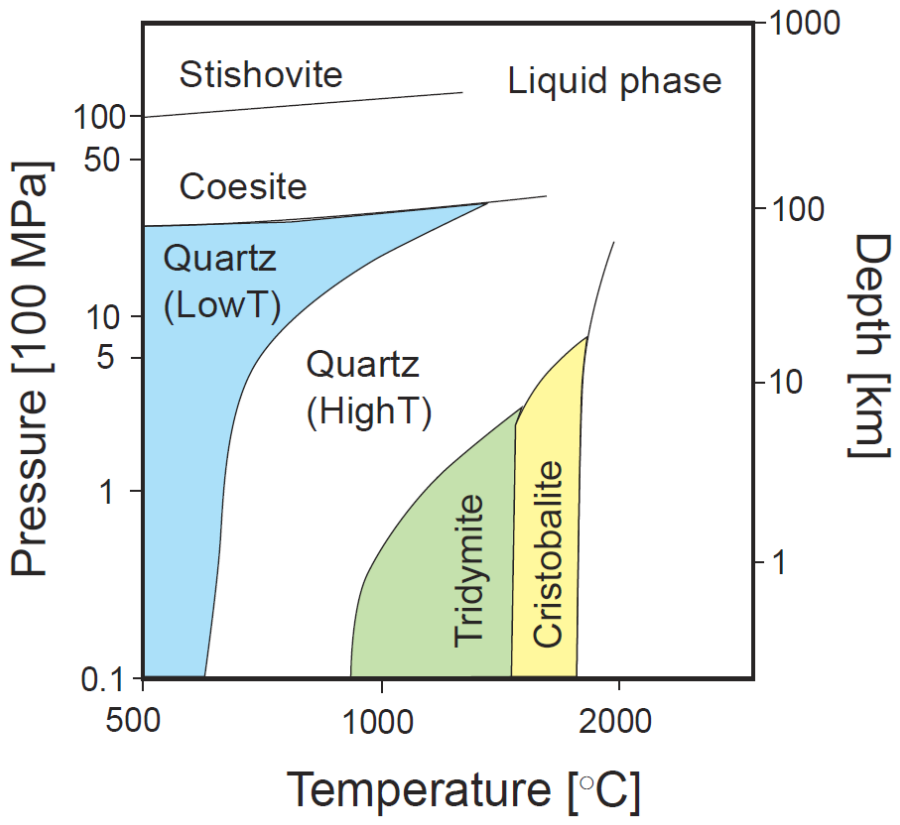

Figure 1-1 Silica (SiO_2) phase diagram (modified after Mason and Moore, 1982).

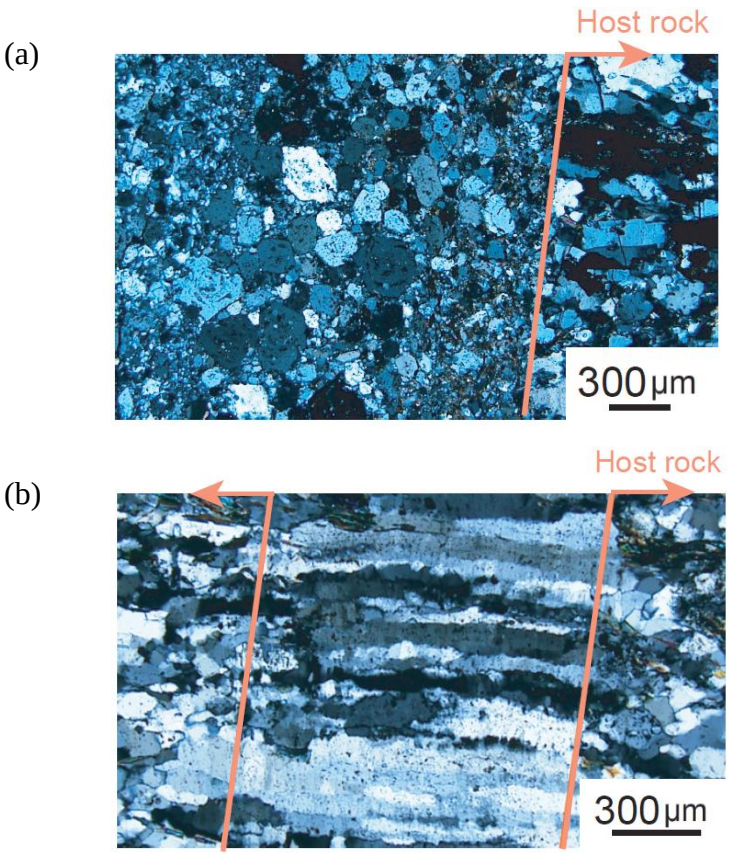

Figure 1-2 Quartz veins at the Sanbagawa metamorphic belt, Japan (modified after Okamoto *et al*., 2008). (a) Blocky texture and (b) stretched-crystal texture.

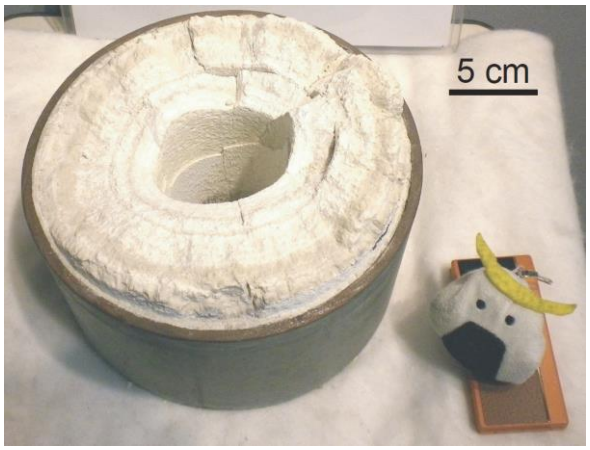

Figure 1-3 Silica scale of the Yamakawa geothermal plant, Kyusyu, Japan (displayed at the showroom of the Yamakawa geothermal plant, Japan).

1.1.2. The hydrological properties of the Earth's crust

Temperature and pressure increases with increasing depth in the crust cause the changes in the various physical and chemical properties of the Earth's crust. At shallow depths, fractures are interconnected to the earth's surface. Therefore, the fluid pressure gradient is hydrostatic (Fig. 1-4a). At deeper depths, in contrast, pore spaces are rarely connected, and a variety of mechanisms contribute to porosity reduction (Walder and Nur, 1984; Nur and Walder, 1990). Thus, at such depth, fluid pressure may be suprahydrostatic and lithostatic (Fig. 1-4a).

The crustal rocks undergo a transition in failure mode from localized brittle fracture to non-localized plastic flow (Fig. 1-4b), called the "Brittle-Plastic Transition (BPT)". The transition zone of the rock strength was marked as the intersection of the friction law and the plastic flow law, and at temperature around 300–450 °C for quartzo-feldspathic rocks (Brace and Kohlstedt, 1980; Kirby, 1980; Scholz, 2002; Fig. 1-4b). The BPT is generally located at depths from 10 to 20 km under typical geothermal gradient of the continental crust, 30 °C/km. However, the depth of the BPT depends on thermal gradient. For example, at NE Japan, the brittle zone of the inland is up to 20 km, whereas that at the volcanic area is above 10 km depth (Shimamoto, 1994).

The seismic and aseismic zones are also commonly found at the shallower and deeper part of the Earth's crust, respectively (Fig. 1-4c). Microseismicity has occurred at around the center of the brittle zone of NE Japan (Shimamoto, 1994; Fig. 1-4b, c). Most of the largest earthquakes in the continental crust nucleate at the bottom of the seismogenic layer in depths between 10 and 20 km, which has been interpreted by the model that the stresses can be released by brittle failure under high confining pressures and temperatures (Scholz, 2002).

Permeability is one of the important hydrological parameters of the Earth's crust because fluid migration plays a fundamental role in heat and mass transfer and crustal rheology. At greater depths in the crust, permeability tends to be lower than that at shallower part. The permeability of the continental crust is highly variable, approximately 16 orders of magnitude, from values as low as 10^{-23} m^2 in intact crystalline rock, intact shales, and fault gouge, to values as high as 10^{-7} m^2 in well-sorted gravels (Ingebritsen and Manning, 2002, 2010; Fig. 1-5). The transition from the permeable zone to the impermeable zone is also thought to correspond to the BPT (Ingebritsen and Manning, 2010; Weis *et al*., 2012; Fig. 1-5) because temperature is similar to that of the BPT (300–450 °C) in the field of the geothermal gradient, 30 °C/km, of the typical continental crust.

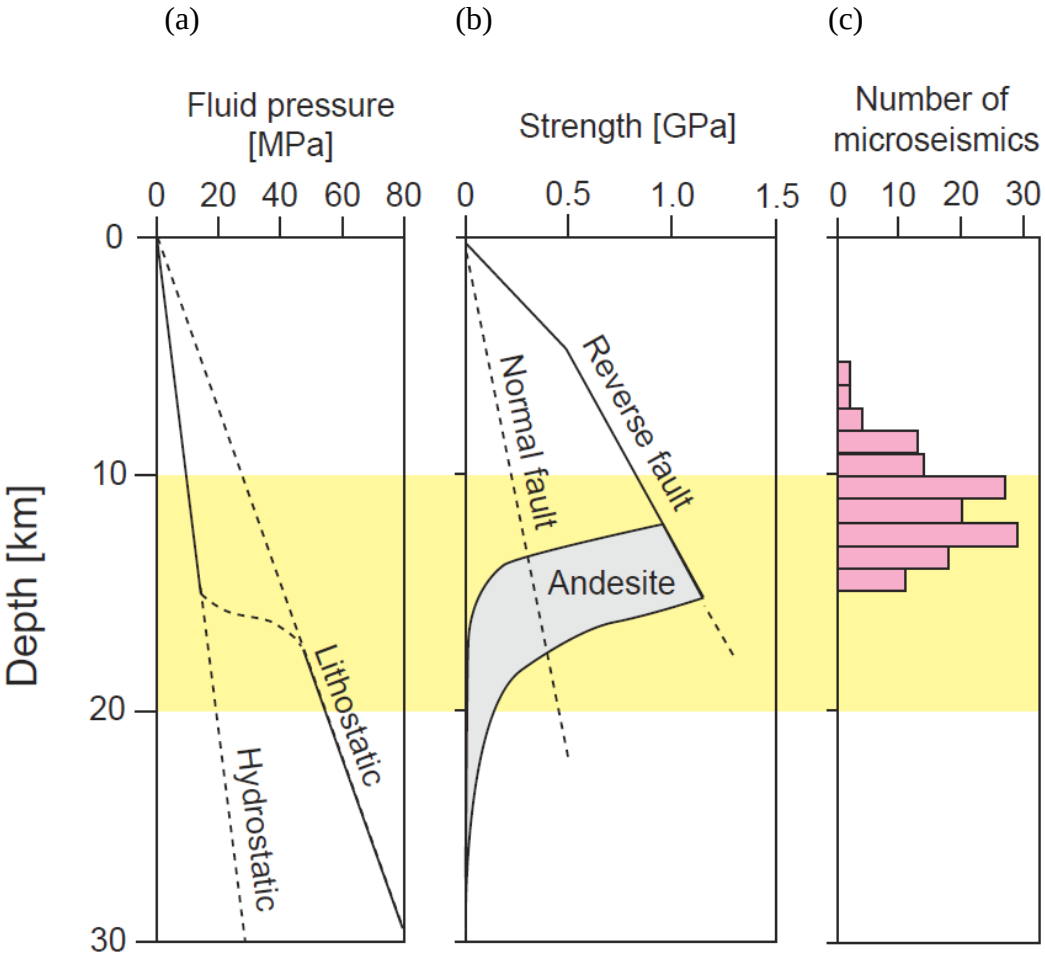

Figure 1-4 The characteristics of the Earth's crust. (a) Fluid pressure calculated by using the density of 1.0 g/cm^3 for hydrostatic and 2.7 g/cm^3 for lithostatic. (b) Rock strength at NE Japan (modified after Shimamoto, 1994). (c) Number of microseismics at NE Japan (modified after Shimamoto, 1994). The yellow zone shows the brittle-plastic transition (BPT) at 10–20 km depth.

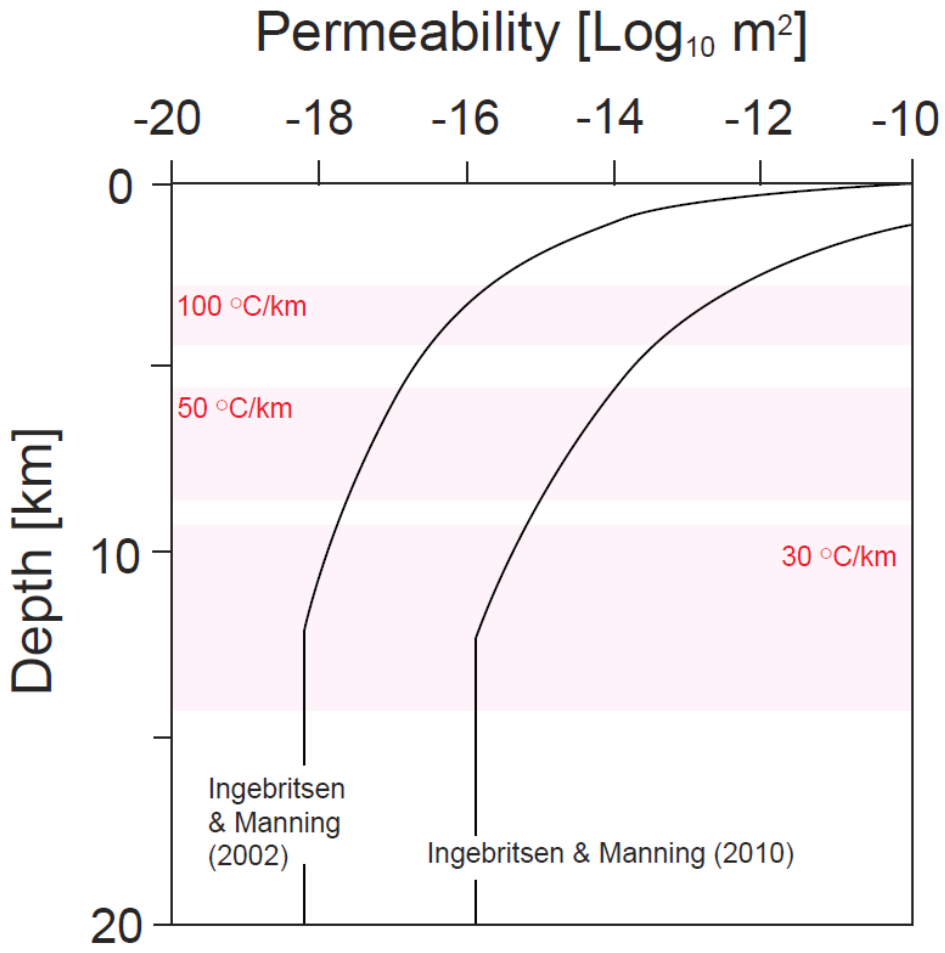

Figure 1-5 Permeability fitted with a constant value (modified after Ingebritsen and Manning, 2002; Ingebritsen and Manning, 2010) and the depth of the brittle-plastic transition (BPT) at 300–450 °C of 30, 50, and 100 °C/km geothermal gradient (red areas).

1.2. Previous works

1.2.1. Observations of silica precipitates

Textures and compositions of silica precipitates have been investigated as one of the important indicators of the hydrological activities within the Earth's crust, which is unraveled in host rock. The shape, orientation and internal structures of veins could reveal deformation kinematics and fluid pressure. Mineralogy and geochemistry of vein-filling minerals and fluid inclusions give information on metamorphic conditions during vein formation, fluid characteristics and origin of fluids.

The types of quartz veins with elongate crystals are divided into fibrous, elongate blocky, and stretched crystal (Oliver and Bons, 2001). All three types have often been loosely termed 'fibrous' in the literature (e.g., Cox, 1987; Nicholson, 1991; Kirschner *et al.*, 1995). Fibrous veins are normally antitaxial, indicating that growth occurred outwards on both surfaces of the vein (Oliver and Bons, 2001). Growth pattern of elongate blocky vein is normally syntaxial, which is on the surfaces of one fracture and inwards from the wallrock (Durney and Ramsay, 1973). The observations of growth competition in elongate blocky veins have been regarded as the result of crystal growth into a fluid-filled crack (Urai *et al.*, 1991; Fisher and Brantley, 1992; Bons, 2000; Okamoto and Sekine, 2011). Stretched-crystal veins have a roughly constant width

across a vein, distinguishing no growth direction (Oliver and Bons, 2001). The presence of cracks during the formation of elongate blocky and stretched-crystal veins permits both closed system diffusional material transport as well as open system material advection through percolating fluids (Oliver and Bons, 2001). Blocky veins, in contrast, can form when nucleation in the primary high supersaturated solution. The formation of blocky veins may be caused by large, near-instantaneous fluid pressure drops upon fracturing result in rapid oversaturation of a particular mineral (Phillips, 1972) or a rapidly fluid ascending, which could realize both the high SiO_2 concentrations required for nucleation and the development of crystal-fluid suspension (Bons, 2001; Okamoto and Tsuchiya, 2009).

Silica sinter are associated with epithermal ore deposits with a wide range of ages (Cunneen and Sillitoe, 1989; White *et al*., 1989; Trewin, 1994; Sherlock *et al*., 1995), and have been used as an indicator of relative age of deposits (Herdianita *et al*., 2000). Amorphous silica scales form as a result of silicic acid, $Si(OH)_4$, polymerization (Ellis and Mahon, 1977). Morphology of silica minerals in silica sinter is controlled mainly by temperature, cyanobacterial growth, and hot spring hydrodynamics (Walter, 1976; Cady and Farmer, 1996).

Diagenesis of silica minerals has been investigated in terms of thermodynamic and/or kinetic considerations. The primary widespread occurrences of metastable silica polymorphs in surficial environments are attributed to the high mineral-solution interfacial tensions of the stable minerals, which is difficult to nucleate directly (Steefel and Van Cappellen, 1990). Mineralogical variations in quartz veins have been considered to result from nucleation of amorphous silica as a metastable precursor, which is converted to the stable phase (quartz) in geologically significant periods of time (Garrels, 1982; Steefel and Van Cappellen, 1990). In contrast to surface silica deposits, however, none of hydrothermal quartz veins contain the relics of other silica polymorphs (e.g., Rusk and Reed, 2002), probably because the primary precipitates as amorphous silica changed to quartz when the quartz vein formed completely. It is still unclear which quartz vein was transformed from amorphous silica or not.

In spite of the huge amounts of observation of silica precipitates, the mechanisms and kinetics of silica precipitation has been unrevealed because observed silica deposits are the fossil after silica precipitation completed, and the on-going process of silica precipitation is not visible and only speculative. Therefore, the experimental evidences are needed to understand how silica precipitation occurs in various conditions.

1.2.2. Equilibrium state of silica minerals

The solubility of silica minerals in aqueous solutions is the fundamental parameter to control the geochemical reactions. The silica concentration of boiling water has been used to estimate the temperature of a geothermal reservoir at depth, based on an assumption that the water was in equilibrium with quartz prior to its ascent and discharge (Fournier and Rowe, 1966). The applicable conditions to estimate the theoretical quartz solubility had been considered experimentally. In the simple system of SiO_2-H_2O, the equilibrium between aqueous SiO_2, $SiO_{2(aq)}$, and quartz, $SiO_{2(quartz)}$, as follows:

$$SiO_{2(quartz)} = SiO_{2(aq)}. \quad (1)$$

The properties of aqueous silica do not depend on the explicit structure of the dissolved silica (Walther and Helgeson, 1977). Because aqueous silica exists as a neutral hydrated monomer species in pure water (Walther and Helgeson, 1977; Walther and Orville, 1983), the activity coefficient of $SiO_{2(aq)}$, γ_{SiO_2}, and molality of $SiO_{2(aq)}$, b_{SiO_2}, are given by

$$\log K = \log \gamma_{SiO_2} = \log b_{SiO_2} \quad (2)$$

where K is the equilibrium constant of $SiO_{2(aq)}$, which is 1 in equilibrium state.

Fournier and Potter (1982) were determined the solubility of quartz in water in the conditions from 1 bar (0.1 MPa) at 25 °C to 10 kb (1 GPa) at 900 °C. They proposed a simple equation expressing solubility in terms of temperature and specific volume of water based on the good correlation between the logarithmic molality of silica concentration, b_{Si} (mol/kg), and the logarithmic values of specific volume of pure water, V_{sp} (cm^3/kg), at each temperature. The quartz solubility is empirically written as follows:

$$\log b_{Si} = \Phi_1 + \Phi_2 \left(\log V_{sp}\right) + \Phi_3 \left(\log V_{sp}\right)^2 \quad (3)$$

$$\Phi_1 = -4.66206 + 0.0034063T + \frac{2179.7}{T} - \frac{1.1292 \times 10^6}{T^2} + \frac{1.3543 \times 10^8}{T^3} \quad (4)$$

$$\Phi_2 = -0.001418T - \frac{806.97}{T} \quad (5)$$

$$\Phi_3 = 3.9465 \times 10^{-4} T \quad (6)$$

where T is temperature in Kelvin.

Manning (1994) also showed the empirical expression of quartz solubility based on the rapid-quench experiments in the expanded conditions from 5 to 20 kb (0.5 to 2 GPa) and 500 to 900 °C as follows:

$$\log K = \Psi_1 + \Psi_2 \cdot \log \rho_{H_2O} \tag{7}$$

$$\Psi_1 = 4.2620 - \frac{5764.2}{T} + \frac{1.7513 \times 10^6}{T^2} \tag{8}$$

$$\Psi_2 = 2.8454 - \frac{1006.9}{T} + \frac{3.5689 \times 10^5}{T^2} \tag{9}$$

where ρ_{H_2O} is the density of water (kg/m^3).

As shown in Eqs. 3–9 (Fournier and Potter, 1982; Manning, 1994), the density (or specific volume) of water is a critical factor to estimate the quartz solubility. The density of pure water up to 1000 °C and 1 GPa is well studied and summarized in ASME international steam tables (Parry, 2000). However, the other components (NaCl, KCl, CO_2, and CH_4) in the crustal fluid affect to the density of water and the quartz solubility

in the crustal conditions. The density of water including components has been studied above 573 K for the systems of NaCl-H_2O system (Anderko and Pitzer, 1993a), KCl-H_2O and NaCl-KCl-H_2O (Anderko and Pitzer, 1993b), NaCl-H_2O-CO_2 (Duan *et al*., 1995), NaCl-H_2O-CH_4 and NaCl-H_2O-CO_2-CH_4 (Duan *et al*., 2003). The program LonerAP was constructed and published by Akinfiev and Diamond (2009) to calculate the quartz solubility by using the equations of Manning (1994) (Eqs. 7, 8, 9) in the system of H_2O-NaCl-CO_2-KCl.

Figure 1-6a shows the solubilities of quartz at 30, 50, 80, and 100 MPa, calculated by using the program LonerAP (Manning, 1994; Akinfiev and Diamond, 2009). When the geothermal gradient is 30 °C/km, quartz solubility increases with increasing of temperature and pressure along the depth (Fig. 1-6a). However, the solubility of quartz with in pure water has the local maximum and minimum values due to a change of the specific volume of water at each pressure of <100 MPa (Tsuchiya and Hirano, 2007; Fig. 1-6a).

Rimstidt and Barnes (1980) suggested the temperature functions of equilibrium constants for silica-water interactions at saturation vapour pressure including quartz, α-cristobalite, β-cristobalite, and amorphous silica as follows:

quartz $\log K = 1.881 - 2.028 \times 10^{-3} T - 1560/T$ (10)

α-cristobalite $\log K = -0.0321 - 988.2/T$ (11)

β-cristobalite $\log K = -0.2560 - 793.6/T$ (12)

amorphous silica $\log K = 0.3380 - 7.889 \times 10^{-4} T - 840.1/T$. (13)

A FORTRAN computer program, SOLVEQ-XPT, which developed for computing multicomponent homogeneous chemical equilibria in aqueous systems, solves a system of mass-balance and mass-action equations by the Newton-Raphson numerical technique (Reed, 1982, 1998; Reed *et al*., 2010). Figure 1-6b shows the solubilities of silica minerals at 30 MPa calculated by using the program SOLVEQ-XPT (Reed *et al*., 2010). The solubilities of cristobalite and amorphous silica are larger than that of quartz.

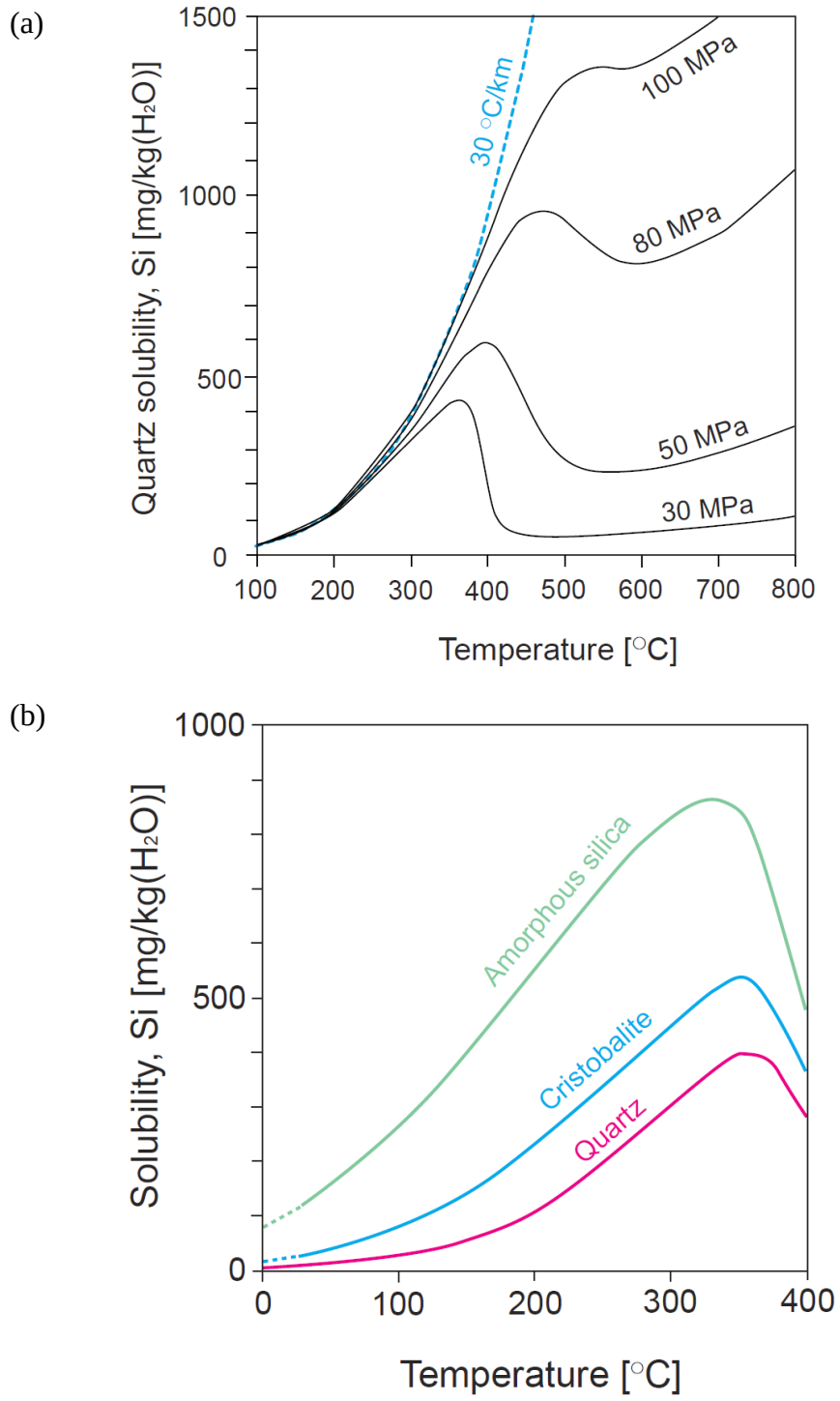

Figure 1-6 (a) Quartz solubilities at 100–800 °C and 30, 50, 80, and 100 MPa, and that in 30 °C/km geothermal gradient and hydrostatic pressure calculated by using the program LonerAP (Manning, 1994; Akinfiev and Diamond, 2009). (b) Solubilities of amorphous silica (green), cristobalite (blue) and quartz (red) at 0–400 °C and 30 MPa calculated by using the program SOLVEQ-XPT (Reed *et al*., 2010).

1.2.3. Kinetics of dissolution and precipitation of silica minerals

Understanding of the reaction kinetics of silica minerals is required to consider the geochemical evolution of the Earth's crust because dissolution and precipitation of silica is possible to greatly affect porosity and permeability in a wide range of crustal rocks and compositions of crustal fluid. Predicting of kinetics of silica precipitation is also necessary to estimate amounts of surficial silica deposits and to maintenance the facilities in geothermal plants.

The reaction of dissolution of silica is given by

$$SiO_2 + 2H_2O \rightarrow H_4SiO_4 \quad (14)$$

and that of precipitation as opposite reaction is

$$H_4SiO_4 \rightarrow SiO_2 + 2H_2O. \quad (15)$$

Silica-water interaction is related to the equilibrium constants. A differential rate equation for silica-water reactions from 0 to 300 °C was determined by Rimstidt and Barnes (1980) as follows:

$$\frac{\partial C_{\mathrm{Si}}}{\partial t} = k_{\mathrm{S}} \frac{A_{\mathrm{Qtz}}}{M_{\mathrm{H_2O}}} (C_{\mathrm{Si,Qtz,eq}} - C_{\mathrm{Si}}) \tag{16}$$

where C_{Si} is the concentration of Si (mg/kg(H_2O)), t is time (sec), k_{S} is the reaction rate constant (kg m^{-2} sec^{-1}), A_{Qtz} is the reaction surface area of quartz (m^2), $M_{\mathrm{H_2O}}$ is the mass of water in the system (kg), and $C_{\mathrm{Si,Qtz,eq}}$ is the solubility of quartz, Si (mg/kg(H_2O)). The reaction rate constant was determined by the Arrhenius equation as follows:

$$k_{\mathrm{S}} = B \exp\left(-\frac{E_{\mathrm{act}}}{RT} \right) \tag{17}$$

where B is the frequency factor in the Arrhenius equation, E_{act} is the activation energy (kJ/mol), R is the gas constant (8.318 J mol^{-1} K^{-1}), and T is temperature in Kelvin. Activation energies of quartz, α- and β-cristobalite, and amorphous silica are 67.4–76.6, 68.7, 65.0, and 60.9–64.9 kJ/mol, respectively (Rimstidt and Barnes, 1980). Bird *et al.* (1986) carried out the dissolution and precipitation experiments at 121–255 °C. The activation energy for quartz precipitation was estimated between 51 and 55 kJ/mol, which were equal to that estimated by Rimstidt and Barnes (1980) within experimental

error. These studies covered temperatures that roughly correspond to the depth of the brittle zone, from the ground surface to 10 km depth, at the field of the typical geothermal gradient (30 °C/km). However, they used the solution of near saturation and near neutral pH, which is not covered the range of the crustal fluid.

The saturation of Si in the solution is an important factor to affect the mineralogy of silica precipitation. In this study, the saturation ratio with respect to quartz, Ω_{Qtz}, is determined as the ratio of Si concentration in the solution, C_{Si}, versus quartz solubility, $C_{Si,Qtz,eq}$ (i.e., $\Omega_{Qtz} = C_{Si}/C_{Si,Qtz,eq}$). Some experiments revealed silica precipitation in the higher Si saturated solution. Rothbaum and Rohde (1979) carried out the precipitation experiments at 5–180 °C in neutral and monomeric silica solutions. The rate of silica polymerization was little dependent on temperature but highly dependent on the saturation ratio with respect to amorphous silica. Especially at 180 °C and in iron pipes, they suggested that geothermal waters could deposit silica scales, even though the silica concentration of the water is lower than the amorphous silica solubility due to formation of iron or nickel silicates. Renders *et al*. (1995) carried out the experiments to measure the rates of dissolution and precipitation for cristobalite at 150–300 °C. The activation energy of dissolution and precipitation was 68.9 and 52.9 kJ/mol, respectively. They suggested that cristobalite may precipitate from hydrothermal solutions of Si

concentration higher than the cristobalite saturation and less than amorphous silica saturation if there are cristobalite nuclei present.

Aqueous silica polymerization occurs within a few hours at acid pH and within a few of minutes at pH >7 (Iler, 1973). Carroll *et al*. (1998) investigated the behaviour of amorphous silica precipitation by comparing the laboratory experiment of pH ranging from 3 to 9 at 100–150 °C and the complex field experiments with geothermal water in the Wairakei, New Zealand, at 58–117 °C. In their experiments, the reaction rate increased with increasing of pH. The reaction order was investigated to be different between the elementary reaction control in the simple laboratory experiments and the surface defect/surface nucleation control in the complex field experiments. Conrad *et al*. (2007) investigated the kinetics of the formation and precipitation of nanocolloidal silica. They suggested that nanocolloidal silica is an important species at low pH and neutral pH at low ionic strengths and may play a more important role in geochemical cycles in natural aqueous systems. In the experiments of high Si concentration in the solution, Ω_{Qtz} >2, precipitation of opal-C at 150 °C was observed instead of quartz growth on the pre-existing seed quartz crystals (Alekseyev *et al*., 2010).

Hydrothermal quartz veins and silica deposits contain various trace elements, including Al, Ca, K, Na, Ti, and Li (Monecke *et al.*, 2002; Rusk *et al.*, 2008).

Distributions of trace elements in quartz veins have been observed as zoning by analysis of scanning electron microscope-cathodoluminescence (SEM-CL) (e.g., Rusk and Reed, 2002) to decipher complex histories of vein formation. However, the effect of trace elements on formation of quartz veins is unclear. Especially, aluminium is dominant next to oxygen and silica in the crust, which has been recognized as one of the important components in the fluid affecting to the silica solubility and silica-water interaction (Iler, 1973; Yokoyama *et al*., 1993; Carroll *et al*., 1998; Nishida *et al*., 2009; Miyoshi, 2005; Jourdan *et al*., 2009). Iler (1973) suggested that the adsorption of small amounts of alumina on the surface of amorphous silica reduces the rate of solution as well as the equilibrium solubility of silica in water because negative aluminosilicate ion sites on the surface prevent the approach of hydroxyl ions, which are required to catalyze the dissolution of silica, and that the solubility depends on the proportions of silica and alumina on the surface at equilibrium.

Most of these previous experiments of silica precipitation were carried out at ≤300 °C and in liquid phase of water. However, abundant quartz vein has been also observed at higher temperature than 300 °C (e.g., near the brittle-ductile boundary; Fournier, 1999). In addition, silica precipitation has been treated via growth of quartz growth on existing quartz surfaces or nucleation of amorphous silica and cristobalite,

not mixing of surface reaction and nucleation in the previous studies. However, it is uncertain whether diagenesis of silica minerals can occur following precipitation of amorphous silica without quartz or not.

Okamoto *et al*. (2010) carried the complex precipitation experiments with granite substrates and the solution made by dissolution of granite to simulate the formation of quartz veins in the crustal conditions. Temperature and pressure were 430 °C and 30 MPa in the supercritical conditions of water. Their experiments revealed that nucleation of amorphous silica and cristobalite and that of quartz occurred dominantly in the solution made by dissolution of quartz and granite (Si with trace amounts of Al, K, and Na), respectively. In addition, only quartz growth on quartz surfaces occurred at the parts of low Si supersaturated solution, Ω_{Qtz} <1.2, whereas nucleation could be observed only in the solution of Ω_{Qtz} >1.2, indicating that precipitation via both silica nucleation and quartz growth can occur in the high Si saturated solution. The effects of minor components, Si saturation in the solution, and mineralogy of substrates on mineralogy of silica precipitation were discussed by Okamoto *et al*. (2010). However, the systematic relationship between the minor components in the solution and kinetics of silica precipitation is still uncertain.

1.2.4. The role of fluid on geomechanical properties

The brittle-plastic transition (BPT) is marked by the geomechanical model of friction law and plastic flow law (Fig. 1-4b), which roughly corresponds to the observations of the deformation mechanisms of fault zone rocks and the distribution of earthquake hypocentres (Sibson, 1982; Meissner and Strelau, 1982). However, the BPT occurs not at a point depicted in the simple geomechanical model but at a wide range of pressure and temperature in which semibrittle behavior gradually changes from the fully brittle to fully plastic modes of deformation (Scholz, 2002). The experiments of confining pressures with marble revealed that the yield strength and the strain hardening index increases strongly with pressure up to 300 MPa (Scholz, 1968). The deformation experiments of polycrystalline MgO at a variety of temperatures and at pressure of 0, 200, and 500 MPa, revealed that the deformation is a marked effect of pressure on the yield strength at 300 °C, whereas the yield stress does not show a clear pressure dependence at >300 °C (Paterson and Weaver, 1970).

Fluid also has a significant role on friction, which is a controlling factor of the brittle zone. The purely physical effect of fluid on rock strength is known in the Byerlee's law (Byerlee, 1978), which determines the shear stress, τ, as follows:

$$\tau = 50 + 0.6\sigma_n \quad (18)$$

for the normal stress, σ_n >200 MPa, and

$$\tau = 0.85\sigma_n \quad (19)$$

for lower normal stress. The Byerlee's law is used for most of the physical properties of porous solids to govern the behavior of cracks and the macroscopic strength of rocks (Scholz, 2002). Based on the effective stress law, the local pore pressure is independent of the total stress, whereas the coupling of the pore fluid and total pressures is caused by dilatancy, which increases void space, changes the permeability of the rock, reduces the pore pressure, and causes dilatancy hardening (Frank, 1965). In addition, the presence of water enhances plasticity in silicates (Griggs and Blacic, 1965), which is called hydrolytic weakening (Atkinson, 1984; Dunning *et al*., 1984; Freiman, 1984;Swanson, 1984).

Recently, numerous geophysical observations have revealed that the presence of aqueous fluids in the vicinity of the seismogenic zones. Iwamori (2007) simulated that an aqueous fluid at NE Japan is released from the subducting oceanic crust and

subducted to a depth where serpentine and chlorite in the serpentinite layer break down. The hypocenters at NE Japan (1997–1999) distributed at the subduction zone, which is corresponded to the region of large amounts of the upwelling magma and crustal fluid (Okada *et al*., 2010). The mechanism of the seismic activity is expected that fluids supplied from the lower crustal levels may decrease the effective stress by increasing pore pressure. The highly conductive zone was observed below the focal area of the Northern Miyagi earthquake, which is interpreted that fluids might cause that earthquake (Mitsuhata *et al*., 2001). In the central part of NE Japan, low P-wave velocity (V_P), low S-wave velocity (V_S) and low V_P/ V_S distributed in the upper crust of the volcanic areas where some clustered earthquakes were seen, indicating that earthquakes in such anomalous areas may be triggered by the migration or diffusion of H_2O (rather than melt) (Nakajima *et al*., 2001). Hasegawa *et al*. (2001) indicated that the existence of fluids beneath active faults caused the decrease of shear strength of the fault. The deep low-frequency (DLF) earthquakes observed before the mainshock of western Tottori earthquake 2000 was also thought to have a single-force type source mechanism, which may be attributed to the transport of fluids such as magma or water (Ohmi and Obara, 2002). Although the presence of H_2O near hypocentres is true, the role of fluid on generation of earthquakes is still unclear.

In addition, induced seismicity is known associated with hydrocarbon and geothermal fields. The mechanisms of the induced seismic instabilities at the hydrocarbon fields are thought that (1) fluid injection induces seismic-slip on cracks within the injected reservoir, (2) pure fluid withdrawal causes pore pressure to decrease within the reservoir, and (3) massive hydrocarbon recovery induces crustal readjustments due to the removal of load from the upper crust (Grasso, 1992). Swarms of seismic events were reported to be caused by artificial management of fluids at the geothermal fields of Larderello (Itally; Console and Rossini, 1998) and Coso (California; Scholz, 2002) and during the deep drilling project KTB of NE Bavaria (Germany; Zoback and Harjes, 1997). One of the trigger of seismicity is also thought to be increasing of pore fluid pressure based on the Mohr circle (Scholz, 2002).

The fracture of rocks is the dominant flow path of fluids in the crust. The structure and channel of crustal fractures tend to be changed spatially and temporally by dissolution and precipitation of minerals. Therefore, the knowledge of dissolution and precipitation processes of minerals in fractures is important as the factor of rock permeability and strength. However, there are few studies focusing on the relationship between geochemical reactions in fractures and the hydrological conditions within the Earth’s crust.

1.2.5. The role of silica-water interaction on hydrological properties

Fractures in the crusts are commonly sealed by quartz (e.g., Bons, 2001; Rusk and Reed, 2002; Okamoto *et al*., 2008). The theoretical models have showed that the silica-water interaction could affect the crustal permeability significantly (Connolly, 1997; Lowell *et al*., 1993). Quartz veins, which show variable internal textures (e.g., Bons, 2001; Okamoto *et al*., 2008), are ubiquitous in the crust. Thus, the spatial and temporal variations in permeability within the crust are affected by precipitation of silica minerals from aqueous fluids (Lowell *et al*., 1993; Connolly, 1997; Fournier, 1999; Rusk and Reed, 2002). Fournier (1999) suggested that quartz deposition would be a major factor in the self-sealed zone at the BPT. However, apart from some observations from deep wells in geothermal areas (Fournier, 1991; White and Mrozek, 1998), there is little information on the locations of silica dissolution and precipitation within the Earth's crust.

Moreover, mineral precipitation may cause an increase of the fluid pressure by plugging of the flow path and become the trigger of earthquakes. Fluids in the upper crust could play significant roles such as the trigger of earthquakes and flow dominantly in fractures (faults), which are commonly sealed by minerals. Ubiquitous behaviours of

dissolution and precipitation of silica minerals have a marked effect on the hydrological and mechanical properties, especially porosity and permeability in a wide range of crustal rocks. Hydrothermal self-sealing of transiently permeable fault-fracture systems is widely recognised in active geothermal fields (Grindley and Browne, 1976). Sibson (1990) suggested a mechanism of earthquakes of ‘fault-valve behavior’, which occurs by highly permeable channel ways of faults and causes abrupt fluctuations in fluid pressure linked to the earthquake system. Within faults and fractures, the fluid pressure can fluctuate between lithostatic and hydrostatic in response to the seismic-interseismic cycle (Sibson, 1992), which is one of the possible driving forces of quartz vein formation (Rusk and Reed, 2002). However, the role of dissolution and precipitation of silica minerals on fracture permeability and earthquakes is unclear.

1.3. Objectives

The main aim of this study is to understand the geochemical evolution and its effects on the hydrologic systems within the Earth‘s crust. Especially, precipitation of silica minerals is focused on as a geochemical reaction because silica-water interaction is one of the major geochemical reactions, but mechanism and kinetics of silica

precipitation in the Earth's crust is not clear rather than that of silica dissolution. In addition, the effect of silica precipitation on the permeable-impermeable boundary within the Earth's crust is clarified. The hydrothermal experiments of silica precipitation were conducted in the simulated crustal conditions to understand kinetics of silica precipitation at the permeable-impermeable boundary within the Earth's crust. Based on the derived kinetic equation and solubility of silica minerals, various geochemical and hydrological processes are discussed, including the spatial and temporal change of permeability and fluid distribution, the mechanisms of earthquakes with fluid, and the development and maintenance of the hydrocarbon and the geothermal fields.

1.4. Structure of this thesis

In the chapter 2, two series of hydrothermal flow-through experiments for silica precipitation are conducted by using the Si supersaturated aqueous solution made by dissolution of minerals to simulate the crustal fluid. No rock/mineral substrate is set in the precipitation vessel for dominant occurrence of nucleation of silica minerals. In the first experiments, the strong temperature dependence of silica precipitation is compared with the nucleation rate. In the second experiments, the effect of minor amount of Al

and Na in the solution on the mineralogy of precipitated materials is observed. These experimental results indicate that the structure of hydrothermal quartz vein could be characterized by depth related with temperature and the composition of the crustal fluid.

In the chapter 3, the empirical kinetic equation for precipitation of quartz and other silica minerals is derived. The effect of silica precipitation via silica nucleation is needed to consider the overall rate of silica precipitation as well as crystal growth. The nucleation rate order is derived by the precipitation experiments of flow rate. The nucleation term is introduced into the kinetic equation only under the supercritical conditions of water, based on the experimental results of temperature dependence in the chapter 2. The precipitation rate via nucleation is also derived as a function of minor components in the solution based on the experiments of Al and Na concentrations in the solution in the chapter 2. The experimental results are simulated by using the new kinetic equation of silica precipitation.

The influence of dissolution and precipitation of silica minerals on the hydrological system within the Earth's crust is investigated in the chapter 4. The Kakkonda geothermal field, northeast Japan, is the unique field worldwide with the well that penetrates the boundary between the hydrothermal convection zone and the underlying heat conduction zone (Doi *et al*., 1998), where water is in the supercritical conditions.

Quartz solubility in water calculated along the depth of the well has a local minimum around the bottom of the hydrothermal convection zone. Based on the hydrothermal experiments in the chapter 2, large amount of silica precipitation via quartz nucleation is expected to form the permeable-impermeable boundary of the Kakkonda and other geothermal fields.

In the chapter 5, the evolution of crustal permeability is modelled and simulated via precipitation of silica minerals leading fracture sealing under the condition of the Earth's crust by using the kinetic equation of silica-water reactions derived in the chapter 3 and the quartz solubility calculated in the chapter 4. Based on the numerical simulations, the fastest silica precipitation is found at the permeable-impermeable boundary of the well WD-1a in the Kakkonda geothermal field by the downward-fluid flow. The timescale for fracture sealing at ~2 km depth is ~1 Ma, which correlates with the age of the Kakkonda granite expected in previous studies, whereas that at the permeable-impermeable boundary is ~100 times shorter than that at shallower depth. These results suggest that the boundary between the permeable and the impermeable zones might have formed at the early stage in the evolution of the Kakkonda geothermal field.

2. THE HYDROTHERMAL EXPERIMENTS OF SILICA PRECIPITATION

2.1. Introduction

Various structures of quartz vein are regarded to have information of the crustal conditions when precipitation of silica minerals occurred. A blocky texture in which grains are roughly equidimensional and randomly oriented is considered to be the primary formation due to nucleation of new grains and also to be the secondary formation due to recrystallisation of a primary texture (Bons, 2000). On the other hand, elongate blocky texture is regarded to form when nucleation of new grains does not occur during vein growth, and all growth is by crystallographically continuous overgrowths on existing grains (Bons, 2000). Nucleation rate of amorphous silica is faster than that of quartz because the surface energy of quartz (350 mJ/m^2) is much higher than that of amorphous silica (45 mJ/m^2) at 25 °C (Steefel and Van Capperen, 1990). In the previous experiments of the solution with concentration of Si near the solubility of amorphous silica, silica precipitation did not occur immediately in the form of quartz but metastable silica modification at 200–300 °C (Alekseyev *et al.*, 2010). However, the evidence of nucleation of amorphous silica has not been observed in quartz vein. The conditions to produce various textures of quartz vein are still poorly understood.

One of the important factors of mineralogy of silica precipitation is minor components in the fluid. Hydrothermal quartz veins contain various trace elements (Monecke, *et al.*, 2002; Rusk *et al*., 2008). Especially, Aluminium is recognized as one of the important components in the fluid to affect dissolution and precipitation of silica minerals. The solubility of amorphous silica, which is observed as surficial silica deposits, is decreased by trace amount of aluminium (Iler, 1973). Aluminium has been also known to accelerate the silica deposition (Yokoyama *et al*., 1993; Carroll *et al*., 1998; Nishida *et al*., 2009). The incorporation of Al, H and Li in hydrothermal quartz has been regarded to play important roles to precipitation of silica minerals (Miyoshi *et al*., 2005; Jordan *et al.*, 2009). Okamoto *et al.* (2010) showed that precipitation of quartz dominantly occurred in the solution with minor amount of Al, Na and K, which was made by dissolution of granite, whereas nucleation of amorphous silica occurred dominantly instead of quartz from the solution of high Si concentration without impurity, which was made by dissolution of quartz. Their experiments suggested that the mineralogy and precipitation rate of silica minerals are strongly influenced by the minor components in the solution. Various textures of quartz veins are expected to represent variety of compositions in the crustal fluid controlled by dissolution of host rock.

The temperature dependence and the effect of minor components in the crustal fluid on precipitation of silica minerals are demonstrated in this section. The solution was made by dissolution of quartz, amorphous silica, albite, and granite to simulate the crustal fluid. Concentration of Si in the prepared solution was much higher than that of quartz. Precipitation of silica minerals via nucleation occurred dominantly because no rock/mineral substrate was set in the precipitation tube.

2.2. Fundamental methods of the hydrothermal flow-through experiment

2.2.1. Apparatus

The hydrothermal flow-through experiments were conducted to reveal the effects of temperature and minor components in the solution on silica precipitation. The cylindrical stainless steel tube (SUS316) was used as the reaction vessel. Diameter of the SUS tube was 10 mm. Distilled water was pumped by the solution supplying pump for high performance liquid chromatography (HPLC) (JASCO, Japan). The flow rate was kept constant during individual runs. The apparatus was composed of the dissolution and precipitation parts of horizontal flow path. In the dissolution part, Si supersaturated solution was prepared by dissolution of minerals (quartz, amorphous

silica, granite, or albite) to simulate the crustal fluid. The grain size of dissolved minerals was 1–2 mm. The difference of temperature between the dissolution and precipitation parts causes the Si supersaturated solution in the precipitation part. No rock/mineral substrate was placed in the precipitation vessel because the previous experiments using granite substrates (Okamoto *et al*., 2010) suggested that overgrowth on pre-existing quartz is minor compared with the nucleation and growth of quartz in the fluids.

2.2.2. Analytical methods

During individual runs, the input and output solutions (i.e., before and after passing through the precipitation vessel, respectively) were periodically sampled after quenching. The concentrations of Si and minor components (Al, Na, and K) in the solutions were measured using an inductively coupled plasma–atomic emission spectrometer (ICP–AES; Thermo Scientific iCAP 6300 Duo View, Tohoku University, Japan) and atomic absorption spectrometry (AAS; VARIAN AA240FS, Tohoku University, Japan). Si concentration was derived by using the results of the ten times diluted samples due to the detection upper limit of ICP-AES. The pH of the solutions was measured at room temperature (23 °C).

After each run, the synthesized products were collected from the precipitation vessel, dried at 90 °C for over 24 hours, weighed, and identified using an X-ray diffractometer (XRD; Rigaku MiniFlex II, Tohoku University, Japan). The analytical range was 2θ = 20–30°. Fixed time method was used with scan step 0.02°. The source of X-ray was Cu-Kα. To measure the relative peak intensities and the relative integrated intensities, calcite was added to precipitates as the standard material. The first peak of calcite is at 2θ = 29.4°. The product at one segment in each experiment was picked up 10 ± 0.5 mg and grinded in a mortar for 2 minutes. Calcite powder 10 ± 0.5 mg was mixed with the products for 5 minutes. The intensity and integrated intensity were calculated after processes of smoothing and removing the effect of background and Kα-ray by using the analytical software of XRD data (Rigaku PDXL, Rigaku, Tohoku University, Japan).

The chemical compositions of the products were measured using an electron probe microanalyzer (EPMA; JEOL 8200, The University of Tokyo, Japan; University of Oregon, U.S.A.) and a scanning electron microscope (SEM; University of Oregon, U.S.A.).

2.3. Temperature dependence of silica precipitation

2.3.1. Experimental conditions

To confirm temperature dependence on silica precipitation, the hydrothermal flow-through experiments were conducted at temperature ranging from 200 to 430 °C at 24 MPa (P24-Gr; Table 2-1) and that from 170 to 430 °C at 31 MPa (P31-GA; Table 2-2). The experimental apparatus was consisted with the two stainless steel tubes (Fig. 2-1). In the first vessel for preparation of the Si supersaturated solution, two types of the input solutions were made at 350–360 °C. Si concentration in the input solution, $C_{Si,in}$, was 332–348 mg/kg(H_2O) made by dissolution of granite in the experiment of 24 MPa (Table 2-1). An extremely high-Si input solution was prepared by dissolution of granite mixed with amorphous silica: Si concentration in the input solution was 636–705 mg/kg(H_2O) in the experiment of 31 MPa (Table 2-2). The Si concentration in the input solution corresponded to the saturation ratios with respect to quartz, $\Omega_{Qtz} = C_{Si,in}/C_{Si,Qtz,eq}$, of 1.1–13.1 and 1.5–8.7 in the experiments at 24 and 31 MPa, respectively (Table 2-1, 2-2). The input solutions contained minor amounts of Al (2.0–3.7 mg/kg(H_2O)), Na (1.7–3.7 mg/kg(H_2O)), and K (1.0–1.8 mg/kg(H_2O)) derived from granite (Table 2-1, 2-2).

The length of precipitation vessel was 14 cm. The flow rate was kept constant at 0.4–0.5 g/min. The residence time of fluid in the precipitation vessel decreased with increasing temperature: from 25.2 minutes at 200 °C to 4.2 minutes at 430 °C in the experiment of 24 MPa (Table 2-1), and from 32.2 minutes at 170 °C to 6.9 minutes at 430 °C in the experiment of 31 MPa (Table 2-2). The precipitation rate of silica minerals at each temperature was evaluated from the decrease in Si concentration in solution when flowing through the precipitation vessel (i.e., $dC_{Si} = C_{Si,in} - C_{Si,out}$).

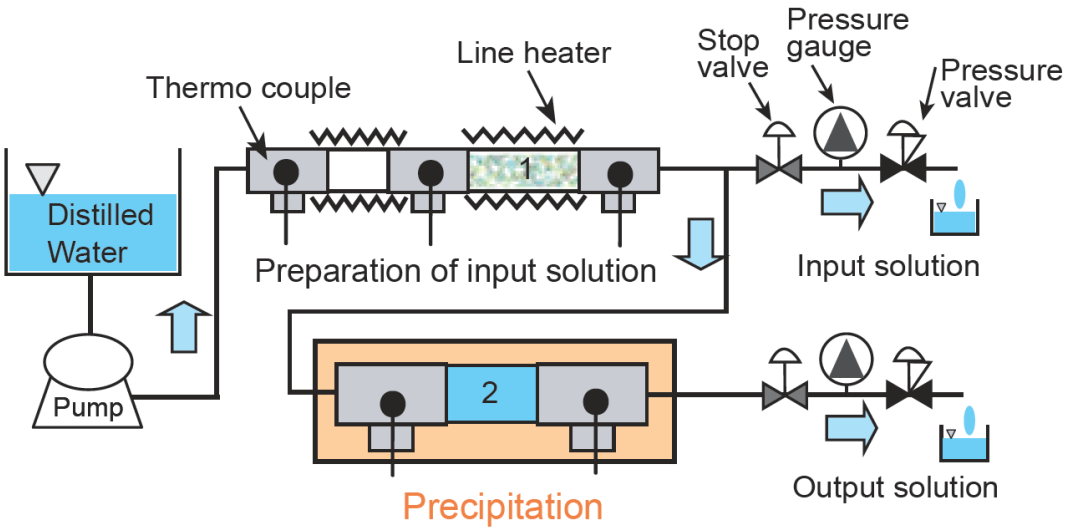

Figure 2-1 Schematic illustration of the apparatus for the experiments of temperature dependence of silica precipitation. Granite or granite mixed with amorphous silica was dissolved in the first vessel to prepare the Si supersaturated solution. The second vessel was for precipitation without rock/mineral substrates. Vessels were consisted of SUS tubes and the T-shaped connections. See text for details.

2.3.2. Results

In the experiment of 31 MPa (P31-GA), the absolute dC_{Si} values were less than the standard deviation, 1σ, of the solution analyses (~5 mg/kg(H_2O) for most samples at <400 °C (Table 2-2). No silica precipitation occurred at lower temperatures even in the extremely high-Si supersaturated solutions (e.g., Ω_{Qtz} = 8.7 at 170 °C; Table 2-2). At 430 °C, however, the Si concentration decreased from 655 mg/kg(H_2O) (Ω_{Qtz} = 8.6) to 148 mg/kg(H_2O) (Ω_{Qtz} = 2.0) (Fig. 2-2; Table 2-2), which was lower than the solubility of amorphous silica (~180 mg/kg(H_2O); Okamoto *et al*., 2010), indicating that nucleation of quartz occurred dominantly in the solution made by dissolution of granite at temperature of >400 °C as found in the previous study (Okamoto *et al*., 2010). The concentrations of minor elements in the solution, Al, Na, and K, decreased during the occurrence of silica precipitation at >400 °C (Table 2-2), indicating the incorporation of these elements into the quartz lattice, which was revealed in the next section (2.4). The pH values were similar between the input and output solutions, pH = 5.3–5.9 and 6.1–6.3, respectively (Table 2-2). The results of the experiment at 24 MPa (P24-Gr) were similar to those of the experiment at 31 MPa: significant precipitation of silica minerals occurred only at higher temperatures of >390 °C, yielding the hockey-stick trend observed in the plot of dC_{Si} versus temperature (Table 2-1; Fig. 2-2).

Table 2-1 Conditions of the experiments of temperature dependence at 24 MPa.

Experiment		**P24-Gr**[1]											
No.		1		2		3		4		5		6		7	
Temperature [°C][2]		200		250		300		380		390		400		430	
Pressure [MPa]		24.4		24.3		24.6		24.7		24.7		24.5		24.5	
Duration time [min]		501		395		495		523		523		556		544	
Residence time [min]		25.2	(0)	23.7	(0)	21.4	(0)	12.4	(0)	8.4	(0)	4.7	(0)	4.2	(0)
Solution[3]															
Number of sample	in[4]	2		2		2		2		2		2		2	
	out[4]	3		3		3		3		3		3		3	
pH[5]	in	7.1	(0.1)	7.0	(0)	6.9	(0.1)	6.9	(0.1)	6.9	(0.1)	7.0	(0.2)	6.9	(0.1)
	out	7.4	(0)	7.2	(0)	7.0	(0)	7.0	(0)	7.0	(0.1)	6.9	(0.1)	6.9	(0.1)
Concentrations [mg/kg(H_2O)][2]															
Si	in	344	(3)	342	(5)	348	(0)	332	(11)	338	(1)	334	(10)	340	(3)
	out	337	(3)	344	(2)	342	(2)	334	(0)	345	(30)	77	(1)	73	(0)
Quartz solubility, Si		117		203		313		243		58		38		28	
Ω_{Qtz}[6]	in	2.9		1.7		1.1		1.4		5.8		8.8		12.1	
	out	2.9		1.7		1.1		1.4		5.9		2.0		2.6	
Al	in	2.1	(0.1)	2.0	(0.1)	2.3	(0)	2.3	(0.1)	2.5	(0.1)	2.3	(0.1)	2.0	(0)
	out	1.5	(0)	1.9	(0)	2.2	(0)	1.8	(0)	1.4	(0.6)	0.0	(0)	0.0	(0)
Na	in	3.7	(0.2)	3.1	(0.1)	3.7	(0.3)	3.3	(0.6)	3.0	(0.3)	3.4	(0.6)	2.6	(0.5)
	out	3.8	(0.1)	3.3	(0)	3.8	(0.1)	3.5	(0)	3.1	(0.6)	1.2	(0.1)	0.6	(0)
K	in	1.4	(0.1)	1.3	(0.1)	1.3	(0.1)	1.8	(0.5)	1.6	(0.3)	1.6	(0.4)	1.3	(0.3)
	out	1.4	(0)	1.3	(0)	1.3	(0)	1.1	(0)	0.6	(0.2)	0.1	(0)	0.1	(0)

[1] P24 = Pressure at 24 MPa, Gr = Dissolution of granite in H_2O at 350 °C.

[2] Temperature for precipitation.

[3] Average value (standard deviation, 1σ).

[4] in = input solution, out = output solution (solution before and after passing through the precipitation vessel, respectively).

[5] At room temperature.

[6] Si saturation ratio with respect to quartz.

Table 2-2 Conditions of the experiments of temperature dependence at 31 MPa.

Experiment		**P31-GA**[1]											
No.		1		2		3		4		5		6		7	
Temperature [°C][2]		170		200		250		300		350		400		430	
Pressure [MPa]		31.4		31.4		32.0		31.5		31.0		31.0		31.0	
Duration time [min]		388		316		305		308		323		296		332	
Residence time [min]		32.2	(0)	31.1	(0.1)	29.0	(0.1)	26.6	(0)	22.9	(0)	13.2	(0)	6.9	(0)
Solution[3]															
Number of sample	in[4]	2		2		2		2		2		2		2	
	out[4]	3		2		3		2		3		2		2	
pH[5]	in	5.5	(0.1)	5.3	(0)	5.7	(0.2)	5.7	(0)	5.7	(0)	5.7	(0)	5.9	(0)
	out	6.2	(0.1)	6.1	(0)	6.3	(0)	6.3	(0)	6.2	(0.1)	6.3	(0)	6.2	(0.1)
Concentrations [mg/kg(H_2O)][2]															
Si	in	700	(1)	705	(5)	705	(5)	692	(3)	662	(6)	636	(5)	655	(28)
	out	696	(7)	688	(5)	705	(4)	699	(1)	651	(2)	609	(13)	148	(5)
Quartz solubility, Si		81		119		207		324		429		229		77	
Ω_{Qtz}[6]	in	8.7		5.9		3.4		2.1		1.5		2.8		8.5	
	out	8.6		5.8		3.4		2.2		1.5		2.7		1.9	
Al	in	3.0	(0)	3.7	(0.1)	2.8	(0.1)	2.6	(0)	2.5	(0)	2.7	(0)	2.6	(0.2)
	out	2.6	(0)	3.2	(0)	2.2	(0.1)	1.9	(0)	1.8	(0)	0.4	(0)	0.3	(0)
Na	in	2.0	(0.1)	2.8	(0)	1.8	(0.1)	1.7	(0.1)	1.8	(0)	1.9	(0.1)	1.8	(0.2)
	out	2.0	(0)	2.9	(0)	1.8	(0.1)	1.7	(0)	1.8	(0)	0.9	(0)	0.4	(0)
K	in	1.2	(0)	1.0	(0.1)	1.3	(0.2)	1.4	(0.2)	1.5	(0.1)	1.7	(0.2)	1.3	(0)
	out	1.2	(0)	1.1	(0)	1.3	(0.1)	1.3	(0)	1.4	(0)	0.3	(0)	0.2	(0)

[1] P31 = Pressure at 31 MPa, GA = Dissolution of granite + amorphous silica at 360 °C.

[2] Temperature for precipitation.

[3] Average value (standard deviation, 1σ).

[4] in = input solution, out = output solution (solution before and after passing through the precipitation vessel, respectively).

[5] At room temperature.

[6] Si saturation ratio with respect to quartz.

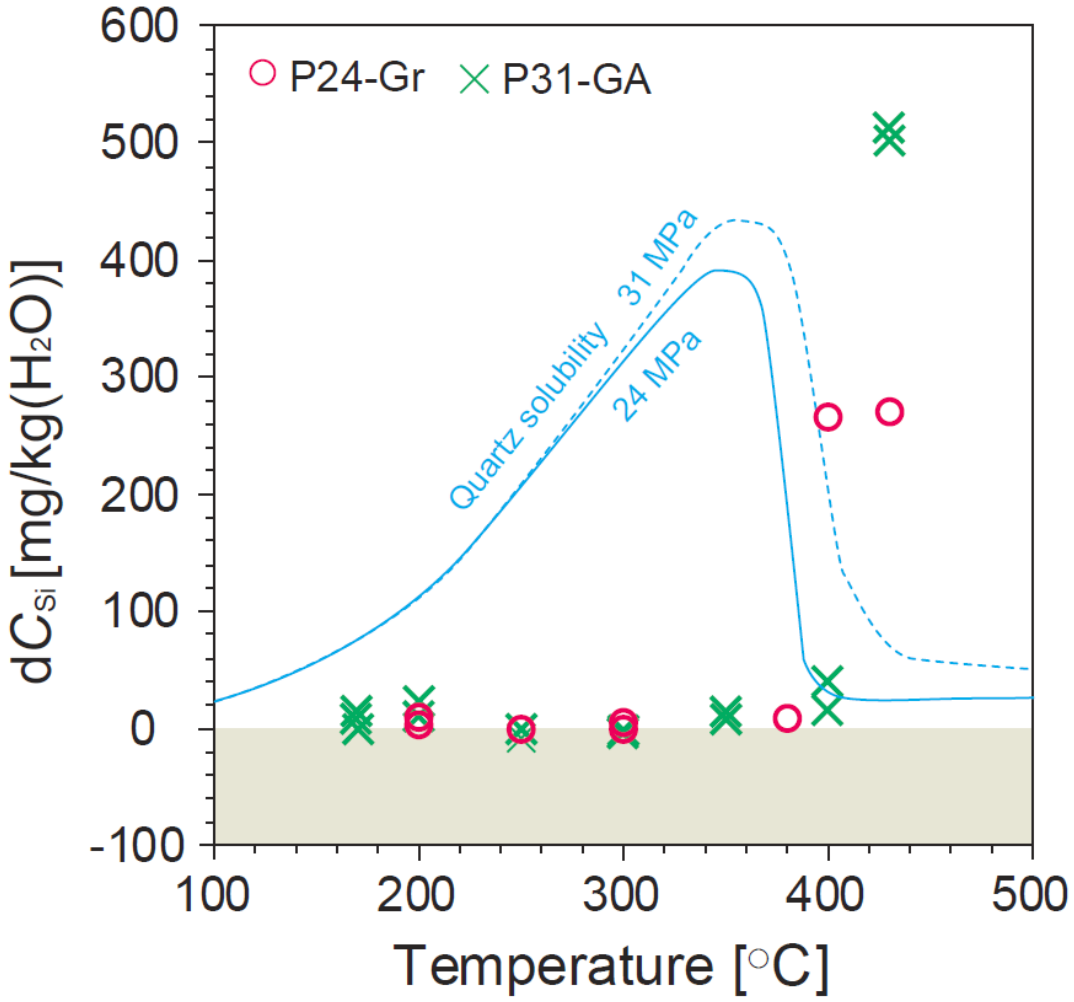

Figure 2-2 Temperature of precipitation and difference of Si concentrations between the input and output solutions. The red circles and the green crosses show the difference of Si concentrations between the input and output solutions, dC_{Si}, in the experiment of 24 MPa and 31 MPa, respectively. The blue solid and broken lines show the solubility of quartz at 24 and at 31 MPa, respectively.

2.3.3. Discussion

The experiments of temperature dependence revealed that large amount of silica precipitation occurs without a quartz substrate at high temperature, >390 °C. The strong temperature dependence of the silica precipitation showed a hockey-stick-like shape (Fig. 2-2), which cannot be explained by the rate equation for surface overgrowth investigated in the previous study (Rimstidt and Barnes, 1980).

On the other hand of surface reaction, the conventional nucleation theory (Steefel and Van Cappellen, 1990) shows the equation of nucleation rate, *I*, as follows:

$$I = \frac{2D}{d^5} \exp\left(\frac{-16\pi\upsilon \cdot {E_{\mathrm{surf}}}^3}{R^3 T^3 \ln \Omega_{\mathrm{Qtz}}} \right) \tag{20}$$

where D is the aqueous diffusion coefficient (10^{-5} cm^2/s), d is the molecular diameter of quartz (5 Å; Lasaga, 1998), R is the gas constant (8.31 J $K^{-1}mol^{-1}$), T is temperature in Kelvin, Ω_{Qtz} is the Si saturation ratio with respect to quartz, υ is the molar volume of quartz (22.688 cm^3/mol; Lasaga, 1998), and E_{surf} is the surface energy ($ergs/cm^2$). The onset of quartz nucleation at 390 °C can be reproduced (Fig. 2-3) when the quartz–H_2O interfacial energy is 130 mJ/m^2, which is similar to the value estimated from greenschist-facies metapelites (145 mJ/m^2) (Hiraga *et al*., 2002).

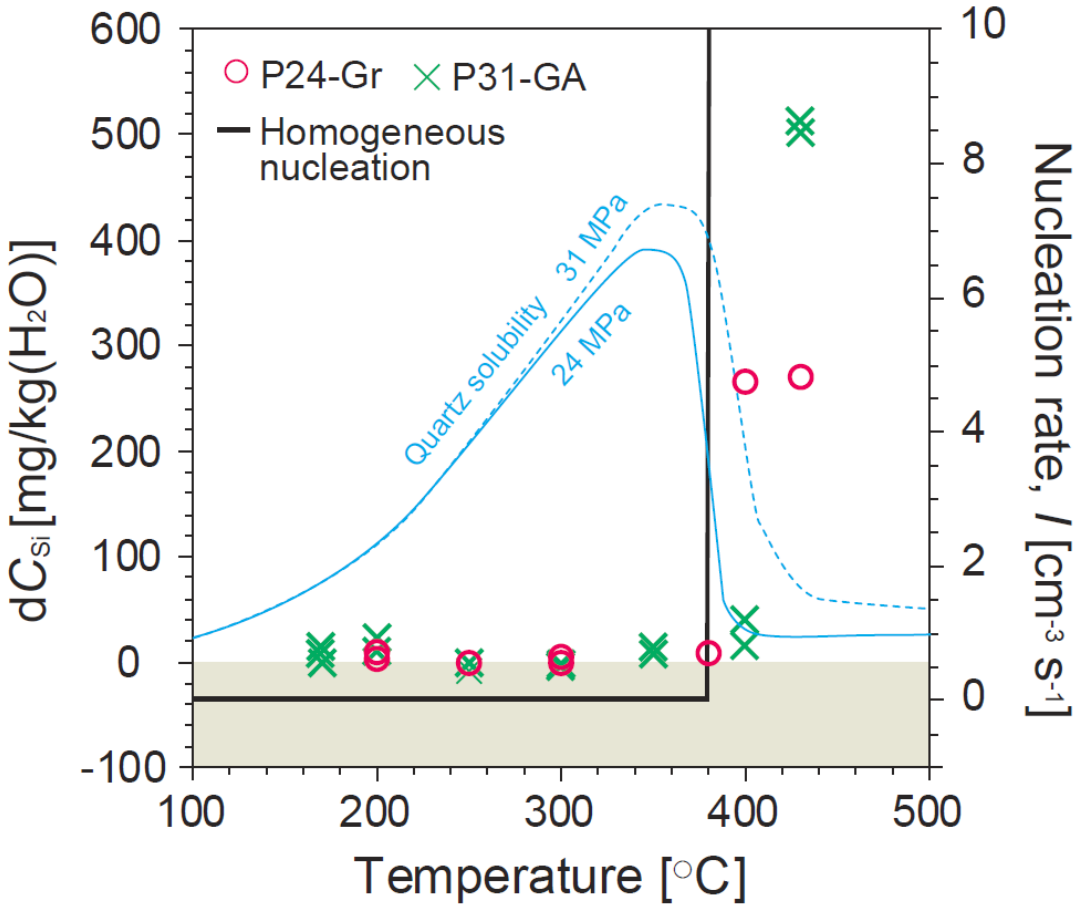

Figure 2-3 Temperature dependence of precipitation and the homogeneous nucleation rate. The red circles and the green crosses show the difference of Si concentrations between the input and output solutions, dC_{Si}, in the experiment of 24 MPa and 31 MPa, respectively. The blue solid and broken lines show the solubility of quartz at 24 and at 31 MPa, respectively. The black line shows the homogenous nucleation rate in the interfacial energy of quartz, σ = 130 mJ/m^2.

2.4. Effects of minor components in the solution on silica precipitation

2.4.1. Experimental conditions

First, dissolution experiments were carried out to find the appropriate condition to produce Si saturated solution with various concentrations of Al and Na. Second, precipitation experiments were conducted to reveal the systematic change of silica precipitation related with minor components, Al and Na, in the solution.

The experimental apparatus consisted of three cylindrical stainless steel reaction vessels of various lengths (diameter, 10.1 mm) connected in series to create a horizontal flow path (Fig. 2-4). Albite sand (Na/(Na+Ca+K) = 0.99) was put in the first vessel (19 cm length), which was connected with the pre-heating vessel (10 cm length). Al and Na concentrations were controlled by temperature of the first vessel. Quartz or amorphous silica sand was in the second vessel for preparation of Si supersaturated solution. The lengths of the second tubes were 25 and 19 cm for dissolution of quartz and amorphous silica, respectively. The third vessel was for precipitation. Fluid pressure was maintained at around 30 MPa in all experiments.

The first experiment of dissolution was conducted only with the first vessel of albite sand to observe how much Al and Na dissolved from the albite in this system. Temperature was set from 150 to 410 °C (Table 2-3). The flow rate was 1.0–2.0 g/min

(Table 2-3). The second experiment of dissolution was conducted to determine the combination of temperatures for dissolution of albite in the first vessel and amorphous silica in the second vessel. The solution made by dissolution of albite in the first vessel flowed into the second vessel to dissolve amorphous silica. The flow rate was 1.0 g/min in the second experiments (Table 2-4).

The conditions of the precipitation experiments are summarized in Table 2-5. The experiments of low Al concentration in the input solution, $C_{Al,in}$ <10 mg/kg(H_2O) and high Al concentration, $C_{Al,in}$ >10 mg/kg(H_2O) were conducted (Table 2-5). The flow rates were 1.6–2.1 ± 0.3 g/min in the experiments of $C_{Al,in}$ <10 mg/kg(H_2O) and 0.4–0.5 g/min in the experiments of $C_{Al,in}$ >10 mg/kg(H_2O), respectively (Table 2-5). Temperature of the second vessel was 360 ± 1 °C to dissolve quartz in the experiments of $C_{Al,in}$ <10 mg/kg(H_2O), 257 ± 4 and 254 ± 6 °C to dissolve amorphous silica in the experiments of $C_{Al,in}$ = 12–17 mg/kg(H_2O), and 280 ± 10 °C to dissolve quartz in the experiment of $C_{Al,in}$ = 29 mg/kg(H_2O), respectively (Table 2-5). In this study, the temperature measurements were accurate to approximately 1 °C for preparation of the solution. Because the solubility of quartz has local maximum value at 360 °C and local minimum value at 430 °C at 30 MPa (Manning, 1994; Akinfiev and Diamond, 2009; Fig 1-6a), precipitation occurred in the third vessel at higher temperature than that of

preparation of the solution. Temperatures of the third vessel were 430 ± 1 °C in the experiments of $C_{Al,in}$ <10 mg/kg(H_2O) and 430-450 °C in the experiments of $C_{Al,in}$ >10 mg/kg(H_2O) (Table 2-5). The lengths of third vessels were 51 cm for the experiments of $C_{Al,in}$ <10 mg/kg(H_2O) and 31 cm for the experiments of $C_{Al,in}$ >10 mg/kg(H_2O). At 430 °C and 30 MPa, the solubility of amorphous silica and cristobalite is 220 and 176 mg/kg(H_2O), respectively (Okamoto *et al.*, 2010), and that of and quartz is 77 mg/kg(H_2O) (Akinfiev and Diamond, 2009).

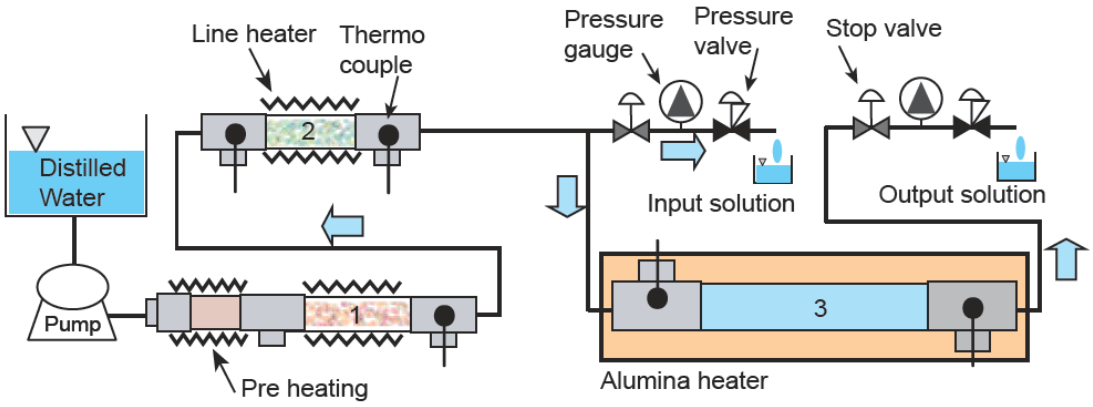

Figure 2-4 Schematic illustration of the apparatus in the hydrothermal flow-through experiments of the minor components, Al and Na, in the solution. The first and second vessels were for preparation of Si supersaturated solution with variable Al and Na. Albite sand was dissolved in the first vessel. Quartz or amorphous silica sand was in the second vessel in the experiments of low and high Al concentration in the solution, $C_{Al,in}$ <10 and >10 mg/kg(H_2O), respectively (see Table 2-5). The third vessel was for precipitation. Vessels were consisted of SUS316 tubes.

2.4.2. Results

2.4.2.1. Chemistry of the solutions in the dissolution experiments

In the experiment of albite dissolution, concentrations of Si, Al, and Na increased from 17, 2, 5 mg/kg(H_2O) to 81, 23, and 28 mg/kg(H_2O), respectively, with increasing of temperature up to 340 °C, and slightly decreased about several mg/kg(H_2O) at temperature ~410 °C (Table 2-3; Fig. 2-5). The molar ratio of Na/Al and Al/Si were 1.2–1.6 and 0.26–0.31, respectively, except the experiment of flow rate of 2.0 g/min (Table 2-3).

In the dissolution experiments of albite and amorphous silica, concentrations of Al and Na were 22–25 and 16–22 mg/kg(H_2O), respectively (Table 2-4). Si concentration from 100 to 196 mg/kg(H_2O) (Table 2-4) was lower than the solubility of amorphous silica from 200 to 713 mg/kg(H_2O) at 109–250 °C (Fig. 1-6b). The molar ratio of Na/Al and Al/Si were 0.83–1.0 and 0.12–0.26, respectively (Table 2-4).

Table 2-3 Conditions and results of the experiment of albite dissolution.

Temperature [°C]	Flow rate [g/min]	Concentrations [mg/kg(H_2O)]			Na/Al [mol/mol]	Al/Si [mol/mol]
		Al	Na	Si		
150	2.0	2	5	19	2.8	0.11
200	2.0	4	6	17	1.7	0.24
250	1.0	12	14	43	1.4	0.29
280	1.0	15	19	57	1.6	0.26
300	1.0	21	22	72	1.2	0.31
310	1.0	19	25	71	1.6	0.28
340	1.0	23	28	81	1.4	0.29
360	1.0	23	27	80	1.4	0.30
410	1.0	21	24	73	1.4	0.30

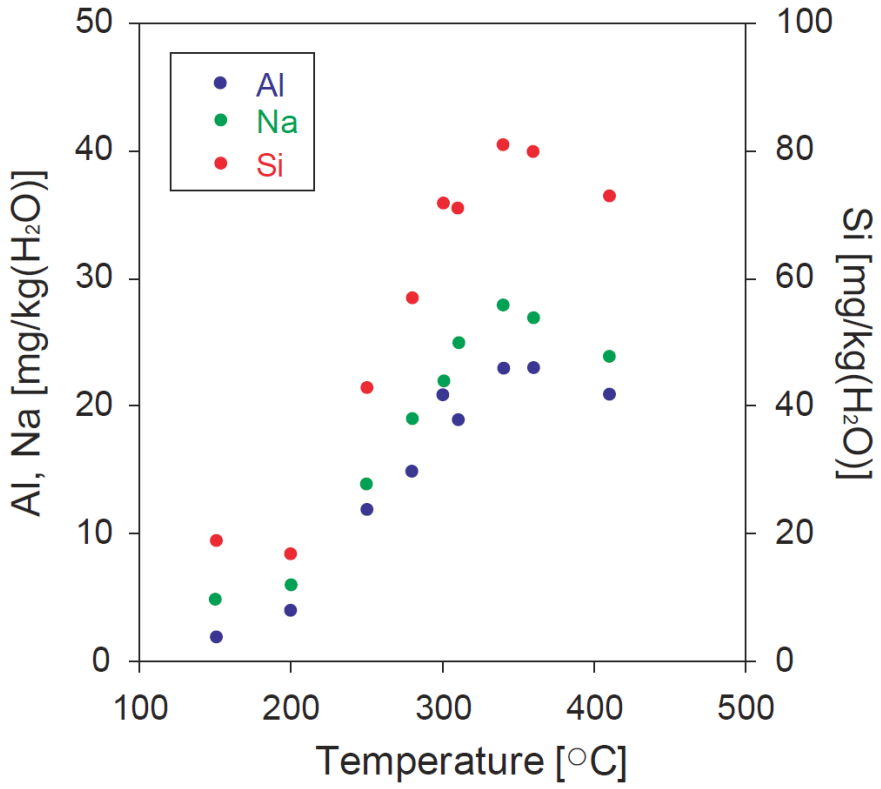

Figure 2-5 Temperature dependence of concentrations of Al (blue), Na (green), and Si (red) in the pre-experiments of albite dissolution.

Table 2-4 Conditions and results of dissolution experiments of albite and amorphous silica.

T (Ab)[1] [°C]	σ (Ab)[2]	T (AS)[3] [°C]	σ (AS)[4]	Flow rate [g/min]	Concentrations [mg/kg(H_2O)]			Na/Al [mol/mol]	Al/Si [mol/mol]
					Al	Na	Si		
301	0.7	109	33	1.0	25	21	100	1.0	0.26
301	0.7	109	33	1.0	25	22	102	1.0	0.26
301	0.7	109	33	1.0	25	21	101	1.0	0.26
351	1.4	141	49	1.0	24	20	102	0.96	0.24
351	1.4	144	47	1.0	24	20	103	0.95	0.25
351	1.4	146	47	1.0	24	20	102	0.97	0.25
350	0.7	205	18	1.0	22	16	116	0.83	0.20
350	0.7	205	18	1.0	22	16	115	0.86	0.20
350	0.7	205	18	1.0	22	17	114	0.87	0.20
350	0.0	250	2.8	1.0	23	19	196	0.94	0.12
350	0.0	250	2.8	1.0	23	19	194	0.95	0.12
350	0.0	250	2.8	1.0	23	19	194	0.96	0.12

[1] Temperature for dissolution of albite.

[2] Standard deviation of temperature for dissolution of albite.

[3] Temperature for dissolution of amorphous silica.

[4] Standard deviation of temperature for dissolution of amorphous silica.

2.4.2.2. Chemistry of the solutions in the precipitation experiments

Ten experiments of silica precipitation were conducted by using the input solution with varying Al concentration, $C_{Al,in}$ = 0, 0.4, 1, 2, 3, 6, 7, 12, 17, and 29 mg/kg(H_2O). The results of the precipitation experiments are summarized in Table 2-5, and the detailed results of each samples were shown in Tables 2-6, 7, 8, 9, 10, and 11 for the experiments of $C_{Al,in}$ = 0, 0.4–2, 3–7, 12, 17, and 29 mg/kg(H_2O), respectively. Each experiment was named Exp. LAl for $C_{Al,in}$ <10 mg/kg(H_2O) and Exp. HAl for $C_{Al,in}$ >10 mg/kg(H_2O) with Al concentration in the input solution, $C_{Al,in}$ (e.g., the name of the experiment of $C_{Al,in}$ = 0 mg/kg(H_2O) was Exp. LAl-0; Tables 2-5–2-11).

Temperature for dissolution of albite varied from 160–350 °C (Table 2-5) based on the results of the pre-experiments of albite dissolution (Table 2-3; Fig. 2-5) and albite and amorphous silica dissolution (Table 2-4). Temperature in the second vessel was 360 ± 1 °C for dissolution of quartz in the experiments of $C_{Al,in}$ <10 mg/kg(H_2O), 257 ± 4 and 254 ± 6 °C for dissolution of amorphous silica in the experiments of $C_{Al,in}$ = 12 and 17 mg/kg(H_2O), and 280 ± 10 °C for dissolution of quartz in the experiments of $C_{Al,in}$ = 29 mg/kg(H_2O) (Table 2-5). In the input solution, the Na/Al molar ratio ranged 1.3–2.1 (Table 2-5). In the experiments of low Al ($C_{Al,in}$ <10 mg/kg(H_2O)), Si concentration in the input solution, $C_{Si,in}$, ranged from 268 to 375 mg/kg(H_2O), which corresponded to

the saturation ratio with respect to quartz, Ω_{Qtz}, ranging 3.1–5.0 (Table 2-5). At 430 °C and 30 MPa, the solubility of amorphous silica (220 mg/kg(H_2O)) (Okamoto *et al.*, 2010) corresponds with Ω_{Qtz} = 2.9 due to the quartz solubility of 77 mg/kg(H_2O) (Akinfiev and Diamond, 2009; Fig. 2-6). Therefore, the solutions prepared in these experiments were supersaturated with respect not only to quartz but also to amorphous silica. Si concentration in the input solutions of the experiments of $C_{Al,in}$ >10 mg/kg(H_2O) ranged from 186 to 230 mg/kg(H_2O), which was supersaturated with respect to quartz (Table 2-5) and was slightly supersaturated or undersaturated with respect to amorphous silica (Fig. 2-6).

Si concentration in the output solution decreased from 224 to 98 mg/kg(H_2O) with increasing of Al and Na concentrations in the input solutions from 0 to 6.7 and 7.6 mg/kg(H_2O), respectively (Table 2-5). On the other hand, Si concentration in the output solution in the experiments of $C_{Al,in}$ >10 mg/kg(H_2O) ranged from 105 to 128 mg/kg(H_2O), which did not correlate with increasing of Al concentration in the input solution (Table 2-5). Al concentrations in the output solutions were nearly 0 mg/kg(H_2O) regardless of that in the input solutions in all experiments (Table 2-5), indicating that precipitation of whole Al in the input solutions occurred during path-through the precipitation vessel. The Si saturation ratio with respect to quartz in the

output solution ranged from 2.1 to 2.9 in the experiment of $C_{Al,in}$ <3 mg/kg(H_2O) and decreased to 1.4–1.6 at $C_{Al,in}$ ≥3 mg/kg(H_2O) (Table 2-5).

The difference in Si concentration between the input and output solutions, dC_{Si}, increased from 77 to 257 mg/kg(H_2O) with increasing of Al concentrations in the input solutions from 0 to 7 mg/kg(H_2O), then decreased to 78–108 mg/kg(H_2O) in the experiments of $C_{Al,in}$ >10 mg/kg(H_2O) (Fig. 2-7). The difference in Al concentration, dC_{Al}, positively correlated with that in Na concentration, dC_{Na} (dC_{Na}/dC_{Al} = 1.0–1.2) (Fig. 2-8).

The standard deviations of the Al and Na concentrations were almost <1 mg/kg(H_2O), which were nearly constant during the run-time of the experiments (Table 2-5). The standard deviation of the Si concentrations ranged from 2 to 32, which was larger than that of Al and Na (Table 2-5) because of dilution of the solution for the analysis. The Al and Na concentrations in the experiments of $C_{Al,in}$ = 17 and 29 mg/kg(H_2O) relatively varied with the standard deviations ~11 mg/kg(H_2O) also because of measure of the diluted samples (Table 2-5). The ratio of differences of Al and Na concentrations in the input and output solutions in the experiments of $C_{Al,in}$ = 29 mg/kg(H_2O) was 1.6, perhaps because of over-observation of high Na concentration >10 mg/kg(H_2O) in the diluted samples by ICP-AES (Table 2-5).

The pH values of input solutions ranged from 5.5 to 8.2 at room temperature and increased with increasing of Al and Na concentrations in the input solutions (Table 2-5). The difference of pH between input solution and output solution was lower than 0.4 for individual experiments. However pH value might affect to precipitation reaction, it was not critical in these experiments. The pH value in the experiments of $C_{Al,in}$ = 29 mg/kg(H_2O) was not measured.

Table 2-5 Summary of conditions and results of the experiments of minor components in the solution.

Exp. Name		LAl-0		LAl-0.5		LAl-1		LAl-2		LAl-3		LAl-6		LAl-7		HAl-12		HAl-17		HAl-29	
Exp. Number		1		2		3		4		5		6		7		8		9		10	
Pressure [MPa]		30.9	(0.3)	31.8	(0.5)	31.4	(0.5)	31.0	(0.8)	30.9	(1.6)	30.5	(0.5)	30.5	(1.0)	30.6	(0.6)	31.4	(2.1)	31.1	(2.1)
Temperature [°C]		430	(1.0)	430	(1.0)	430	(1.0)	430	(1.0)	430	(1.0)	430	(1.0)	430	(1.0)	434	(3.7)	430	(1.0)	430	(1.0)
Volume of water [cm^3/g]		5.1		4.8		5.0		5.1		5.2		5.3		5.3		5.5		4.9		5.1	
Duration time [hour]		113		76		83		80		91		87		76		366		342		202	
Flow rate [g/min]		1.9	(0.2)	2.1	(0.1)	2.1	(0.1)	2.0	(0.1)	1.8	(0.2)	1.8	(0.1)	1.6	(0.3)	0.5	(0)	0.5	(0)	0.4	(0)
Tube length [cm]		51		51		51		51		51		51		51		32		32		32	
Residence time [min]		4.7	(0.4)	4.3	(0.1)	4	(0.2)	4.1	(0.1)	4.4	(0.4)	4.5	(0.3)	5.1	(0.9)	8.4	(0.1)	9.3	(0.4)	5.1	(0.1)
Weight of precipitation [g]		1.5		1.5		2.7		2.7		4.6		4.6		4.6		1.7		1.9		1.2	
Weight change [mg/h][1]		13		20		33		33		50		53		61		5		6		6	
Preparation of solutions																					
Tube1, temperature [°C][2]		-		160	(1)	182	(1)	210	(1)	200	(1)	330	(1)	240	(1)	219	(1)	247.3	(2)	350	(0)
Tube2, dissolved material[3]		Qtz		Qtz		Qtz		Qtz		Qtz		Qtz		Qtz		AmSil		AmSil		Qtz	
Tube2, temperature [°C][4]		360	(1)	360	(1)	360	(1)	360	(1)	360	(1)	360	(1)	360	(1)	257	(4)	254	(6)	280	(10)
Solution[5]																					
Sampling number		11		3		3		3		3		3		3		9		8		5	
pH[6]	in[7]	5.5	(0.6)	5.9	(0)	6.7	(0.1)	6.6	(0.1)	6.6	(0)	7.9	(0.1)	7.2	(0.3)	8.0	(0.4)	7.6	(0.3)	n.m.	
	out[7]	6	(0.7)	6	(0.1)	6.6	(0.2)	6.5	(0.2)	6.7	(0.3)	8.2	(0.3)	7.1	(0.4)	7.6	(0.5)	7.7	(0.3)	n.m.	
Concentrations [mg/kg(H_2O)]																					
Si	in	301	(29)	268	(15)	375	(7)	331	(10)	316	(32)	318	(23)	355	(18)	187	(11)	230	(16)	186	(2)
	out	224	(32)	181	(6)	209	(18)	162	(19)	118	(17)	104	(4)	98	(9)	109	(17)	128	(17)	105	(5)
Quartz solubility		76		87		82		77		75		71		72		68		82		79	
Ω_{Qtz}[8]	in	4.0		3.1		4.6		4.3		4.2		4.5		5.0		2.8		2.8		2.4	
	out	2.9		2.1		2.6		2.1		1.6		1.5		1.4		1.6		1.5		1.3	
Al	in	0	-	0.4	(0)	1.4	(0.2)	2.3	(0.1)	3.0	(0.1)	5.6	(0.9)	6.7	(0.6)	12	(0.5)	17	(0.8)	29	(4.4)
	out	0	-	0	(0)	0.1	(0)	0.9	(0)	0.1	(0)	0.0	(0)	0.1	(0)	0.2	(0.1)	0.3	(0.2)	0.0	(0)
Na	in	0	-	0.7	(0)	1.5	(0.2)	2.5	(0.2)	3.5	(0.1)	8.2	(1.1)	7.6	(0.7)	14	(0.6)	23	(2.0)	45	(11)
	out	0	-	0.3	(0)	0.3	(0.1)	1.8	(1.2)	1.0	(0.1)	3.4	(0.1)	1.4	(0.4)	2.9	(0.7)	4.8	(0.5)	5.5	(0.9)
$(Na/Al)_{in}$ [mol/mol]	in	-	-	2.1	(0.1)	1.3	(0.2)	1.3	(0)	1.4	(0)	1.7	(0.1)	1.3	(0)	1.3	(0)	1.5	(0)	1.8	(0)
$(Na/Al)_{dif}$ [mol/mol]	in	-	-	1.3	(0.2)	1.0	(0.1)	1.0	(0)	1.0	(0)	1.0	(0.1)	1.1	(0)	1.1	(0.1)	1.2	(0)	1.6	(0)
$(Al/Si)_{in}$ [10^{-2} mol/mol]	in	0		1		4		7		10		18		20		67		77		164	

Table 2-5 continued (footnote).

[1] Total weight of precipitation divided by the duration.

[2] Temperature of the albite dissolution vessel for preparing the input solutions.

[3] Dissolved silica minerals in the second vessel: Qtz = Quartz, AmSil = Amorphus silica.

[4] Temperature of the silica dissolution vessel for preparing the input solutions

[5] Average value (standard deviation, 1σ).

[6] At room temperature.

[7] in = input solution, out = output solution (solution before and after passing through the precipitation vessel, respectively).

[8] Si saturation ratio with respect to quartz.

Table 2-6 Compositions of the solutions in the experiment of $C_{Al,in}$ = 0 mg/kg(H_2O) (Exp. LAl-0).

Experiment		**LAl-0**										
No.[1]		1	2	3	4	5	6	7	8	9	10	11
pH[2]	in	6.8	n.m.	5.7	5.3	4.8	n.m.	5.4	n.m.	5.4	n.m.	5.2
	out	7.4	6.9	5.7	6.0	5.4	n.m.	5.5	n.m.	5.7	n.m.	5.5
Concentrations [mg/kg(H_2O)][3]												
Si	in	246	260	285	310	341	311	284	309	323	321	323
	out	162	203	221	250	197	246	204	248	256	268	214
Ω_{Qtz}[4]	in	3.2	3.4	3.7	4.1	4.5	4.1	3.7	4.1	4.2	4.2	4.2
	out	2.1	2.7	2.9	3.3	2.6	3.2	2.7	3.3	3.4	3.5	2.8

[1] Solution sample number.

[2] At room temperature.

[3] in = input solution, out = output solution (solution before and after passing through the precipitation vessel, respectively).

[4] Si saturation ratio with respect to quartz.

Table 2-7 Compositions of the solutions in the experiments of $C_{Al,in}$ = 0.4–2 mg/kg(H_2O) (Exp. LAl-0.4, 1, 2).

Experiment		**LAl-0.4**		**LAl-1**			**LAl-2**		
No.[1]		1	2	1	2	3	1	2	3
pH[2]	in	5.9	5.9	6.8	6.7	6.6	6.6	6.6	6.8
	out	6.1	6.0	6.3	6.6	6.8	6.2	6.8	6.6
Concentrations [mg/kg(H_2O)][3]									
Si	in	257	278	369	373	382	333	340	319
	out	177	185	223	215	188	181	142	165
Ω_{Qtz}[4]	in	3.0	3.2	4.5	4.6	4.7	4.3	4.4	4.2
	out	2.0	2.1	2.7	2.6	2.3	2.3	1.8	2.1
Al	in	0.4	0.4	1.3	1.3	1.6	2.1	2.4	2.4
	out	0.0	0.0	0.1	0.1	0.0	0.1	0.0	0.0
Na	in	0.7	0.6	1.3	1.7	1.5	2.2	2.6	2.6
	out	0.2	0.3	0.3	0.5	0.2	0.4	0.6	0.6

[1] Solution sample number.

[2] At room temperature.

[3] in = input solution, out = output solution (solution before and after passing through the precipitation vessel, respectively).

[4] Si saturation ratio with respect to quartz.

Table 2-8 Compositions of the solutions in the experiments of $C_{Al,in}$ = 3–7 mg/kg(H_2O) (Exp. LAl-3, 6, 7).

Experiment		**LAl-3**			**LAl-6**			**LAl-7**		
No.[1]		1	2	3	1	2	3	1	2	3
pH[2]	in	6.6	6.6	6.6	8.0	7.8	7.9	6.9	7.7	7.0
	out	6.3	6.9	6.9	7.9	8.4	8.4	6.6	7.6	7.1
Concentrations [mg/kg(H_2O)][3]										
Si	in	282	321	345	324	293	337	358	335	371
	out	116	102	136	100	108	103	104	101	88
Ω_{Qtz}[4]	in	3.7	4.3	4.6	4.5	4.1	4.7	5.0	4.7	5.2
	out	1.5	1.4	1.8	1.4	1.5	1.4	1.5	1.4	1.2
Al	in	3.0	3.1	3.1	6.5	4.4	5.8	6.7	6.0	7.4
	out	0.2	0.1	0.0	0.1	0.0	0.0	0.1	0.1	0.1
Na	in	3.4	3.5	3.6	9.1	6.7	8.9	7.4	6.9	8.5
	out	1.2	1.0	0.9	3.2	3.6	3.5	0.9	1.4	1.9

[1] Solution sample number.

[2] At room temperature.

[3] in = input solution, out = output solution (solution before and after passing through the precipitation vessel, respectively).

[4] Si saturation ratio with respect to quartz.

Table 2-9 Compositions of the solutions in the experiment of $C_{Al,in}$ = 12 mg/kg(H_2O) (Exp. HAl-12).

Experiment		**HAl-12**							
No.[1]		1	3	4	5	6	7	8	9
pH[2]	in	7.3	7.4	8.1	8.3	8.5	8.3	8.3	8.3
	out	6.9	7.3	7.6	6.9	8.3	8.0	8.1	7.6
Concentrations [mg/kg(H_2O)][3]									
Si	in	166	187	185	186	182	204	197	191
	out	126	131	117	101	118	105	87	87
Ω_{Qtz}[4]	in	2.4	2.8	2.7	2.7	2.7	3.0	2.9	2.8
	out	1.9	1.9	1.7	1.5	1.7	1.5	1.3	1.3
Al	in	12.0	12.6	12.2	12.7	12.6	11.8	11.6	11.4
	out	0.5	0.2	0.2	0.2	0.2	0.1	0.1	0.2
Na	in	13.7	14.3	14.1	14.6	14.3	13.4	13.5	12.9
	out	1.4	2.6	3.1	3.4	3.4	3.4	3.0	2.9
K	in	0.6	0.6	0.6	0.5	0.5	0.4	0.4	0.4
	out	0.1	0.1	0.2	0.2	0.2	0.2	0.1	0.2

[1] Solution sample number.

[2] At room temperature.

[3] in = input solution, out = output solution (solution before and after passing through the precipitation vessel, respectively).

[4] Si saturation ratio with respect to quartz.

Table 2-10 Compositions of the solutions in the experiment of $C_{Al,in}$ = 17 mg/kg(H_2O) (Exp. HAl-17).

Experiment		**HAl-17**								
No.[1]		1	2	3	4	5	6	7	8	9
pH[2]	in	7.1	7.5	7.9	7.5	7.4	7.6	7.8	8.3	8.0
	out	7.6	8.0	8.5	7.5	7.8	8.1	7.6	8.3	7.6
Concentrations [mg/kg(H_2O)][3]										
Si	in	267	238	219	236	227	233	221	218	213
	out	135	107	146	137	153	119	128	127	96
Ω_{Qtz}[4]	in	3.2	2.9	2.7	2.9	2.8	2.8	2.7	2.6	2.6
	out	1.6	1.3	1.8	1.7	1.9	1.4	1.6	1.5	1.2
Al	in	15.3	16.0	17.3	18.1	16.4	17.3	17.6	17.5	17.4
	out	0.8	0.8	0.2	0.2	0.3	0.2	0.2	0.2	0.2
Na	in	17.9	20.3	22.5	24.0	22.6	23.7	24.2	23.8	24.1
	out	3.5	4.5	5.0	5.3	5.1	4.9	5.1	5.2	4.8
K	in	3.1	2.5	2.4	2.4	2.0	1.7	1.6	1.4	1.2
	out	0.2	0.2	0.3	0.3	0.3	0.2	0.3	0.2	0.2

[1] Solution sample number.

[2] At room temperature.

[3] in = input solution, out = output solution (solution before and after passing through the precipitation vessel, respectively).

[4] Si saturation ratio with respect to quartz.

Table 2-11 Compositions of the solutions in the experiment of $C_{Al,in}$ = 29 mg/kg(H_2O) (Exp. HAl-29).

Experiment		**HAl-29**				
No.[1]		1	2	3	4	5
pH[2]	in	-	-	-	-	-
	out	-	-	-	-	-
Concentrations [mg/kg(H_2O)][3]						
Si	in	183	188	187	186	184
	out	108	108	96	103	109
Ω_{Qtz}[4]	in	2.3	2.4	2.4	2.4	2.3
	out	1.4	1.4	1.2	1.3	1.4
Al	in	26.5	33.1	33.0	31.7	21.9
	out	0.1	0.1	0.0	0.0	0.0
Na	in	32.2	54.4	55.4	52.0	31.4
	out	4.5	5.0	5.3	5.8	7.1
K	in	1.3	0.0	0.0	0.0	0.0
	out	0.4	0.0	0.0	0.0	0.0

[1] Solution sample number.

[2] At room temperature.

[3] in = input solution, out = output solution (solution before and after passing through the precipitation vessel, respectively).

[4] Si saturation ratio with respect to quartz.

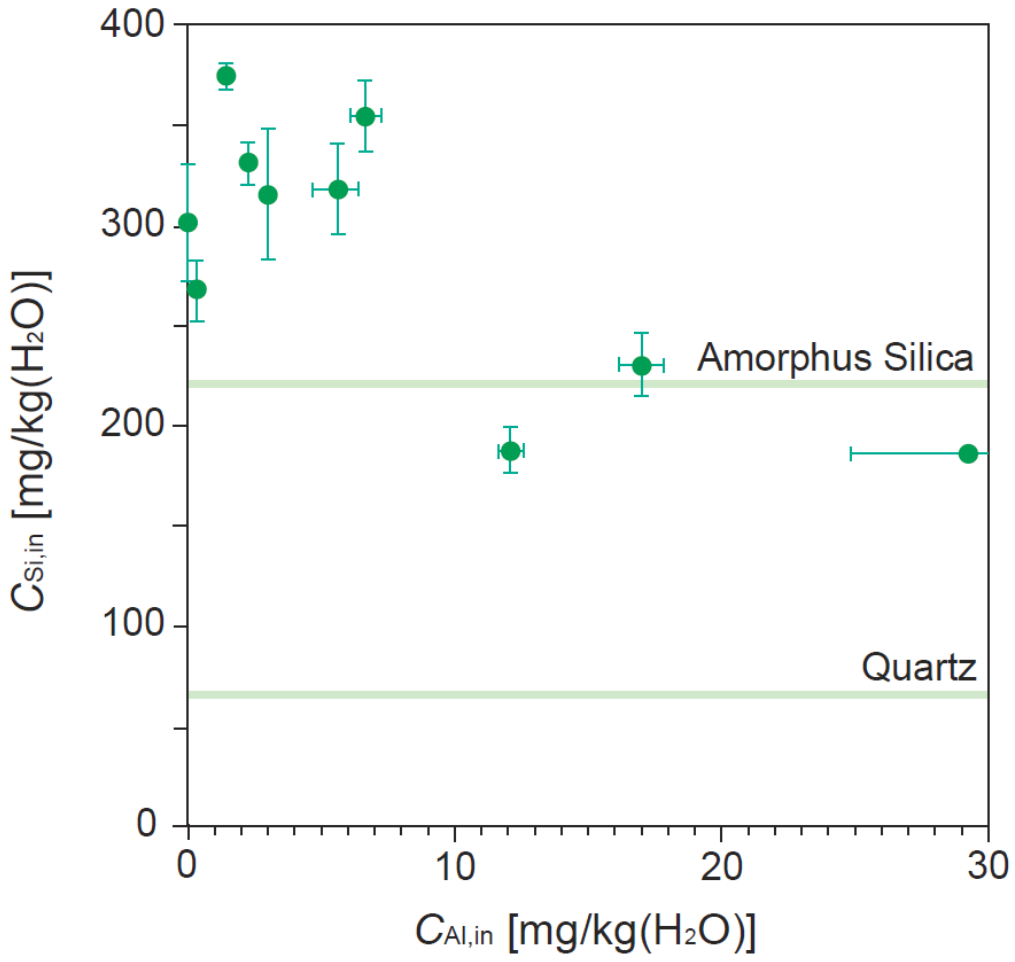

Figure 2-6 Al and Si concentrations in the input solutions, $C_{Al,in}$ and $C_{Si,in}$, respectively. Error bar indicates the standard deviation. Green lines indicate the solubilities of amorphous silica and quartz at 430 °C and 31 MPa.

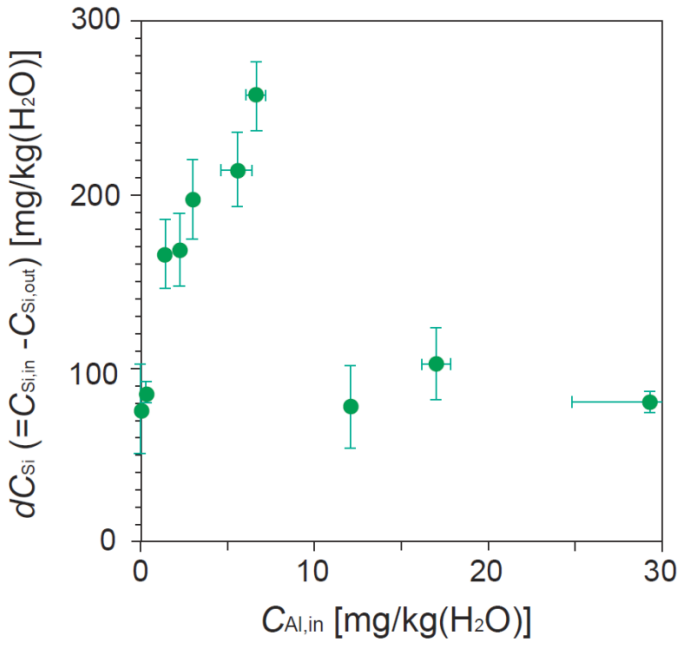

Figure 2-7 Difference of Si concentration between input and output solutions, dC_{Si}, as a function of Al concentration in the input solutions, $C_{Al,in}$.

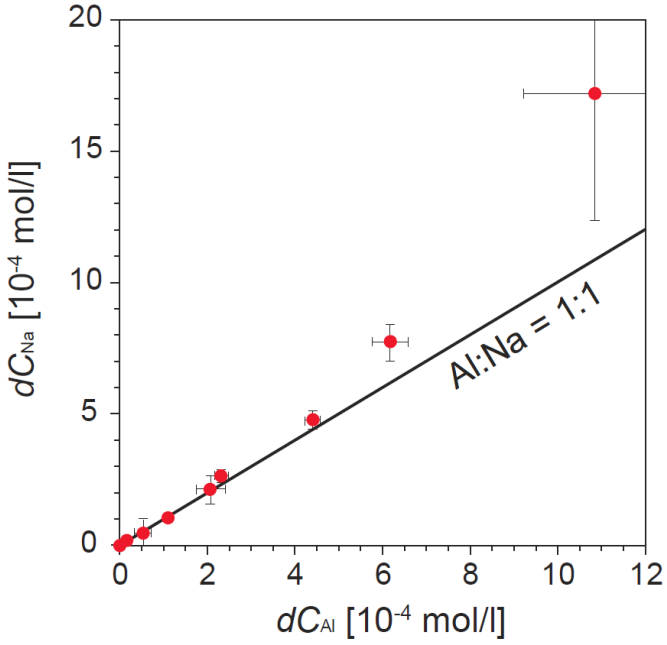

Figure 2-8 Difference of Al concentrations between in the input and output solutions, dC_{Al} (mol/l), versus that of Na concentrations, dC_{Na} (mol/l).

2.4.2.3. Amounts of the precipitated products in the precipitation experiments

The run durations were 76–113 and 202–366 hours in the experiments of $C_{Al,in}$ <10 mg/kg(H_2O) and that of >10 mg/kg(H_2O), respectively (Table 2-5). In the experiments of $C_{Al,in}$ <10 mg/kg(H_2O), the Si concentration in the output solution decreased from the solubility of amorphous silica (220 mg/kg(H_2O)) to that of quartz (77 mg/kg(H_2O)) with increasing of Al concentration in the solution, $C_{Al,in}$, resulting in an increase in the average precipitation rate from 13 to 61 mg/h (Table 2-5; Fig. 2-9). The precipitation rate in the experiments of $C_{Al,in}$ >10 mg/kg(H_2O) was 5–6 mg/h and much less than that of the experiments of $C_{Al,in}$ <10 mg/kg(H_2O) (Table 2-5; Fig. 2-9).

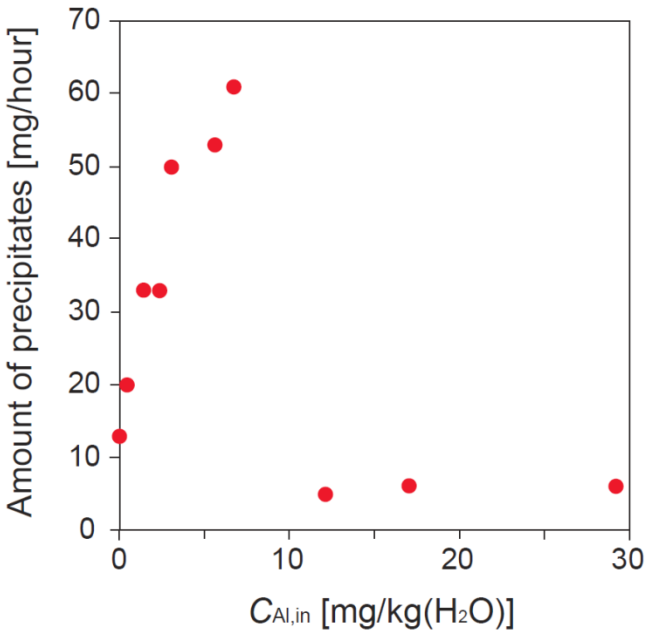

Figure 2-9 Amount of the precipitated products per unit time in the experiments of minor components in the solution.

2.4.2.4. Mineralogy of the precipitated products

In the experiments of Al concentration in the input solution, $C_{Al,in}$, of <1 mg/kg(H_2O), almost products precipitated at around the inlet of the precipitation vessel and covered the entire surfaces of the stainless steel tube. In contrast, few amount of silica precipitation occurred at the downstream of the precipitation vessel. No crystalline mineral was found in XRD analysis and observation of the thin sections. In the solutions of $C_{Al,in}$ = 1, 2, and 3 mg/kg(H_2O), products were collected from the inlet to the outlet of the precipitation vessel. At the part of the T-shaped connection (0–5, 12–16 and 48–52 cm from the inlet), the precipitated product was harder to be collected than that at other parts in the experiments of $C_{Al,in}$ <10 mg/kg(H_2O). In the experiments of $C_{Al,in}$ = 6 and 7 mg/kg(H_2O), large amount of precipitates was corrected at around 10 cm from the inlet (Fig. 2-10a). Products were observed to include crystalline minerals (Fig 2-10b). In the experiments of $C_{Al,in}$ >10 mg/kg(H_2O), almost all of product precipitated from the T-shaped connection at the inlet and ~10 cm from the inlet (Fig. 2-10c). A small amount of precipitates at ~10 cm from the outlet were similar with that in the experiments of $C_{Al,in}$ = 6 and 7 mg/kg(H_2O) (Fig. 2-10d).

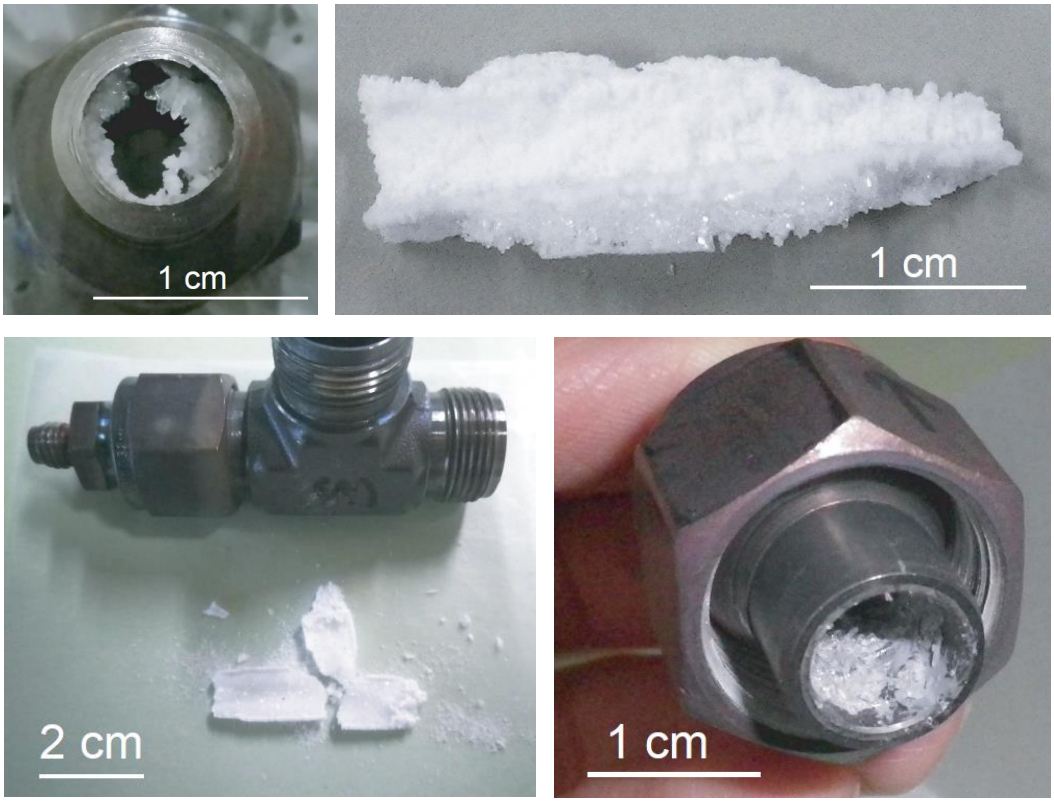

Figure 2-10 Photographs of (a) the cross-section of the precipitation vessel at 8 cm from the inlet in the experiment of $C_{Al,in}$ = 6 mg/kg(H_2O) (Exp. LAl-6), (b) the product precipitated at 11 cm from the inlet in the experiment of $C_{Al,in}$ = 7 mg/kg(H_2O) (Exp. LAl-7), and (c) the product precipitated in the inlet connection and (d) in the outlet connection in the experiment of $C_{Al,in}$ = 12 mg/kg(H_2O) (Exp. HAl-12).

Observations of thin sections and XRD analysis revealed that precipitation of amorphous silica, cristobalite, quartz, albite, and analcite occurred depending on Al concentration in the input solution. Figure 2-14 shows the XRD data (2θ = 20°–30°) of material precipitated at around 10 cm from the inlet of the precipitation tube in each experiment. With increasing Al concentration in the input solutions, $C_{Al,in}$, the dominant silica mineral changed from amorphous silica to cristobalite, quartz, albite and analcite (Fig. 2-14). In the experiments with $C_{Al,in}$ <1 mg/kg(H_2O), the thin section of the precipitated material could not be made because product was a little powder. The precipitated material was white and excluded crystalline minerals. The precipitates from the solution of Al concentration, $C_{Al,in}$, of 0 and 0.4 mg/kg(H_2O) did not show any crystalline peaks in the XRD profiles (Fig. 2-14), indicating that only amorphous silica (opal-A) was present. In the experiments with $C_{Al,in}$ >1 mg/kg(H_2O), amorphous silica and cristobalite predominantly occurred (Figs. 2-11a, b). Cristobalite was commonly composed of a weakly crystallized core and a well-crystallized rim of radially oriented fibrous cristobalite crystals (Fig. 2-11b). The strongest peak of cristobalite is the (1 0 1) diffraction centered 2θ = 21.9°. The peak intensity of cristobalite became larger with increasing of $C_{Al,in}$ from 1 to 3 mg/kg(H_2O) and decreased with increasing of $C_{Al,in}$ to 7 mg/kg(H_2O), whereas that of quartz increases with increasing of $C_{Al,in}$ to 7 mg/kg(H_2O)

(Fig. 2-14). Quartz crystals grew from the vessel wall with *c*-axes preferably oriented perpendicular to the wall, indicating that quartz nuclei settling on the bottom became loci for growth (Figs. 2-11c, 2-12). The largest quartz crystal had an axial length of ~1 mm. The scanning electron microscope-cathodoluminescence (SEM-CL) image showed bright and dark bands in quartz precipitated in the experiment of $C_{Al,in}$ = 7 mg/kg(H_2O) (Fig. 2-12c). In the experiments of $C_{Al,in}$ >10 mg/kg(H_2O), precipitations of albite and analcite were observed in the products whereas the XRD peak intensity of quartz became smaller than that in the experiments of $C_{Al,in}$ <10 mg/kg(H_2O) (Fig. 2-14). In the experiment of $C_{Al,in}$ = 12 mg/kg(H_2O), albite was observed with minor quartz (Fig. 2-14). From the solution of $C_{Al,in}$ = 17 mg/kg(H_2O), analcite precipitated with albite and quartz (Fig. 2-13, 2-14). Precipitation of albite and analcite without quartz occurred in the experiment of $C_{Al,in}$ = 29 mg/kg(H_2O) (Fig. 2-14). The thin sections of the products formed from the solutions of $C_{Al,in}$ = 12 and 17 mg/kg(H_2O), amorphous silica were observed to precipitate above the small crystalline minerals including quartz, albite, and analcite (Fig 2-13).

Based on XRD profile, the values of the relative intensity is shown in Table 2-12 and Fig 2-15. The intensities of first peak of silica minerals (cristobalite and quartz) were compared with the first peak of calcite (29.4°). The intensities of first and second

peaks of albite were used to compare with the calcite peak because these were at near peaks (27.79° and 28.11°) and fluctuation of these peaks caused difficulty to separate each other. The ranges of angles of each XRD data (Fig. 2-14) are 21.90–21.95° as cristobalite (21.98°, (1 0 1) diffraction), 25.89–26.0° as analcite (26.03°, (4 0 0) diffraction), 26.55–26.64° as quartz (26.64°, (1 0 1) diffraction), and 27.72–28.10° as albite (27.80° and 28.10°, (0 4 0) and (0 0 2) diffractions, respectively). For the data of $C_{Al,in}$ = 7 mg/kg(H_2O), the values of the relative intensity were results to be compared with the peak of quartz, which was higher than that of calcite. The intensity of quartz has the maximum value at $C_{Al,in}$ = 7 mg/kg(H_2O), and decreased with increasing of $C_{Al,in}$ over 10 mg/kg(H_2O). Cristobalite had the maximum value at $C_{Al,in}$ = 3 mg/kg(H_2O) and increased again from 6 to 29 mg/kg(H_2O) (Fig. 2-15). Although the peak of 22° is cristobalite, the increase of the peak with increasing of $C_{Al,in}$ from 6 to 29 mg/kg(H_2O) did not indicate cristobalite but albite because the first peak of albite is 22.1° which coexists with the second peak of albite, 28.1°. On the other hand, the peak at around 22° was regarded to show precipitation of cristobalite in the experiments of $C_{Al,in}$ <10 mg/kg(H_2O) because the peak of albite at 28.1° was not observed (Fig. 2-15).

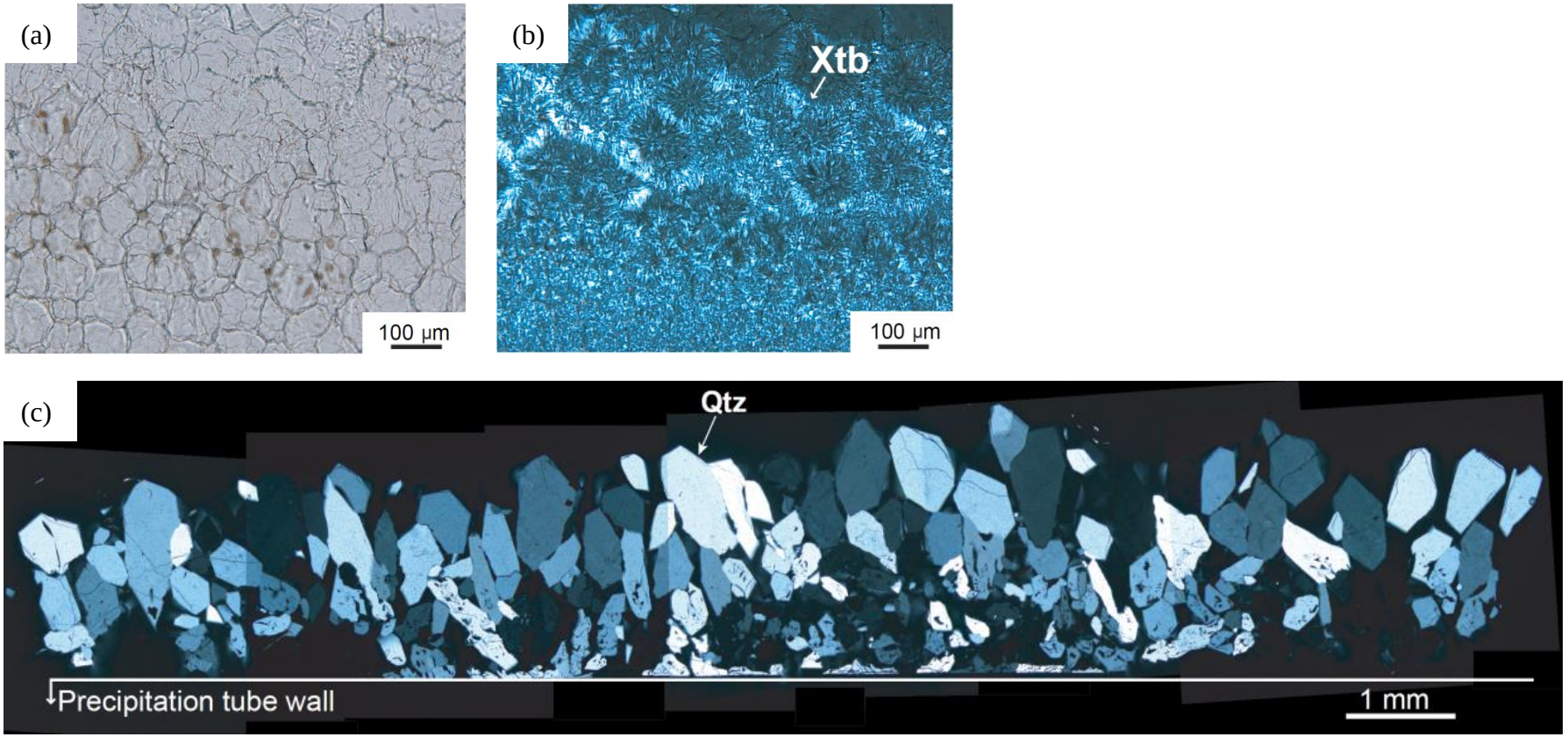

Figure 2-11 Photomicrographs of the thin sections of the precipitated products in the experiments of minor components in the solution. (a) Amorphous silica and cristobalite in the experiment of $C_{Al,in}$ = 1 mg/kg(H_2O) (Exp. LAl-1) under open-polarized and (b) cross-polarized light, and (c) quartz in the experiment of Al concentration in the input solution, $C_{Al,in}$ = 6 mg/kg(H_2O) (Exp. LAl-6) under cross-polarized light.

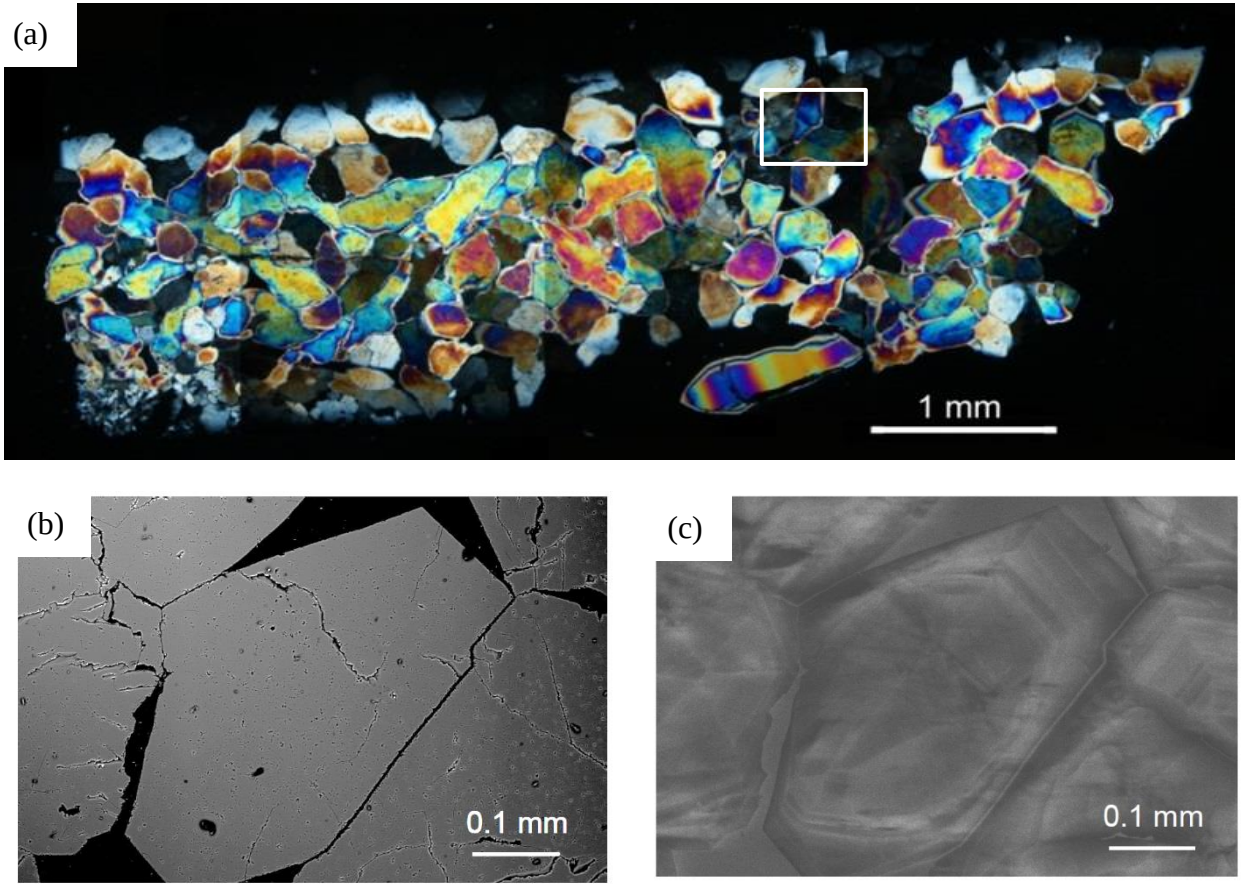

Figure 2-12 The precipitated products at the 10 cm from the inlet in the experiments of $C_{Al,in}$ = 7 mg/kg(H_2O) (Exp. LAl-7) in (a) photomicrograph of precipitated quartz on the precipitation tube wall, and (b) back scatter electron (BSE) and (c) SEM-CL images magnified the area shown by a white box in the photomicrograph (a).

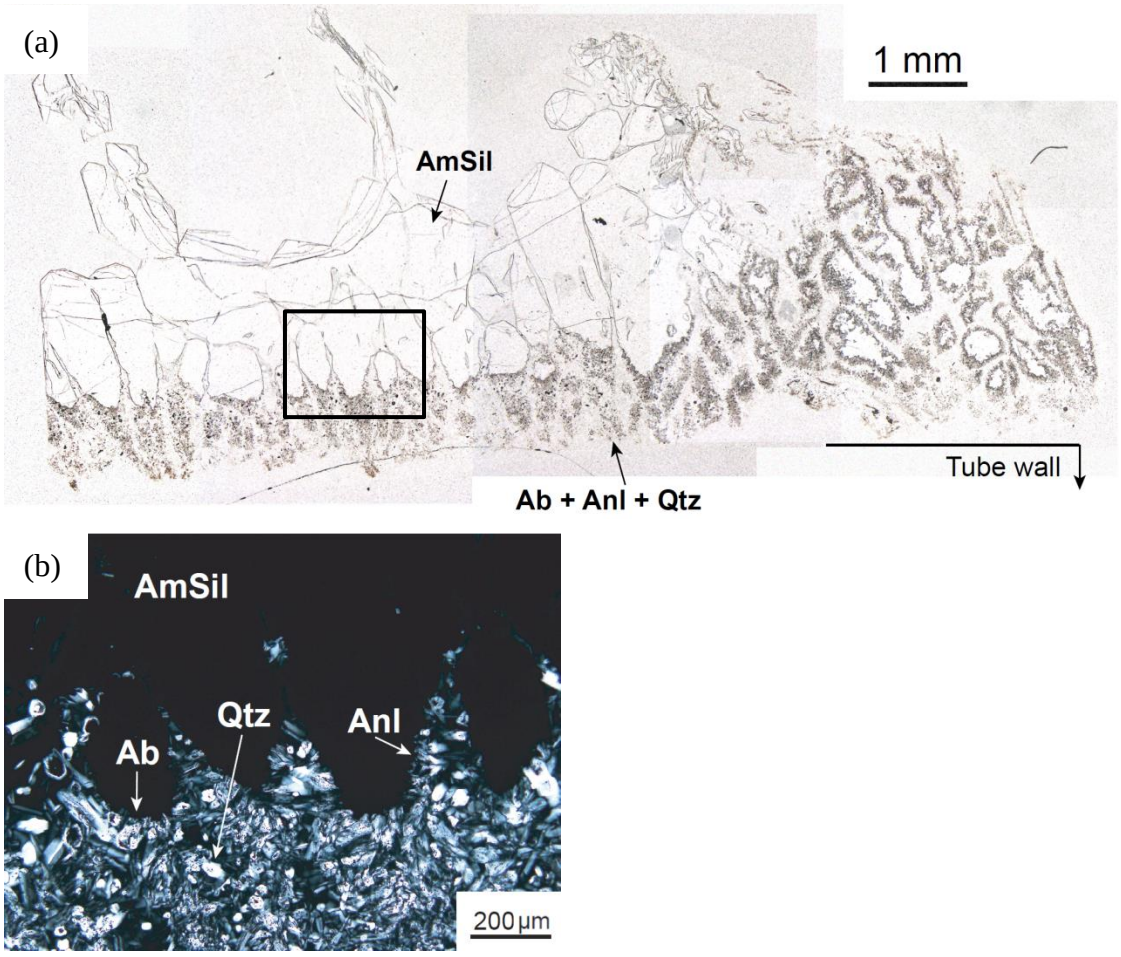

Figure 2-13 Photomicrographs of the thin sections of the precipitated products in the experiments of minor components. (a) Amorphous silica precipitated on albite, analcite, and quartz in the experiment of $C_{Al,in}$ = 17 mg/kg(H_2O) (Exp. HAl-17) under open-polarized and (b) cross-polarized light in the area of a black box in the photo of Fig. 2-13a.

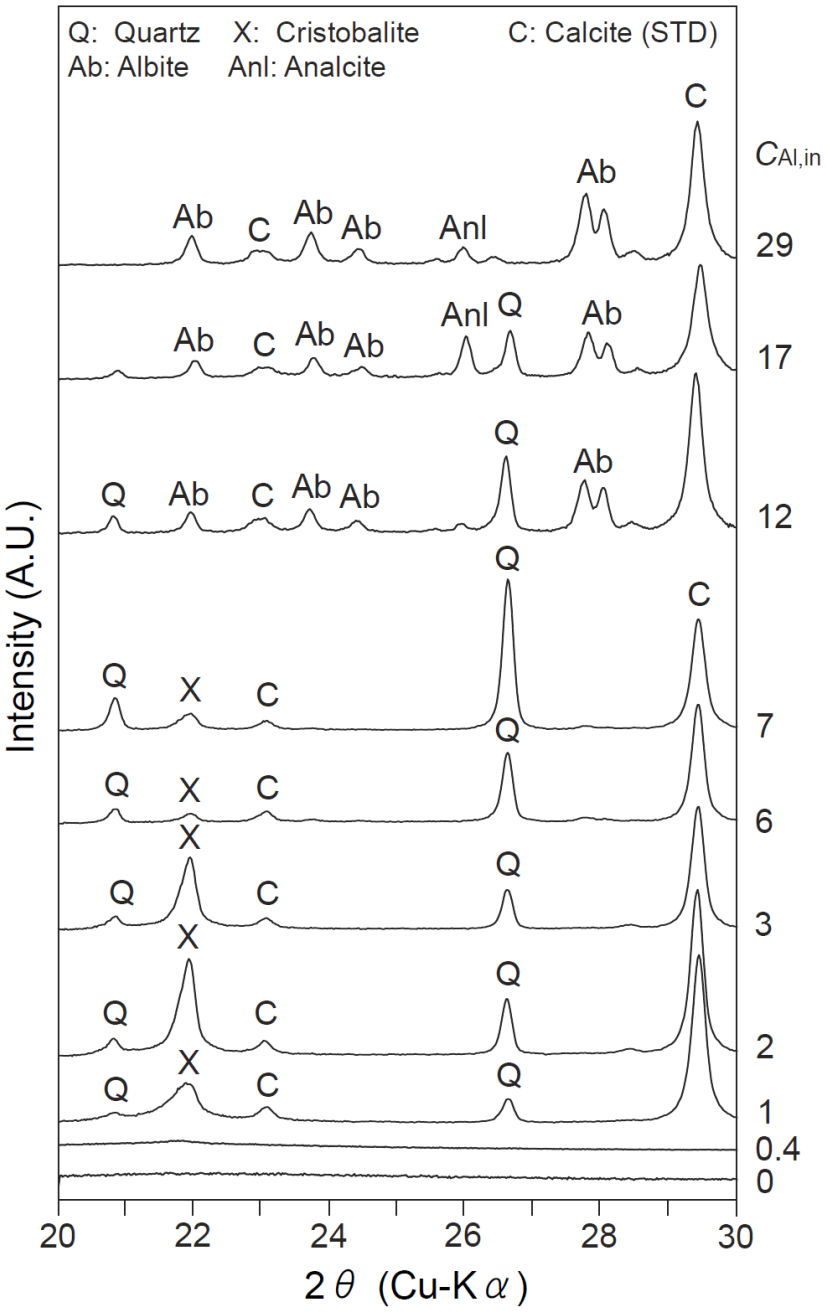

Figure 2-14 XRD results of the precipitated products sampled at ~10 cm from the inlet of precipitation vessels in the experiments of $C_{Al,in}$ = 0–29 mg/kg(H_2O). The degree of XRD analysis was 2θ = 20–30°. Observed precipitated minerals were quartz (Q), cristobalite (X), albite (Ab), and analcite (Anl), respectively. Calcite (C) at 2θ = 29.4° was used as the standard material to estimate the relative intensity.

Table 2-12 XRD results of the intensities and the relative intensities.

$C_{Al,in}$ [mg/kg(H_2O)][1]	2θ [deg]	Intensity [cps][2]	Relative intensity [%][2]
1.2	21.93	556	20
1.2	26.62	410	15
2.3	21.94	960	36
2.3	26.61	586	22
3.0	21.93	1460	52
3.0	26.60	991	35
5.6	21.90	142	7
5.6	26.61	1197	61
5.6	27.76	54	3
6.7	21.95	235	9
6.7	26.61	2605	100
6.7	27.75	41	2
12	21.95	160	12
12	25.89	67	5
12	26.56	646	49
12	27.73	377	29
12	28.01	351	27
17	22.00	141	16
17	26.00	338	38
17	26.64	391	44
17	27.81	333	37
17	28.08	257	29
30	21.95	234	21
30	25.94	123	11
30	27.78	558	51
30	28.05	446	40
30	29.08	26	2

[1] Al concentration in the input solutions in Table 2-6.

[2] Estimated by using the software Rigaku PDXL (Regaku, Tohoku University, Japan).

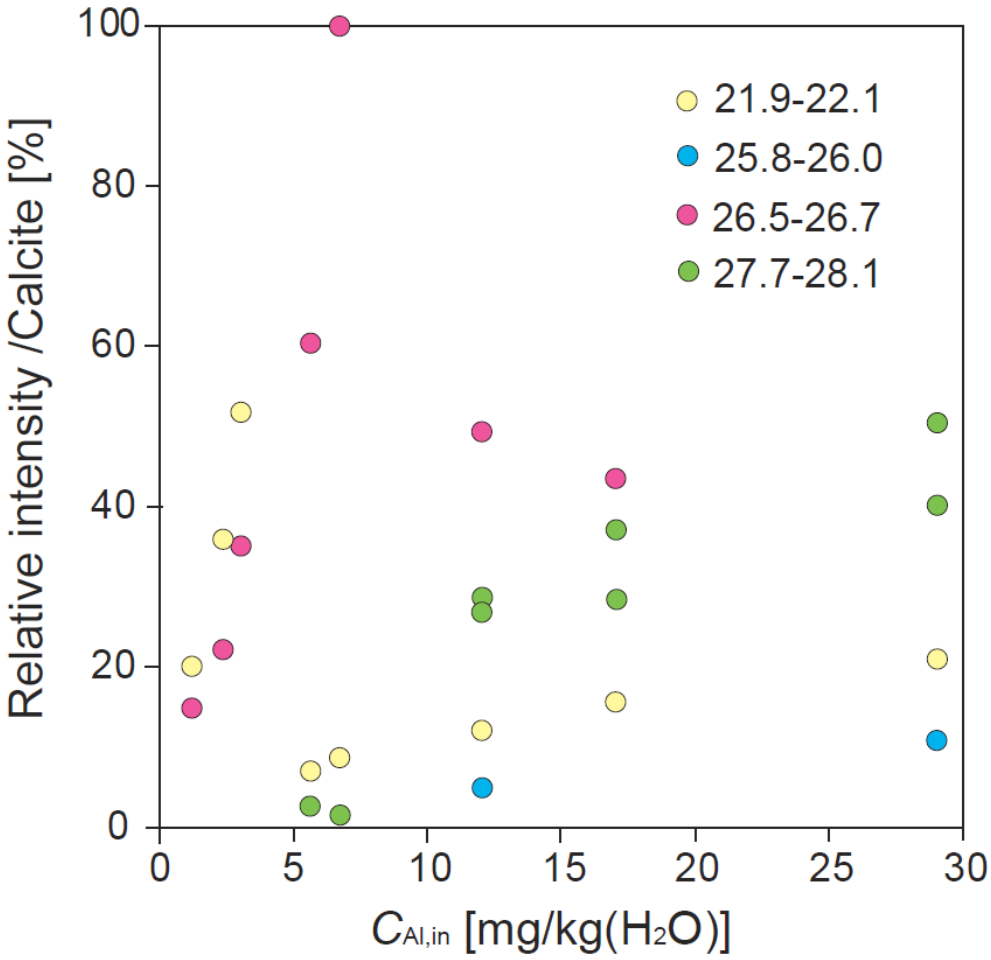

Figure 2-15 Relative intensities of XRD peaks observed in the precipitated products from the solutions of $C_{Al,in}$ = 0–29 mg/kg(H_2O). The standard material was calcite (29.4°). Peaks are at 2θ = 21.9–22.1° as cristobalite (21.9°; yellow circles), 25.8–26.0° as analcite (25.96° and 25.98°; blue circles), 26.55–26.64° as quartz (26.64°; red circles), and 27.72–28.10° as albite (27.79° and 28.11°; green circles), respectively.

The Al and Na contents of precipitated silica minerals were measured by EPMA. Figure 2-16 shows the results of precipitated products analyzed by EPMA of Tokyo University. Amounts of Al and Na in the products were variable even within individual experiments. The Al and Na contents of amorphous silica and cristobalite in the experiments of $C_{Al,in}$ = 1 and 2 mg/kg(H_2O) were under the detection limits of Al (<240 mg/kg) and Na (<209 mg/kg) of EPMA analyses, whereas the Na and Al contents of quartz in the experiments of $C_{Al,in}$ = 3–7 mg/kg(H_2O) were mostly higher than their respective detection limits, yielding a positive correlation between Al and Na contents (Fig. 2-16).

The Al and Na contents of precipitated silica minerals in the experiments of $C_{Al,in}$ = 2 and 7 mg/kg(H_2O) were also observed by EPMA of University of Oregon with the detection limits of under 10 mg/kg. In the precipitates of the experiment of $C_{Al,in}$ = 2 mg/kg(H_2O), observation of an euhedral product, which seemed to be quartz (Fig. 2-17a, b) showed that the Al concentration correlated with that of Na at 20, 70, 180, and 210 μm from the start point (Fig. 2-17c). In the precipitated products of the experiment of $C_{Al,in}$ = 7 mg/kg(H_2O), larger amount of Al and Na in quartz correlated with bright bands of SEM-CL image (Fig. 2-18a, b) at the point of 35, 77, and 105 μm from the start point (Fig. 2-18c).

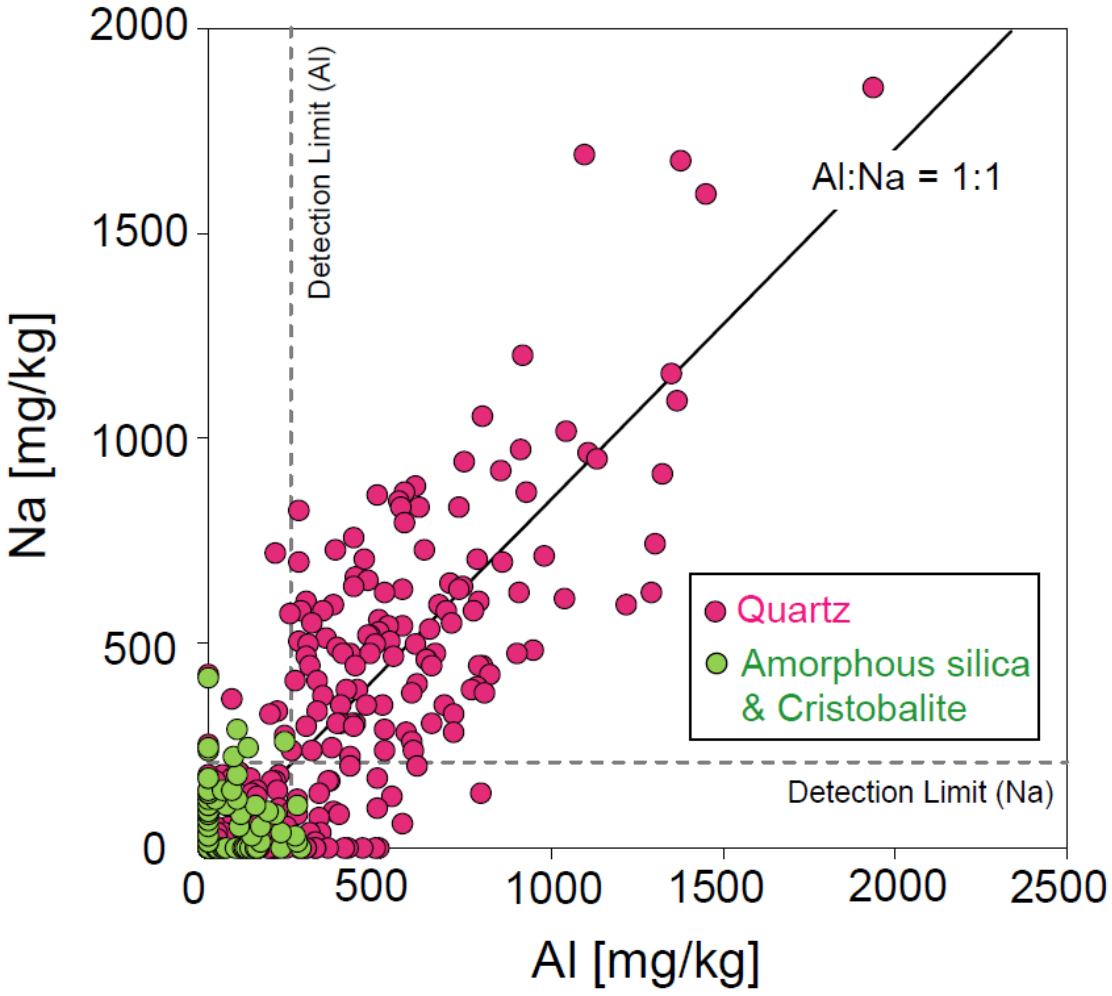

Figure 2-16 The Al and Na contents (mg/kg) in the products: Amorphous silica and cristobalite from experiments with $C_{Al,in}$ = 1 and 2 mg/kg(H_2O) (green circles) and quartz from experiments with $C_{Al,in}$ = 3, 6, and 7 mg/kg(H_2O) (red circles). The gray dashed lines indicate the detection limits of Al (<240 mg/kg) and Na (<209 mg/kg) by EPMA.

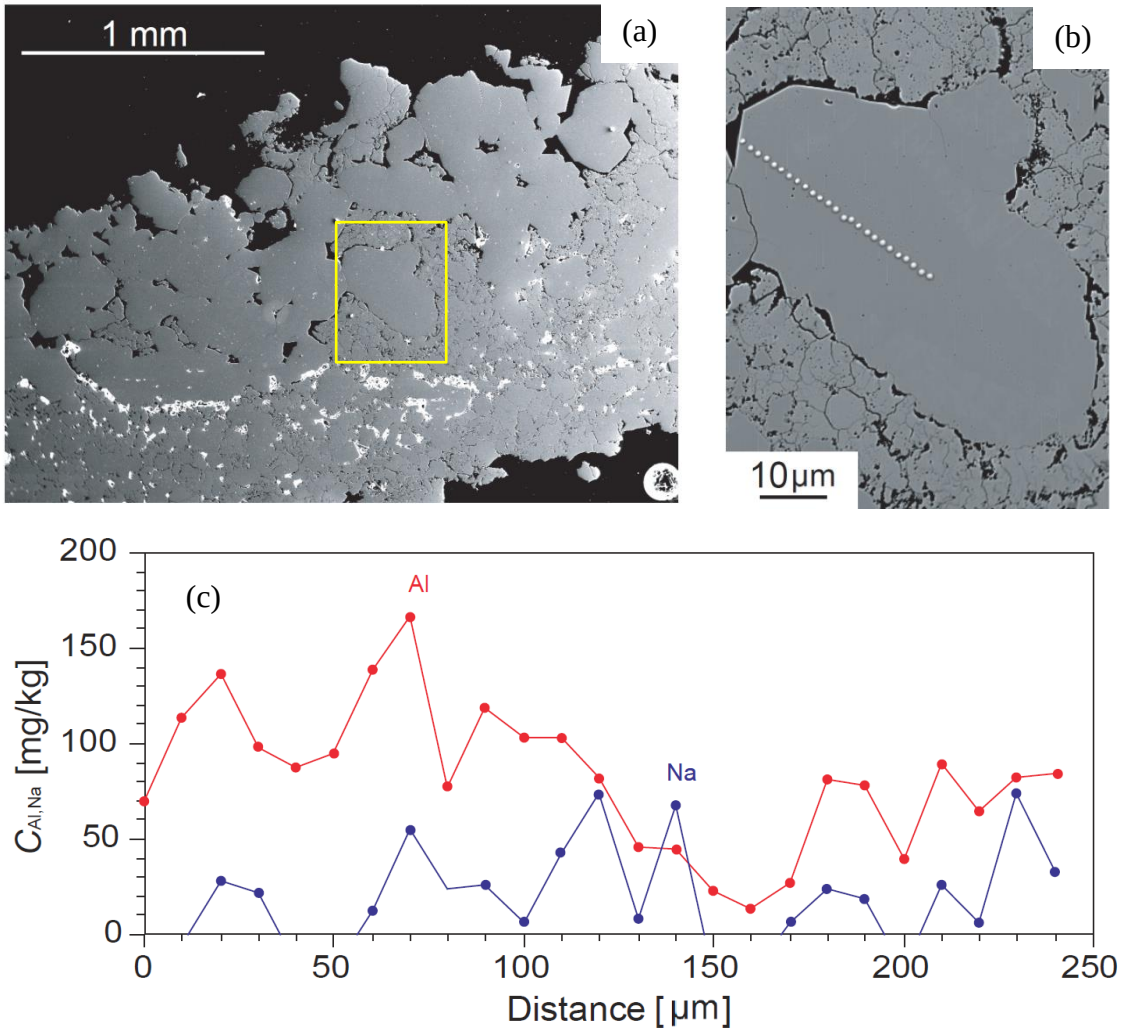

Figure 2-17 (a) SEM image of the precipitated products in the experiment of $C_{Al,in}$ = 2 mg/kg(H_2O) (Exp. LAl-2), (b) the line of EPMA analysis at the area of Fig. 2-17a (a yellow box), and (c) Al (red line) and Na (blue line) concentrations along the line of Fig. 2-17b.

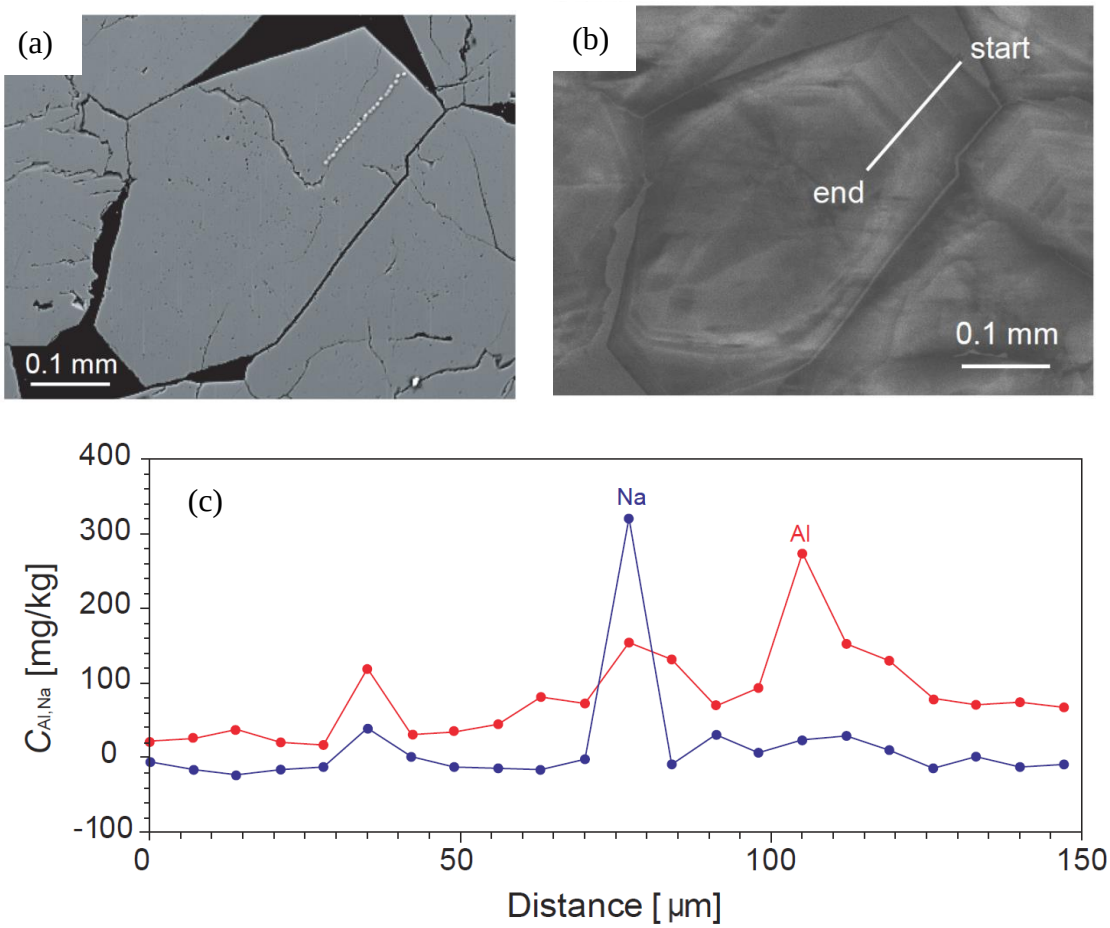

Figure 2-18 (a) SEM image of quartz in the experiments of $C_{Al,in}$ = 7 mg/kg(H_2O) (Exp. LAl-7) after EPMA analysis and (b) SEM-CL image of Fig. 2-18a with the line of EPMA analysis at the area of Fig. 2-10a. (c) Al (red line) and Na (blue line) concentrations along the line of Fig. 2-18a, and b.

2.4.3. Discussion

2.4.3.1. Compositions of the input solutions

In the experiments of albite dissolution, the ratio of Na and Al concentrations in the solution, Na/Al, ranged from 1.2 to 1.6 in the flow rate of 1.0 g/min (Table 2-3). In addition, the ratio of Al and Si concentrations in the solution, Al/Si, ranged from 0.26 to 0.31 in the flow rate of 1.0 g/min (Table 2-3). The ratio of Al and Si at temperature >200 °C correlated with stoichiometry of albite, Al/Si = 0.3, indicating the occurrence of stoichiometric dissolution of albite in this experiments. In the condition of temperature ≤200 °C, the ratio of Al and Si was lower than that expected by stoichiometry of albite perhaps because flow rate (2.0 g/min) was double of that in experiments of >200 °C (Table 2-3). These results suggest that congruent dissolution of albite occurred in the experiments of the flow rate of 1.0 g/min. In the experiments of the flow rate of 2.0 g/min, however, these ratios of components imply that the incongruent dissolution of albite, which might because the flow rate (and the residence time in the dissolution vessel) was not enough for the congruent reaction of albite sand.

2.4.3.2. The effect of Al and Na in the solution on mineralogy of silica precipitation

The correlation between Al and Na in the solutions (Fig. 2-8) and in the precipitated products (Fig. 2-16), indicating that Al was incorporated into quartz mainly by the substitution $Si^{4+} = Al^{3+} + Na^{+}$. This interpretation is consistent with previous findings that the extra electrical charge derived from the substitution of Al^{3+} for Si^{4+} in the quartz Si-O tetrahedron lattice is compensated for by an interstitial monovalent cation (e.g., Monecke *et al*., 2002). Amount of Al and Na in quartz correlated with CL intensity, indicating that the bright zones of SEM-CL images in quartz were caused by distribution of Al and Na in precipitated quartz (Fig. 2-18c). SEM-CL textures of quartz have been regarded as the result of fluctuation of temperature, compositions of fluid, or precipitation rate (Rusk and Reed, 2002; Wilkinson *et al.*, 1999). However, no temporal changes in fluid chemistry of input solutions and temperature were observed in this study (Table 2-5).

In the experiments of Al concentration in the input solution, $C_{Al,in}$, of 6 and 7 mg/kg(H_2O), no relics of amorphous silica was found within quartz crystals (Figs. 2-11c, 2-12a). These findings indicated that the products of these experiments resulted from the direct nucleation of quartz rather than recrystallization processes. The theoretical homogeneous nucleation of quartz is difficult to occur at room temperature due to the

high interfacial energy between quartz and water (Steefel and Van Cappellen, 1990). However, the strong temperature dependence of silica precipitation was revealed because of lower surface energy of quartz at higher temperature (>400 °C at 24 and 30 MPa) in the hydrothermal experiments in the chapter 2.2. Alekseyev *et al*. (2009) suggested that the temporal change of Si concentration in step, which was similar to the solubilities of amorphous silica, α-, and β-cristobalite, reflected that silica does not directly precipitate as quartz but forms initially metastable silica modifications, which change each other in accordance with Ostwald's rule even in the precipitation experiments of 200–300 °C with quartz seeds. In their experiments, the quartz glass was used to obtain silica-oversaturated solutions without minor components. In this study, on the other hand, the experiments of minor components in the solution indicated that the presence of Al^{3+} and Na^{+} in solution could be also one of the factors to reduce the energetic barrier of quartz nucleation. In addition, the formation of Na-Al and Na-Al-Si complexing in solutions (Newton and Manning, 2008) may be associated with quartz nucleation. Further detailed experimental studies will be required for understanding the mechanism of direct nucleation of quartz.

2.4.3.3. Precipitation of albite and analcite

In the experiments of Al concentration in the input solution, $C_{Al,in}$, of <1 mg/kg(H_2O), amorphous silica precipitated without any transformation to other minerals (Fig. 2-14). In the experiments of $C_{Al,in}$ = 1–3 mg/kg(H_2O), cristobalite was observed in amorphous silica (Fig. 2-11b), perhaps indicating that cristobalite nucleated and be introduced in amorphous silica, or amorphous silica precipitated on the tube wall and then transformed to cristobalite in time. In the experiments of $C_{Al,in}$ >10 mg/kg(H_2O), the ratio of the difference of Al and Na in the input and output solutions was similar with that in the experiments of $C_{Al,in}$ <10 mg/kg(H_2O) except that in the experiments of $C_{Al,in}$ = 29 mg/kg(H_2O) (Fig. 2-8), indicating that Al with Na was incorporated into precipitated product. Precipitation of albite in water is as follows:

$$NaAlSi_3O_8 + 4H_2O + 4H^+ \rightarrow Na^+ + Al^{3+} + 3H_4SiO_4. \quad (21)$$

Because the input solution made by dissolution of albite and silica minerals (quartz or amorphous silica), precipitation of analcite was suspected to occur by using Al, Na, and Si in the solution from albite and silica minerals as follows:

$$NaAlSi_3O_8 + SiO_2 + 5H_2O \rightarrow NaAlSi_2O_6 \cdot H_2O + 2H_4SiO_4 . \quad (22)$$

The saturation index, which is the logarithmic value of a reaction quotient, Q, versus an equilibrium constant, K ($\log_{10}$ (Q/K)), for precipitation of albite and analcite was calculated by using the program SOLVEQ-XPT developed by Reed *et al.* (2010). The *PT* condition was 430 °C and 35 MPa similar to that of the experiments. In the condition of the experiments, 430 °C and 30 MPa, calculation of SOLVEQ-XPT could not work probably because of lack of the reliable thermodynamic dataset in this condition.

Si concentration was set 100, 200, and 300 mg/kg(H_2O). Al and Na concentrations were same each other, 0, 3, 7, 10, 12, 17, and 30 mg/kg(H_2O). For taking a balance of ion charge, SO_4^{2-} was added in 0.01 mg/kg(H_2O) because S could be in SUS316 tube and dissolve in the solution during run. Minerals are supersaturated if $\log_{10}$ (Q/K) >0, exactly saturated if $\log_{10}$ (Q/K) = 0, and undersaturated if $\log_{10}$ (Q/K) <0. Albite and analcite are supersaturated in the solution of C_{Si} = 200 mg/kg(H_2O) and C_{Al} and C_{Na} >10 mg/kg(H_2O) (Fig. 2-19), indicating that these minerals possibly precipitates in the experiments of $C_{Al,in}$ >10 mg/kg(H_2O) (Figs. 2-13, 2-14). In addition, albite becomes supersaturated with increasing of C_{Al} and C_{Na} >2 mg/kg(H_2O) in the solution of C_{Si} =

300 mg/kg(H_2O) (Fig. 2-19a). Analcite is also supersaturated in the solution of Si = 300 mg/kg(H_2O) and concentrations of Al and Na are higher than 4 mg/kg(H_2O) (Fig. 2-19b), whereas the saturation index of analcite is always lower than that of albite in the same condition (Fig. 2-19).

In the experiments of temperature dependence, the Al and Na concentrations were under 5 mg/kg(H_2O) at a maximum in the input solutions made by dissolution of granite sand (Tables 2-1, 2-2). Silica precipitation at the permeable zone in the continental plates of the Earth's crust may occur mainly in the condition of the solution of C_{Al} <5 mg/kg(H_2O) because granite is usually found there. In the solution of $C_{Al,in}$ <10 mg/kg(H_2O), albite and analcite also could precipitate (Fig. 2-19), whereas these were not detected in the precipitated products in this study (Fig. 2-14). When the total amount of Al and Na in the solution is less than 10 mg/kg(H_2O), Al and Na may be relatively distributed into not precipitation of albite and analcite but quartz, which can nucleate directly with Al^{3+} and Na^{+} (Fig. 2-16).

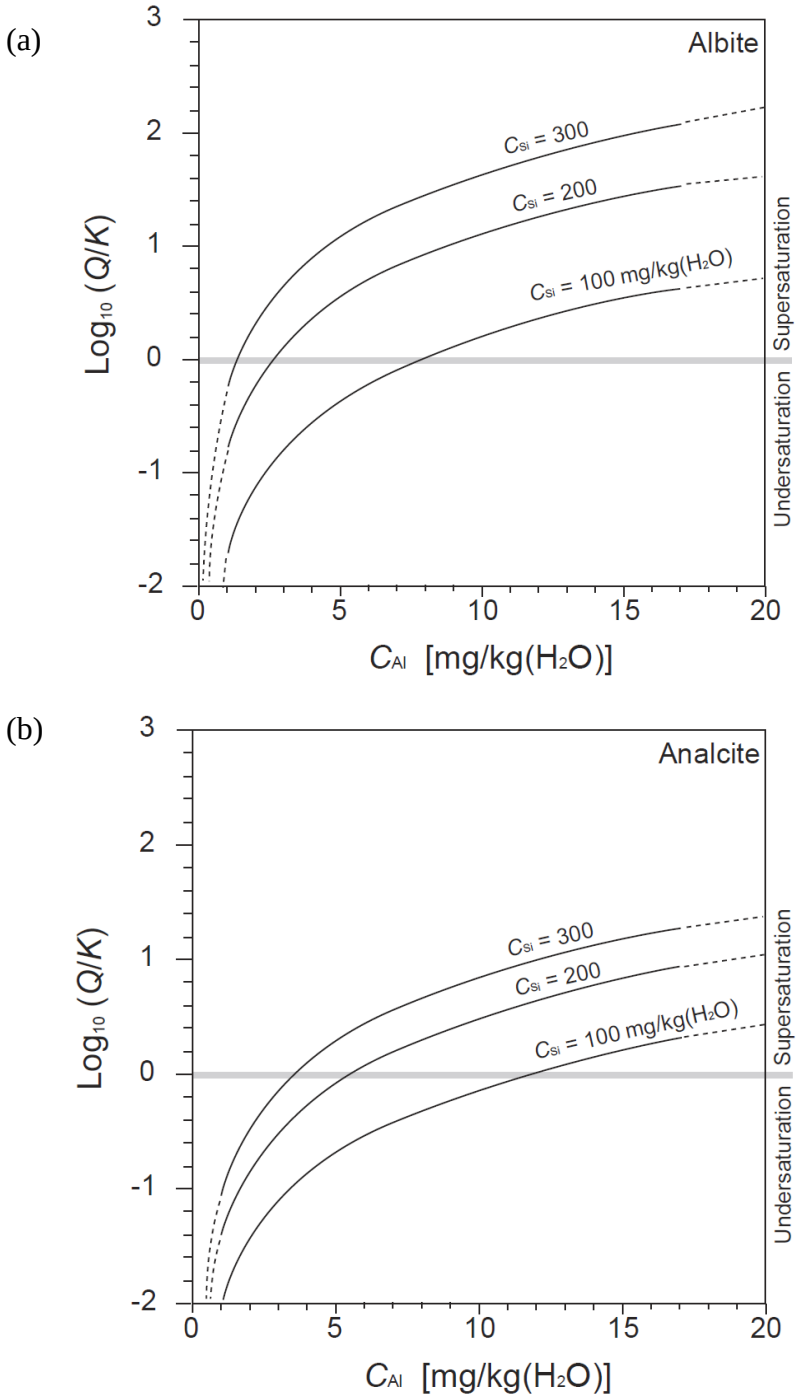

Figure 2-19 The saturation index, $\log_{10}$ (Q/K), of (a) albite, and (b) analcite at 430 °C and 35 MPa. Minerals are supersaturated if $\log_{10}$ (Q/K) >0, exactly saturated if $\log_{10}$ (Q/K) = 0, and undersaturated if $\log_{10}$ (Q/K) <0. Concentrations of Si, C_{Si}, is 100, 200, 300 mg/kg(H_2O).

2.5. Conclusions

The hydrothermal flow-through experiments were conducted to reveal the effect of temperature and minor components in the solution on silica precipitation.

Large amount of silica precipitation occurred via nucleation in the supercritical region whereas less precipitation of silica minerals were observed in the liquid region. The onset of the homogeneous nucleation at 390 °C can be reproduced when the surface energy of quartz is 130 mJ/m^2, which is similar to the estimated value from greenschist-facies metapelites (145 mJ/m^2; Hiraga *et al*., 2002).

In the experiments of minor components in the solution, the XRD results and the observations of the synthesized materials revealed that dominant precipitates changed from amorphous silica, to cristobalite, quartz, and albite and analcite with increasing of concentrations of Al and Na in the input solution from 0 to 29 mg/kg(H_2O). Amount of precipitates increased with increasing of Al concentration in the input solution from 0 to 7 mg/kg(H_2O). The positive correlations of difference of Al and Na concentrations between the input and output solutions and Al and Na contents in precipitated quartz indicated that the presence of Al^{3+} and Na^{+} in solution might reduce the energetic barrier of quartz nucleation, and Al was incorporated into quartz mainly by the substitution $Si^{4+} = Al^{3+} + Na^{+}$.

3. THE KINETIC EQUATION OF OVERALL SILICA PRECIPITATION

3.1. Introduction

The kinetics of dissolution and precipitation of silica minerals is important to reveal the geochemical reaction and to estimate how long silica deposits forms in the Earth's crust or into pipelines of geothermal plants. A differential rate equation for silica-water reactions from 0 to 300 °C was determined by Rimstidt and Barnes (1980) (Eq. 16 shown in the chapter 1). Dissolution results positive (increase of C_{Si} per unit time) and precipitation is negative reaction. If the solution of $C_{Si,in}$ flows through a system, Si concentration at output of a system, $C_{Si,out}$, is calculated as follows:

$$\int \frac{dC_{Si}}{(C_{Si,Qtz,eq} - C_{Si})} = \frac{A_{Qtz}}{M_{H_2O}} k_S \int dt \tag{23}$$

$$-\ln \frac{C_{Si,Qtz,eq} - C_{Si,out}}{C_{Si,Qtz,eq} - C_{Si,in}} = -\ln \frac{1-\Omega_{Si,out}}{1-\Omega_{Si,in}} = \frac{A_{Qtz}}{M_{H_2O}} k_S t \tag{24}$$

$$C_{Si,out} = \left(C_{Si,in} - C_{Si,Qtz,eq}\right) \exp\left(\frac{-A_{Qtz}}{M_{H_2O}} k_S t\right) + C_{Si,Qtz,eq}. \tag{25}$$

where C_{Si} is the concentration of Si (mg/kg(H_2O)), t is time (sec), k_S is the reaction rate constant (kg m^{-2} sec^{-1}), A_{Qtz} is the reaction surface area of quartz (m^2), M_{H_2O} is the mass of water in the system (kg), and $C_{Si,Qtz,eq}$ is the solubility of quartz, Si (mg/kg(H_2O)).

This previous kinetic equation is still not enough to estimate precipitation rate of silica minerals under crustal conditions. Rimstidt and Barnes (1980) suggested that the activation energy for dissolution of silica polymorphs is due to the breaking of strong Si-O bands. However, precipitation rate is same for silica polymorphs, which are simply related by their free energies. In the low Si saturated solution, Ω_{Qtz} = 1.0–1.2, the quartz seeds or substrates in the experimental system causes the smaller surface energy for quartz growth than that of nucleation of other silica polymorphs (Rimstidt and Barnes, 1980; Bird *et al*., 1986). On the other hand, if the Si concentration in the solution is enough for nucleation of silica polymorphs, amorphous silica could form initially because the interfacial energy of amorphous silica (46 mJ/m^2) is much smaller than that of quartz (350 mJ/m^2) at room temperature (Alexander, 1957; Parks, 1984). The precipitation experiments of the high Si supersaturated solution, Ω_{Qtz} >2, showed the initial formation of metastable silica modifications (Alekseyev *et al*., 2009, 2010) and co-precipitation of silica minerals via nucleation of quartz, amorphous silica and

cristobalite (Okamoto *et al*., 2010). The experiments of minor components in this study also showed that the euhedral quartz crystals precipitates without precursor of silica polymorphs from the solution with minor components (Al and Na) (Figs. 2-11c, 2-12a).

As noted above, co-precipitation of quartz growth and nucleation of silica polymorphs of not only amorphous silica but also quartz is possible in the crustal fluid, which includes many components dissolved from rocks. In this chapter, the overall precipitation rate of silica minerals is derived empirically to estimate amount of silica precipitation within the Earth's crust.

3.2. Derivation of the new kinetic equation

In this study, the new kinetic equation of surface reaction and nucleation of silica minerals is proposed as follows:

$$\frac{\partial C_{\mathrm{Si}}}{\partial t} = \frac{A_{\mathrm{Qtz}}}{M} k_{\mathrm{S}} \left(C_{\mathrm{Si,Qtz,eq}} - C_{\mathrm{Si}} \right) + \alpha k_{\mathrm{N}} \left(C_{\mathrm{Si,Qtz,eq}} - C_{\mathrm{Si}} \right)^{n} \tag{26}$$

where α is a nucleation parameter reflected with the possibility of occurrence of nucleation of silica minerals, and k_{S} and k_{N} is the reaction rate constant related with

surface reaction (quartz dissolution and quartz growth on quartz surfaces) and nucleation of silica minerals, respectively. The first term represents the kinetic equation of surface reaction proposed by Rimstidt and Barnes (1980) (Eq. 16). The rate constant of surface reaction is as follows (Okamoto *et al*., 2010):

$$\mathrm{Log}k_S = -0.0886 - 2638/T \tag{27}$$

where T is temperature in Kelvin. In this study, the second term is added to estimate precipitation rate related to nucleation, which could occur even in the system without quartz surfaces ($A_{\mathrm{Qtz}} = 0\ \mathrm{m}^2$).

The three parameters, n, α, and k_{N}, in the second term of Eq. 26 are derived empirically in this chapter. First parameter is the order of reaction, n. Rimstidt and Barnes (1980) determined the kinetic equation of silica minerals (Eq. 16) based on the data of dissolution experiments. For phenomenological treatments of reaction kinetics, the reaction rate orders are empirical. The reaction order in the second term is also determined by integral methods based on the precipitation experiments in the condition that only nucleation occurs.

Second parameter is a nucleation parameter, α, which indicates the possibility of nucleation of silica minerals. Si saturation ratio with respect to quartz and temperature are controlling parameters to change nucleation rate drastically. Steefel and Van Capperen (1990) suggested the nucleation of amorphous silica is a dominant reaction rather than that of quartz at 25 °C. However, the precipitation experiments in this study showed quartz precipitation via nucleation in the solution including minor components (Al and Na) (Figs. 2-11c, 2-12a), indicating that quartz nucleation could occur from the crustal fluid. In addition, the strong dependence of temperature on silica precipitation via nucleation was also revealed in this study (Fig. 2-2). Thus, a nucleation parameter, α, is derived by the conditions of Si concentration in the solution and temperature.

Third parameter is the nucleation rate constant, k_N, which is derived as a function of Al concentration in the solution. In the experiments of minor components in the solution, difference of Si concentrations in the input and output solutions and amount of precipitation per unit time depended on Al concentrations in the input solutions, indicating that precipitation rate is affected by minor components in the solution (Figs. 2-7, 2-9). Mineralogy of precipitation also changed depending on Al concentration in the solution (Fig. 2-14). These observations may suggest that the apparent solubility changes in each condition depending on mineralogy of precipitation. In the new kinetic

equation, however, only the quartz solubility is applied in the second term of Eq. 26 to simplify the form of the equation. The activation energy of quartz (67.4–76.6 kJ/mol) is lower than that of amorphous silica and cristobalite, 60.9–64.9, 65.0–68.7 kJ/mol, respectively. Therefore, the solubility of quartz is lower than that of amorphous silica and cristobalite at any temperature (Rimstidt and Barnes, 1980; Fig. 1-6b). The solubility of quartz could cover the reaction of both quartz growth and nucleation of silica polymorphs from the low and high Si supersaturated solutions, respectively.

3.3. Order of precipitation

The integral method (Laidler, 1987; Brantley, 2007) was applied to determining the reaction order of precipitation of silica minerals in fluids, *n*. Eq. 26 is rewritten for silica precipitation without quartz surfaces (A_{Qtz} = 0 m^2) as follows:

$$\frac{\partial C_{Si}}{\partial t} = k_N \left(C_{Si,Qtz,eq} - C_{Si} \right)^n . \quad (28)$$

The integrated value is calculated depending on orders from 1 to 4 as follows:

$$n = 1 \qquad -\ln\left(\frac{C_{\mathrm{Si,out}} - C_{\mathrm{Si,Qtz,eq}}}{C_{\mathrm{Si,in}} - C_{\mathrm{Si,Qtz,eq}}}\right) = k_{\mathrm{N}}t \tag{29}$$

$$n = 2 \qquad \left(C_{\mathrm{Si,out}} - C_{\mathrm{Si,Qtz,eq}}\right)^{-1} - \left(C_{\mathrm{Si,in}} - C_{\mathrm{Si,Qtz,eq}}\right)^{-1} = k_{\mathrm{N}}t \tag{30}$$

$$n = 3 \qquad \frac{1}{2}\left\{\left(C_{\mathrm{Si,out}} - C_{\mathrm{Si,Qtz,eq}}\right)^{-2} - \left(C_{\mathrm{Si,in}} - C_{\mathrm{Si,Qtz,eq}}\right)^{-2}\right\} = k_{\mathrm{N}}t \tag{31}$$

$$n = 4 \qquad \frac{1}{3}\left\{\left(C_{\mathrm{Si,out}} - C_{\mathrm{Si,Qtz,eq}}\right)^{-3} - \left(C_{\mathrm{Si,in}} - C_{\mathrm{Si,Qtz,eq}}\right)^{-3}\right\} = k_{\mathrm{N}}t \tag{32}$$

where $C_{\mathrm{Si,in}}$, $C_{\mathrm{Si,out}}$ and $C_{\mathrm{Si,Qtz,eq}}$ is the Si concentration in the input and output solutions and quartz solubility, respectively.

The validity of the reaction order, *n*, can be identified by the linear relation between time and the value of left side of Eqs. 29–32. The slop of the plot represents the value of the rate constant and the intercept is zero because precipitation does not occur in time zero. In this study, however, the intercept of the linear line was not zero reflecting precipitation via nucleation. Based on the conventional nucleation theory (Steefel and Van Cappellen, 1990), nucleation rate increased instantaneously in the solution of high Si concentration regardless of the flow rate (Eq. 20). In the precipitation experiments of this study, precipitation of silica minerals were at around

the inlet of the precipitation vessel (Fig. 2-10), where the Si concentration in the solution was higher than that at the outlet of the vessel.

3.3.1. Experimental methods

The experimental apparatus in this section was same as that of the experiments of temperature dependence in the chapter 2 (Fig. 2-1). The tube length of precipitation vessel was 51 cm. Pressure was set as 31 ± 1 MPa (Table 3-1). Temperatures for preparation of the Si supersaturated solution and precipitation were 360 °C and 430 °C, respectively. No rock substrates were placed in the precipitation vessel. The Si supersaturated solution was made by dissolution of amorphous silica at 350 °C. The flow rate and the residence time ranged 0.3–1.4 g/min and 6–26 min, respectively (Table 3-1). In each condition, the input and output solutions were sampled 3 times.

3.3.2. Results

The Si concentration in the input solutions ranged from 454 to 656 mg/kg(H_2O) (Table 3-1). The Si saturation ratio with respect to quartz, $\Omega_{Qtz} = C_{Si} - C_{Si,Qtz,eq}$, ranged from 6.2 to 9.1 (Table 3-1). The integrated value in the cases of n = 1–4 was tested following from Eq. 29 to Eq. 32 (Fig. 3-1). The largest correlation coefficient, λ, was

0.87 in the data of the first order reaction, n = 1 (Fig. 3-1a; Table 3-2), indicating that the reaction rate order in the nucleation term of Eq. 26 is first. Thus, the kinetic equation of overall silica-water reactions is given by

$$\frac{\partial C_{\mathrm{Si}}}{\partial t} = \left\{ \frac{A_{\mathrm{Qtz}}}{M} k_{\mathrm{S}} + \alpha k_{\mathrm{N}} \right\} \left(C_{\mathrm{Si,Qtz,eq}} - C_{\mathrm{Si}} \right). \tag{33}$$

Table 3-1 Conditions and results of precipitation experiments of flow rate.

Exp. Name		Vf-0.3		Vf-0.4		Vf-0.5		Vf-0.6		Vf-1.4	
Exp. Number		1		2		3		4		5	
Pressure [MPa]		31.0		30.9		30.0		30.6		30.7	
Volume of water [cm^3/g]		5.1		5.1		5.5		5.3		5.2	
Duration time [hour]											
Flow rate [g/min][1]		0.3	(0.0)	0.4	(0.0)	0.5	(0.0)	0.6	(0.0)	1.4	(0.2)
Residence time [min]		26	(1)	20	(1)	15	(0)	13	(0)	6	(1)
Concentrations [mg/kg(H_2O)]											
Si	in[2]	608	(9)	656	(5)	592	(12)	561	(20)	454	(6)
	out[2]	146	(6)	166	(11)	156	(6)	162	(4)	179	(8)
Quartz solubility		77		76		65		72		73	
Ω_{Qtz}[3]	in	7.9		8.7		9.1		7.8		6.2	
	out	1.9		2.2		2.4		2.2		2.5	

[1] Average value (standard deviation, 1σ).

[2] in = input solution, out = output solution (solution before and after passing through the precipitation vessel, respectively).

[3] Si saturation ratio with respect to quartz.

Table 3-2 Correlation coefficient of n = 1–4.

n[1]	λ[2]
1	0.87
2	0.75
3	0.66
4	0.61

[1] Precipitation rate order.

[2] The correlation coefficient.

(a) (b)

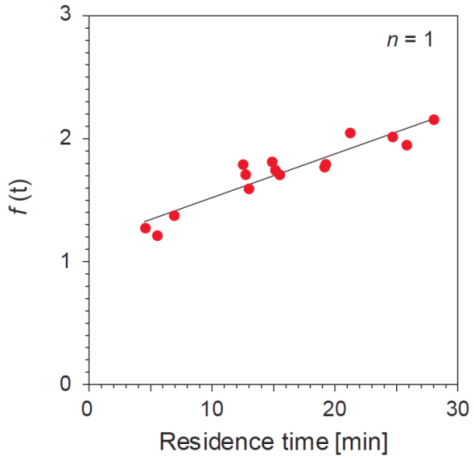

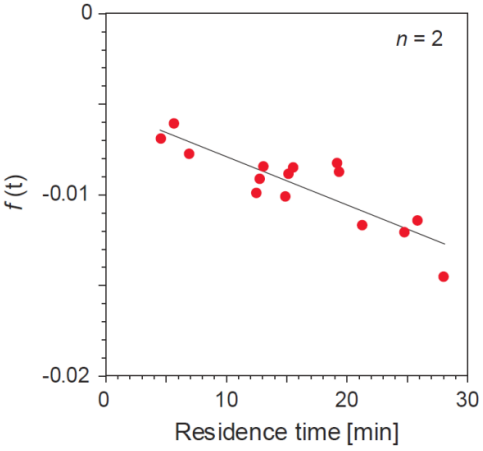

(c) (d)

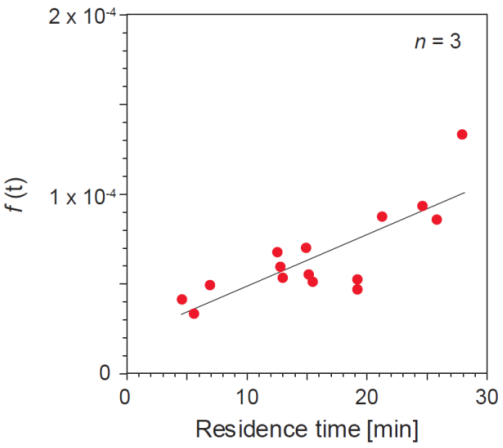

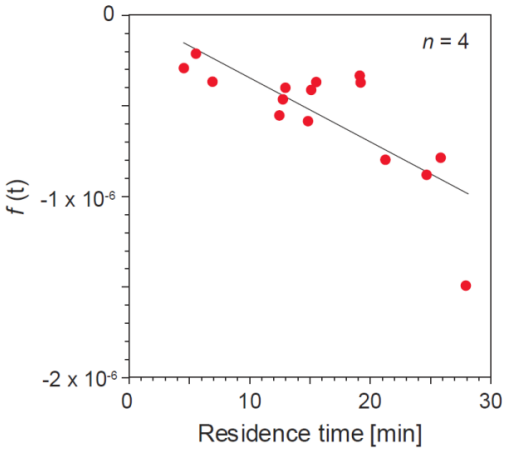

Figure 3-1 Integrated value of the reaction order, n = (a) 1, (b) 2, (c) 3, and (d) 4.

3.4. Applicable conditions of the nucleation term

In this study, the nucleation parameter, α, is introduced as an index of the possibility of precipitation via nucleation, in other words, the applicability of the second term of nucleation, having a role as same as the area of quartz surface, A_{Qtz}, in the first term of the new kinetic equation (Eq. 33). If there is no mineral including quartz surface, surface reaction does not occur and the first term does not work to estimate the reaction rate because A_{Qtz} is zero. Such a situation without pre-existing quartz could be, for example, in a formation of silica scale in the pipeline of the geothermal power plants. When nucleation of silica minerals can occur, α is 1 and the overall precipitation rate is estimated by using both first and second terms of Eq. 33. In conditions of nucleation cannot occur, α is 0 and the rate of nucleation of silica minerals in the second term of Eq. 33 does not contribute to the precipitation rate.

As a basic premise, nucleation occurs only in the Si supersaturated solution, whereas surface reaction occurs in both Si supersaturated and undersaturated solutions as precipitation and dissolution, respectively. Thus, the nucleation rate estimated by the second term of Eq. 33 is applied in the conditions of the solution supersaturated for quartz solubility, whereas the first term of surface reaction works regardless of Si concentration in the solution. The conditions to determine when nucleation occur (α = 1

or 0) is also defined based on the experimental results. The precipitation experiments in the chapter 2 revealed that the strong temperature dependence of silica precipitation relates with nucleation (Fig. 2-3). Large amount of precipitation occurred only in the supercritical conditions of water correlated with theoretical nucleation rate, whereas precipitation did not occur in liquid phase even in the solution of high Si saturation ratio with respect to quartz, Ω_{Qtz} = ~8.7 (Table 2-1, 2-2; Fig. 2-2). Therefore, in this study, the nucleation parameter, α, is zero in liquid phase:

$$\alpha = 0 \quad \text{in } C_{Si} < C_{Si,Qtz,eq}, \text{ or } T < 374\ ^{\circ}C, \text{ or } P < 22.06\ \text{MPa} \qquad (34)$$

and that is one in the supercritical conditions of water (T >374 °C and P >22.06 MPa) as follows:

$$\alpha = 1 \quad \text{in } C_{Si} > C_{Si,Qtz,eq}, \ T > 374\ ^{\circ}C, \text{ and } P > 22.06\ \text{MPa}. \qquad (35)$$

3.5. Effect of Al concentration in the solution on precipitation rate

The results of difference of Si concentrations in the input and output solutions (Fig. 2-7) and amount of precipitates (Fig. 2-9) of the precipitation experiments of minor components in the solution indicates that the precipitation rate increases with increasing of $C_{Al,in}$ from 0 to 7 mg/kg(H_2O) and decreases in the solution of $C_{Al,in}$ >10 mg/kg(H_2O). EPMA analysis revealed that precipitation of quartz, which is faster than that of amorphous silica, occurs with a couple of Al^{3+} and Na^{+} (Fig. 2-16). Thus, the increase of precipitation rate relates with mineralogy of precipitation and concentrations of minor components, Al and Na, in the solution.

The precipitation rate constant via nucleation in the precipitation experiments of minor components was calculated by using the kinetic equation as follows:

$$\frac{\partial C_{Si}}{\partial t} = k_N \left(C_{Si,Qtz,eq} - C_{Si} \right) \tag{36}$$

where A_{Qtz} = 0 m^2 in Eq. 33 because this series of the experiments were conducted without quartz surfaces. Figure 3-2 shows the logarithmic values of the precipitation rate constant, k_N, as a function of Al concentrations in the input solution. As same as the experimental results of difference of Si concentrations in the input and output solutions

(Fig. 2-7) and amount of precipitation (Fig. 2-9), there is two trend of increase of the reaction rate constant with increasing Al concentration in the solution from 0 to 7 mg/kg(H_2O) and from 12 to 29 mg/kg(H_2O). Based on the relationship between Al concentration in the input solution and mineralogy of precipitation (Fig. 2-14), the precipitation rate constant is derived in three regions as shown in Figure 3-2: precipitation of amorphous silica in the solution of $C_{Al,in}$ <1 mg/kg(H_2O), that of quartz in the solution of $C_{Al,in}$ = 1–8 mg/kg(H_2O), and precipitation of albite and analcite in the solution of $C_{Al,in}$ >8 mg/kg(H_2O). Therefore, the precipitation rate constant via nucleation of silica minerals, k_N, is given by

$$\log_{10} k_{N1} = -2.7 \quad (C_{Al,in} < 1 \text{ mg/kg}(H_2O)) \tag{37}$$

$$\log_{10} k_{N2} = -2.5 + 0.062 C_{Al,in} \quad (1 < C_{Al,in} < 8 \text{ mg/kg}(H_2O)) \tag{38}$$

$$\log_{10} k_{N3} = -2.8 + 0.012 C_{Al,in} \quad (C_{Al,in} > 8 \text{ mg/kg}(H_2O)). \tag{39}$$

The transient precipitation rate from $C_{Al,in}$ = 7 mg/kg(H_2O) to 12 mg/kg(H_2O) is not clear because the experiment with such solution was not conducted in this study.

However, silica precipitation at the shallow permeable zone in the continental plates of the Earth's crust is expected to occur mainly in the condition of the solution of C_{Al} <5 mg/kg(H_2O), which is caused by dissolution of granite as shown in the experiments of temperature dependence (Tables 2-1, 2-2). The rate constant of silica precipitation would be used in the condition of the solution of 1< $C_{Al,in}$ <8 mg/kg(H_2O) (Eq. 38) in the permeable zone of the Earth's crust.

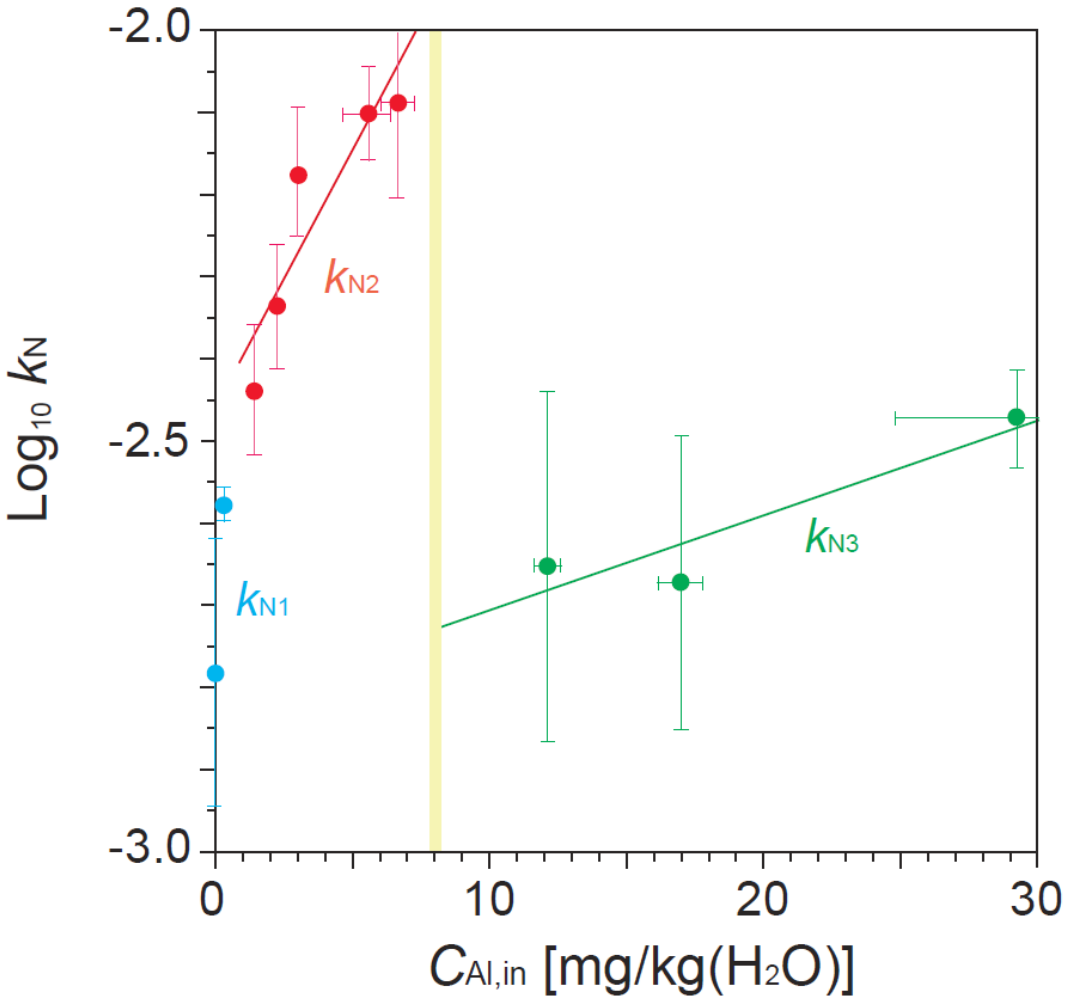

Figure 3-2 Precipitation rate constant via nucleation, k_N, in the solution of $C_{Al,in}$ <1 mg/kg(H_2O) (blue), from 1 to 8 mg/kg(H_2O) (red), and >8 mg/kg(H_2O) (green).

3.6. Application of the kinetic equation to the experimental results

The reaction rates in precipitation experiments were simulated by using the empirical kinetic equation of overall silica-water reactions (Eq. 33). Based on the initial experimental conditions of 10 experiments in Table 2-5, the Si concentrations at the outlet of the precipitation vessel, $C_{Si,out}$, were calculated. In the calculation, the surface area of quartz, A_{Qtz}, was zero because no rock/mineral substrate was used in the precipitation experiments in this study.

Table 3-3 shows the calculation and experiments results. The nucleation rate constant, k_N, increases with increasing of Al concentration in the input solutions, $C_{Al,in}$, to 6.7 mg/kg(H_2O) and decreases with increasing of $C_{Al,in}$, to 29 mg/kg(H_2O) calculated by using Eq. 37–39 (Table 2-5). The ratio of calculated versus experimental results of $C_{Si,out}$ ranges from 0.9 to 1.2, indicating that the kinetic equations (Eq. 32) can simulate precipitation rate via nucleation of silica minerals in the supercritical conditions of water.

Table 3-3 Si concentrations in the output solutions of calculated and experimental results.

$C_{Al,in}$ [mg/kg(H_2O)][1]	$Log_{10}\ k_N$[2]	$C_{Si,\ out}$ [mg/kg(H_2O)]		Calc/Exp[3]
		Calculation	Experiment	
0	-2.7	214	224	1.0
0.4	-2.7	199	181	1.1
1.4	-2.4	202	209	1.0
2.3	-2.4	167	162	1.0
3.0	-2.3	144	118	1.2
5.6	-2.2	113	104	1.1
6.7	-2.1	99	98	1.0
12	-2.7	106	109	1.0
17	-2.6	118	128	0.9
29	-2.4	91	105	0.9

[1] Al concentration in the input solutions in Table 2-6.

[2] Nucleation rate of silica precipitation determined by Eq. 36–38.

[3] The ratio of calculated versus experimental results of Si concentration in the output solutions.

3.7. Conclusions

The new kinetic equation was derived empirically to estimate the overall precipitation rate of silica minerals, including surface reaction of quartz and nucleation of silica polymorphs in the crustal conditions. The first term indicating the rate of surface reaction is same as the previous kinetic equation of Rimstidt and Barnes (1980), and the second term is introduced to represent precipitation via nucleation. The three parameters of the reaction order of nucleation, n, the nucleation parameter, α, and nucleation rate constant, k_N, in the second term were derived based on the hydrothermal experiments of silica precipitation.

Reaction rate order, n, is 1 derived by using the integral methods based on the precipitation experiments with different flow rates (and residence times). The nucleation parameter, α, is one in the conditions of Si supersaturated solution and in the supercritical conditions of water, whereas it is zero in other conditions. The reaction rate constant, k_N, is expressed as a function of Al concentration in the solution, based on mineralogical change of precipitates. The Si concentrations in the output solutions in the experiments of minor components were well reproduced by using the new kinetic equation of overall silica-water reactions.

4. SILICA PRECIPITATION AT THE PERMEABLE-IMPERMEABLE BOUNDARY

4.1. Introduction

Permeability is an important hydrological parameter that influences various geological processes including ore formation, crustal deformation, seismicity, and the development of geothermal systems. Permeability is also a dynamic parameter in response to active deformation, fluid pressure, dissolution and precipitation of minerals. In general, permeability decreases sharply with increasing depth at shallower levels in the crust but is nearly constant at deeper levels (typically >10–20 km depth) (Ingebritsen and Manning, 2002, 2010; Fig. 1-5). This trend with depth has been thought to correspond broadly to that of the brittle–plastic transition (BPT) (Ingebritsen and Manning, 2010; Weis *et al*., 2012) at around 300–450 °C for quartzo-feldspathic rocks (Scholz, 2002). Precipitation of silica from aqueous fluids could be one of the critical processes to affect the spatial and temporal variations in permeability within the crust (Lowell *et al*., 1993; Connolly, 1997; Fournier, 1999; Rusk and Reed, 2002). Quartz deposition and creep would be important in the self-sealed zone at the BPT (Fournier, 1999). Apart from some observations from deep wells in geothermal areas

(Fournier, 1991; White and Mroczek, 1998), however, there is little information on the locations of silica dissolution and precipitation within the crust.

In this chapter, silica–water interaction under the conditions was investigated at the Kakkonda geothermal field, Japan, which has a well that penetrates the boundary between the hydrothermal convection zone and the underlying heat conduction zone (Doi *et al.*, 1998). Based on calculations of quartz solubility down the well, and the results of the hydrothermal experiments, the influence of silica precipitation on the formation of the permeable-impermeable boundary in the crust was examined.

4.2. The Kakkonda geothermal field

4.2.1.1. Geology

The Kakkonda geothermal field, with a surface area of approximately 4 × 2 km, lies within the Hachimantai volcanic zone in NE Japan and is one of the most extensive liquid-dominated geothermal fields nationwide (Fig. 4-1a). The rocks of the field consist of the Kakkonda granite, the Tamagawa welded tuffs, Miocene volcaniclastic and sedimentary rocks, pre-Tertiary formations, and older intrusive rocks (Doi *et al.*, 1998; Fig. 4-1b). Kakkonda granite of late stage (non-metamorphic zone) had been

found in the well-13, 19, 20, 21, and 22 (Doi *et al*., 1998; Fig. 4-1b), and it recognized as the heat source of the hydrothermal system (Kato *et al*., 1993).

4.2.1.2. Ages

Zonal arrangements of alteration ages were estimated from less than 0.1 Ma to 0.3 Ma by thermo-luminescence measurements of quartz at the Kakkonda-Omatsukurazawa and adjacent areas (Takashima *et al*., 1987). The K-Ar ages of K-feldspars in the hydrothermal veins at the Kakkonda and adjacent areas are 0.2 ± 0.1 Ma (Koshiya *et al*., 1993), which has been regarded as the age of vein formation at least after 0.2 Ma in the studied area to the present. Kanisawa *et al*. (1994) revealed that the K-Ar ages of mica, K-feldspars, and hornblende of the Kakkonda granite range from 0.068 to 0.34 Ma, which may indicate the ages subsequent passing the closure temperature of each mineral. They suggested that the observed intrusive age of pluton might have been older than the obtained data because of high temperatures, and might be slightly younger than 0.7–1.0 Ma, from the relation between the ages of the adjacent Tamagawa Welded Tuffs. A numerical simulation of the history of the Kakkonda geothermal system suggested that it has developed during 0.4–0.6 Ma after the time of intrusion and is in the most active stage at present (Ehara *et al*., 2001). K-Ar ages of separated minerals from the granitic

rocks was observed as 0.24–0.11 Ma for hornblende, 0.21–0.02 Ma for biotite, and 0.14–0.01 Ma for potassium feldspar, which are the youngest ages for granite in the world (Doi *et al*., 1998).

4.2.1.3. Conditions observed at the well WD-1a

In 1995, the well WD-1a was drilled into the Kakkonda field to reveal the deep geothermal structure. Measured temperature in WD-1a exceeded the hydrostatic boiling-point curve with a maximum of >500 °C at a depth of 3729 m (Doi *et al*., 1998; Ikeuchi *et al*., 1998; Figs. 4-1b, 4-10a). The temperature gradient in the deeper parts of WD-1a (>3100 m depth) is about ten times greater than that in the shallower parts (<3100 m depth) (Fig. 4-10a). Thus, a depth of 3100 m (380 °C and 24 MPa) within the Kakkonda granite marks the boundary between the hydrothermal convection zone and the heat conduction zone (Figs. 4-1b, 4-10a).

Two geothermal reservoirs are recognized in well WD-1a at shallow (230–260 °C) and deep (300–350 °C) levels (Doi *et al*., 1998; Ikeuchi *et al*., 1998; Fig. 4-1b), where the vertical permeability values are approximately 10^{-14} and 10^{-16} m^2, respectively (Hanano and Takanohashi, 1993). The core samples recovered from around the base of the hydrothermal convection zone have permeability values of 8.9×10^{-17} m^2 at 2937 m

depth and 5.9 × 10^{-17} m^2 at 3229 m depth (measurements at room temperature; Fujimoto *et al*., 2000). The lost circulation occurred into three parts of WD-1a: at very shallow part from 42 to 281 m depth, in a typical shallow reservoir from 981 to 1589 m depth, and in a quasi-deeper reservoir from 1900 to 2137 m depth (Muraoka *et al*., 1998). The logs of formation micro-imager (FMI) revealed that fractures and closed fractures with high dips were relatively dominant at depths from the surface to 1770 m, whereas high concentrations of fractures and closed fractures with low angles exist from 1770 to 2860 m depth (Muraoka *et al*., 1998).

Earthquake hypocentres are distributed mostly at depths shallower than the top of the Kakkonda granite (Tosha *et al*., 1998). Matsushima *et al.* (2003) identified strong reflectors in prestack time-migrated multi-channel seismic data at or near the 350 °C isotherm. Based on the δD-δ^{18}O isotopic properties, the geothermal fluids of low salinity (≤1.2 wt% NaCl equivalent for fluids in the shallow reservoir; Muramatsu *et al*., 2000) were interpreted to result from the dilution of hypersaline fluids produced by exsolution from a residual magma (~55 wt% NaCl equivalent) with heated meteoric water, and by boiling of the dilute fluids (Kasai *et al*., 1998).

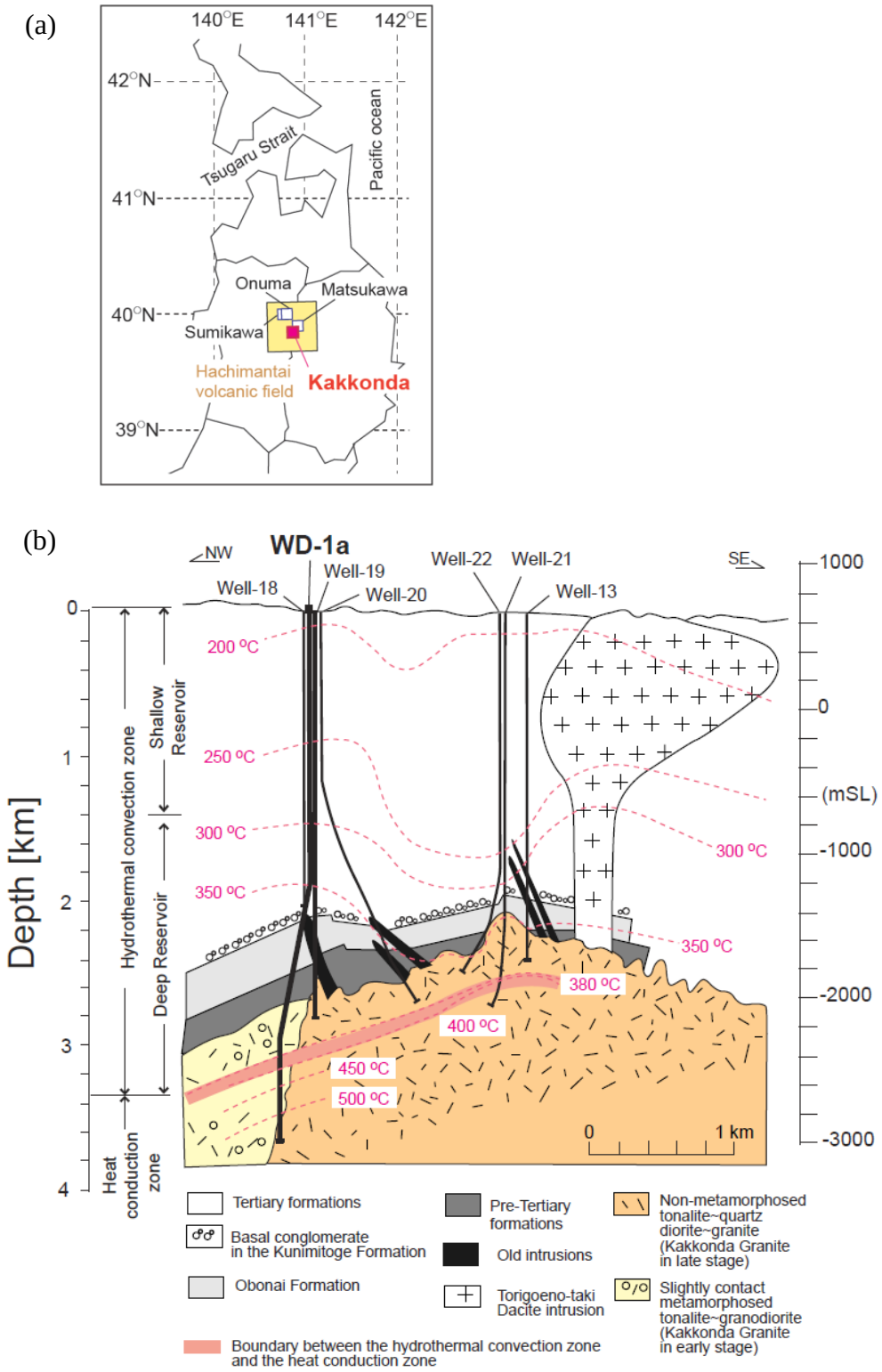

Figure 4-1 The Kakkonda geothermal field. (a) Location of the Kakkonda geothermal field in the Hachimantai volcanic field, NE Japan. (b) Schematic cross-section through the Kakkonda geothermal system (modified after Doi *et al.*, 1998).

4.3. Compositions of silica deposits in the Kakkonda geothermal field

Compositions of silica scale formed in the pipeline of the Kakkonda geothermal plant and that of the drilling core samples at the well WD-1a of the Kakkonda geothermal field were analysed. These samples were provided by Tohoku Hydropower and Geothermal Energy Co., Inc. (TOHGEC), Iwate, Japan. Compositions of silica scale and core samples were analyzed by EPMA in Tokyo University and University of Oregon.

4.3.1. Silica scale

Silica scale was sampled on April 2008 in the D-B line, which is one of the pipelines between the production well and the Kakkonda geothermal plant. Duration of silica scale formation was about several years. The current conditions of the D-B line were at 140 °C and 0.25MPa. Flow rate was 500 t/h. The inlet diameter of the pipeline was 589 mm.

The sample of silica scale sample has a porous structure. The wave pattern of top surface of the sample reflects the direction of fluid flow in the pipeline (Fig. 4-2). The XRD analysis revealed that the sample of silica scale consists of amorphous silica with minor amount of quartz (Fig. 4-3). No other crystalline minerals are found. SEM-CL

observation revealed that the sample of silica scale consists of the fine-grained aggregate and the massive part with several fractures (Fig. 4-4a). The massive part consists of amorphous silica without crystalline minerals (Fig. 4-4a). EPMA mapping of the fine-grained aggregate shows various domains with different composition of amorphous silica (Fig. 4-4b). Si-rich domain is poor in Al content. The amount of Ca rich domain is small. K and Al contents are positively correlated (Fig. 4-4b), and may indicate that the Al^{3+} precipitate with K^{+} in silica scale. The quantitative analysis of EPMA was conducted at the fine-grain aggregate and massive part (L1 and L2 in Fig. 4-5). In the fine-grained aggregate, the concentration of Al_2O_3 ranges from 4 to 32 wt% (Table 4-1). The average value of Al_2O_3 is 19 wt%, which is a next largest component of SiO_2 (Table 4-1; Fig. 4-6a). Distribution of K_2O correlates with that of Al_2O_3, especially at 40, 70, 160, 270, 340, and 480–530 μm from the start point (Table 4-1; Fig. 4-6a). At the start point, the concentration of CaO has the highest value of 27 wt%, which correlates with that of TiO_2 (34 wt%; Table 4-1; Fig. 4-6a). The local maximum value of MgO concentration correlates with the concentrations of MnO at 140, 160, and 200 μm from the start point (Fig. 4-6b). In the massive part, the concentrations of components except SiO_2 are lower than that of Line 1. Al_2O_3 is a next largest component of SiO_2, ranging from 4 to 12 wt% as same as the results of L1 (Table 4-1, 4-2). In this part, the

concentration of CaO correlates with that of Al_2O_3 at 180 μm from the start point (Fig. 4-7a). The distributions of Na_2O and K_2O show no correlation with Al_2O_3 and CaO (Fig. 4-7a). The concentrations of MgO, TiO_2, MnO, and FeO also have the largest values at 180 μm from the start point (Fig. 4-7b).

The EPMA analysis in the experimental products of this study suggested that Al^{3+} with Na^+ substitutes to Si^{4+} in quartz (Fig. 2-16, 17, and 18). The average values of the Al concentration in the silica scale sample of the Kakkonda geothermal plant are 1.1×10^5 and 4.2×10^4 mg/kg in L1 and L2, respectively, which are higher than that of quartz in the experiments (Fig. 2-16). However, the correlation of concentration between Al_2O_3 and K_2O in the fine-grained aggregate of the scale sample (Fig. 4-6a) might indicate that small amount of quartz precipitated in the silica scale due to the couple of Al^{3+} and K^+ instead of Na^+. In the massive part of the scale sample, the concentrations of Na_2O and K_2O did not show the specific correlation with that of Al_2O_3 (Fig. 4-7a) probably because there is no quartz, which is also shown in the SEM-CL images (Fig. 4-5).

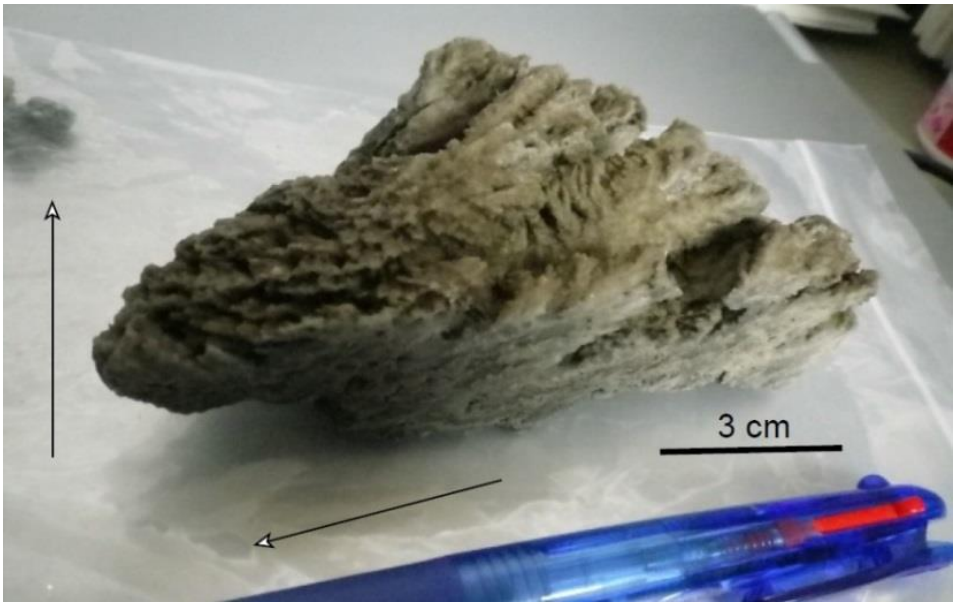

Figure 4-2 A photo of silica scale sampled at the D-B line of the Kakkonda geothermal plant.

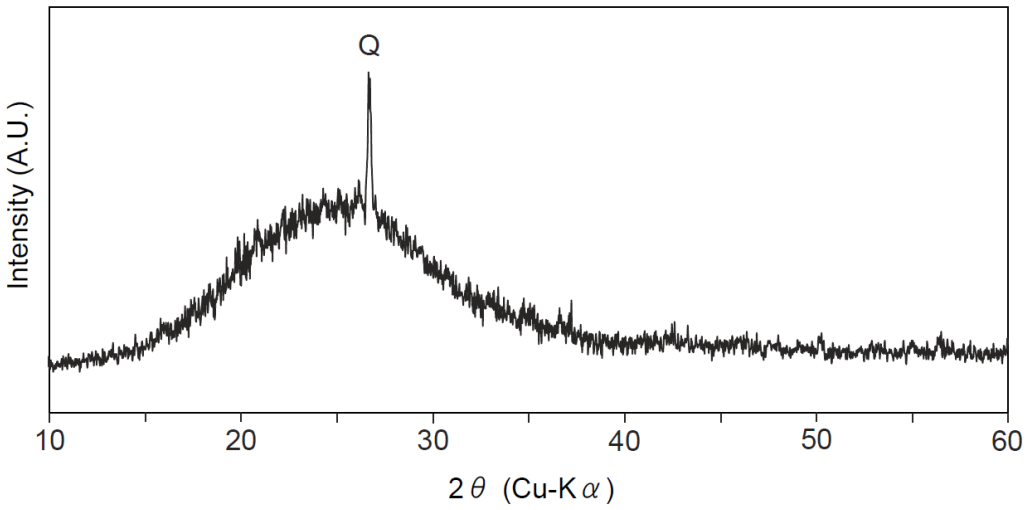

Figure 4-3 XRD plot of silica scale sample of the Kakkonda geothermal plant. The peak of quartz (Q) is at 26.64° ((1 0 1) diffraction).

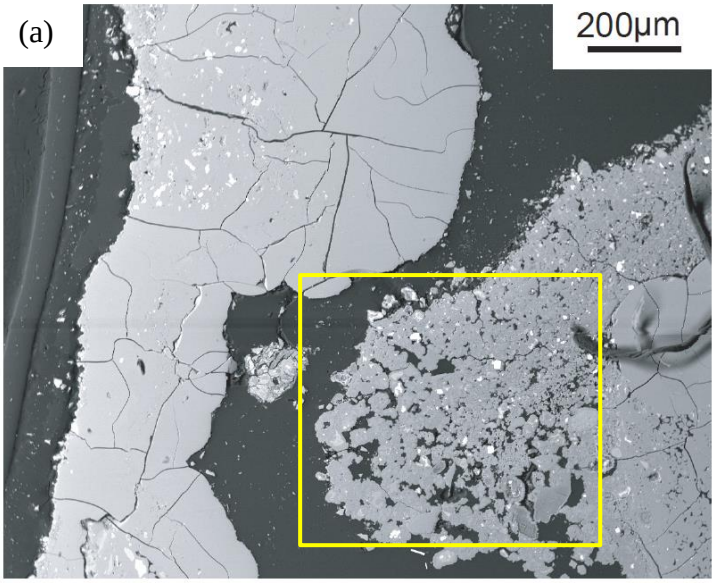

(b)

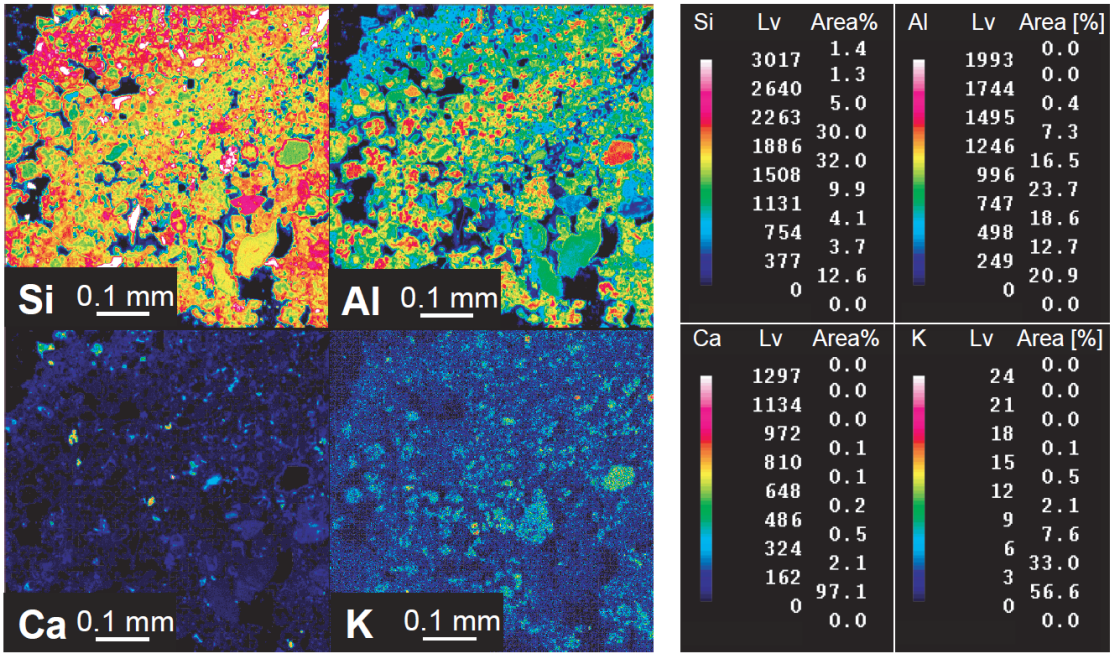

Figure 4-4 Images of the silica scale of the Kakkonda geothermal plant. (a) SEM-CL image, and (b) EPMA mapping images at the area of the yellow box in Fig. 4-4a. Concentrations of components in the silica scale (Si, Al, Ca, and K) are shown in color map.

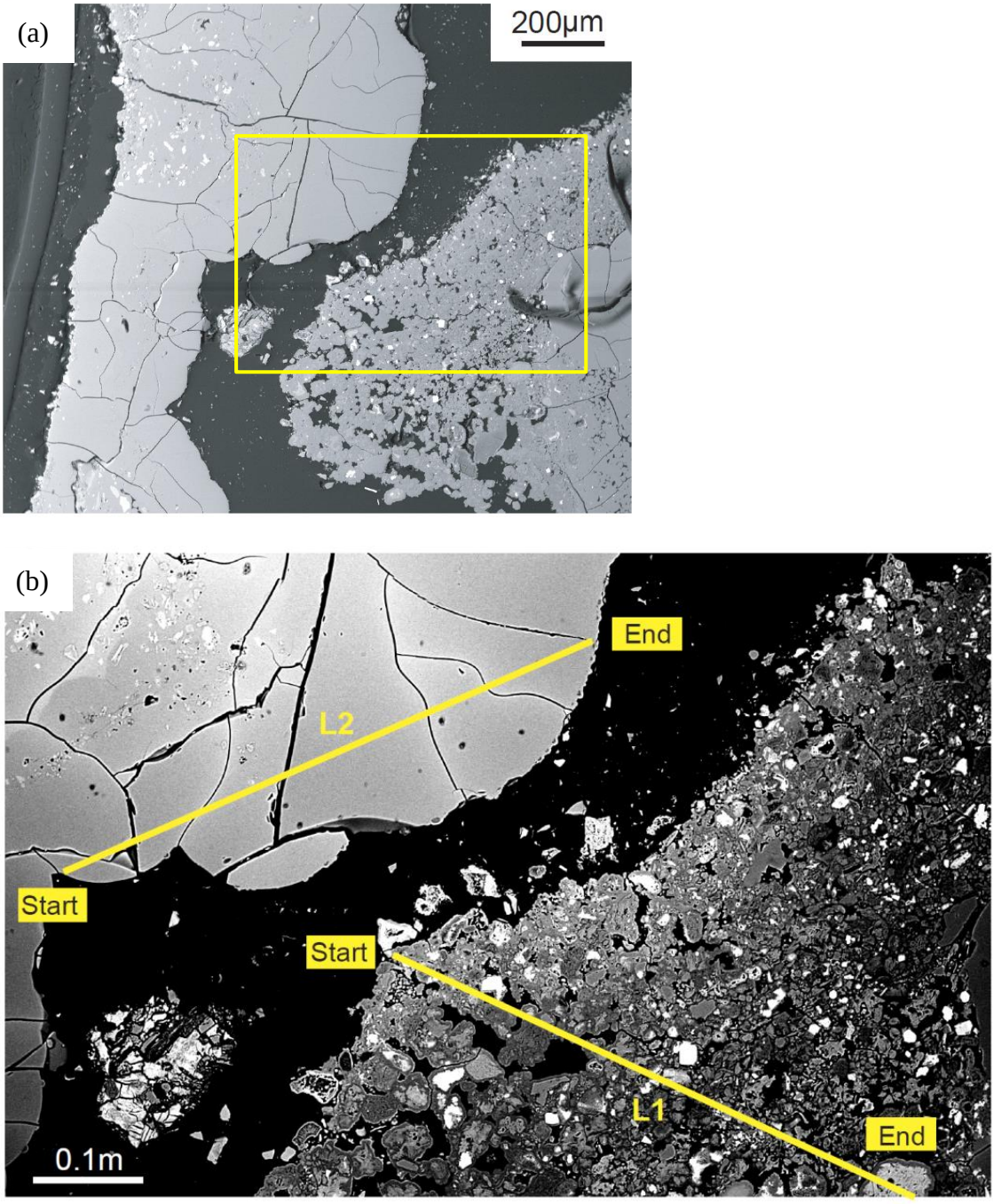

Figure 4-5 Images of the silica scale of the Kakkonda geothermal plant. (a) SEM-CL image, and (b) EPMA line analysis in the area of the yellow box in Fig. 4-5a. The scanning lines of EPMA run from start to end points. Concentrations of elements along the line of L1 and L2 are shown in Fig. 4-6 and 4-7, respectively.

Table 4-1 Results of EPMA analysis along the line L1 (wt%; Fig. 4-5b).

Distance [μm]	0	10	20	30	40	50	60	70	80	90	100	110	120	130
Al_2O_3	4	19	25	10	18	14	12	28	13	19	11	13		22
Na_2O	0.0	0.4	0.3	0.6	0.8	0.5	0.7	0.3	0.6	0.5	0.5	0.4		0.3
K_2O	0.2	3.8	1.0	1.0	3.0	0.9	1.7	3.7	0.8	1.0	1.1	1.0		0.9
MnO	0.0	0.0	0.1	0.1	0.1	0.0	0.1	0.0	0.0	0.0	0.0	0.1		0.1
TiO_2	34	11	0.1	0.0	0.1	0.6	0.0	0.0	0.0	0.1	0.0	0.0		0.0
SiO_2	31	52	49	58	64	50	62	59	66	62	76	76		62
MgO	0.0	0.4	4.1	0.2	0.6	0.9	0.3	1.1	0.1	0.4	0.1	0.2		0.7
CaO	27	9.4	1.3	3.0	1.2	3.4	1.3	0.4	1.2	0.8	0.8	0.9		0.9
FeO	0.2	0.8	3.8	6.2	0.9	14.0	0.4	0.4	0.2	0.6	0.2	0.2		0.3
Cr_2O_3	0.0	0.0	0.0	0.0	0.0	0.0	0.0	0.0	0.0	0.0	0.0	0.0		0.0
Total	97	97	85	79	89	85	79	93	82	84	90	92		87

Distance [μm]	140	150	160	170	180	190	200	210	220	230	240	250	260	270
Al_2O_3	32	16	24	18	13	23	27	27		21	22	22	21	32
Na_2O	0.2	0.4	0.2	0.5	0.5	0.4	0.2	0.4		0.4	0.3	0.5	0.7	0.3
K_2O	0.7	0.7	2.3	0.8	0.7	0.5	1.5	2.3		1.0	1.8	1.0	1.4	6.1
MnO	0.4	0.1	0.6	0.0	0.0	0.1	0.7	0.0		0.1	0.1	0.1	0.0	0.0
TiO_2	0.0	0.0	0.1	0.0	0.0	0.0	0.0	0.1		0.0	0.0	0.0	0.0	0.1
SiO_2	49	71	55	72	62	65	46	62		65	61	58	58	50
MgO	3.2	0.1	4.8	0.1	0.1	0.2	11	0.5		0.2	0.4	0.2	0.1	1.0
CaO	0.3	0.9	0.4	1.0	1.1	0.9	0.3	0.6		0.8	0.8	0.9	0.8	0.1
FeO	1.4	0.0	2.8	0.2	0.5	0.3	1.5	0.1		0.1	0.1	0.2	0.0	1.0
Cr_2O_3	0.0	0.0	0.0	0.0	0.0	0.0	0.0	0.0		0.0	0.0	0.0	0.0	0.1
Total	87	90	90	92	78	91	89	93		89	87	83	81	91

Distance [μm]	280	290	300	310	320	330	340	350	360	370	380	390	400	410
Al_2O_3	19	27	21		14	24	32	16	10	20	20	19		19
Na_2O	0.5	0.4	0.7		0.5	0.4	0.2	0.8	0.5	0.5	0.4	0.3		0.2
K_2O	0.9	1.3	1.2		0.7	0.7	6.8	1.4	1.1	0.9	1.0	0.8		3.3
MnO	0.0	0.0	0.1		0.2	0.1	0.1	0.0	0.0	0.0	0.1	0.0		0.1
TiO_2	0.0	0.0	0.0		0.4	0.2	0.1	0.0	0.0	0.0	0.0	0.0		0.1
SiO_2	50	58	66		54	48	54	51	82	56	60	61		71
MgO	0.1	0.3	0.1		0.1	1.9	1.7	0.1	0.3	0.1	0.3	0.3		2.1
CaO	0.9	0.5	1.1		5.0	1.4	0.1	1.0	0.8	0.9	2.8	3.1		0.5
FeO	0.2	0.1	0.1		2.9	7.1	0.8	0.1	0.1	0.2	0.4	0.4		0.5
Cr_2O_3	0.0	0.0	0.0		0.0	0.0	0.0	0.0	0.0	0.1	0.0	0.0		0.0
Total	71	88	90		78	84	96	70	94	79	84	85		97

Table 4-1 continued.

Distance [μm]	420	430	440	450	460	470	480	490	500	510	520	530
Al_2O_3		21		15	31		9	33	34	33	34	10
Na_2O		0.5		0.8	0.2		0.7	0.2	0.4	0.2	0.3	0.4
K_2O		4.7		2.4	4.7		1.6	8.2	8.4	8.2	7.5	2.3
MnO		0.0		0.0	0.1		0.0	0.0	0.0	0.1	0.1	0.0
TiO_2		0.1		0.0	0.0		0.0	0.1	0.1	0.1	0.1	0.0
SiO_2		62		55	54		61	49	50	50	50	55
MgO		0.9		0.3	0.6		0.0	1.2	0.5	0.6	0.6	0.1
CaO		1.1		0.9	0.3		2.5	0.1	0.1	0.2	0.1	1.8
FeO		0.4		0.7	0.1		0.1	1.3	0.9	1.2	1.0	0.2
Cr_2O_3		0.0		0.1	0.1		0.0	0.0	0.0	0.0	0.0	0.0
Total		91		75	91		75	93	95	93	94	70

Table 4-2 Results of EPMA analysis along the line L2 (wt%; Fig. 4-5b).

Distance [μm]	0	20	40	60	80	100	120	140	160	180	200	220	240	260
Al_2O_3	6.1	7.1	7.7	9.5	6.5	5.2		5.3	4.4	8.9	6.6	11.6	11.4	11.2
Na_2O	0.7	0.6	0.7	0.7	0.8	0.6		0.7	0.5	0.6	0.6	1.0	0.9	0.9
K_2O	1.4	1.4	1.5	1.7	1.5	1.5		1.6	1.5	1.3	1.5	1.3	1.3	1.4
MnO	0.0	0.0	0.0	0.0	0.1	0.0		0.0	0.0	0.2	0.0	0.0	0.0	0.0
TiO_2	0.0	0.0	0.0	0.0	0.0	0.0		0.0	0.0	0.4	0.0	0.0	0.0	0.0
SiO_2	63	63	72	62	70	69		62	63	52	64	77	75	76
MgO	0.0	0.0	0.0	0.0	0.0	0.0		0.0	0.0	0.1	0.0	0.0	0.0	0.0
CaO	2.3	2.3	2.4	2.4	2.0	2.2		2.4	2.2	5.2	2.3	2.5	2.8	2.8
FeO	0.0	0.0	0.0	0.0	0.0	0.0		0.1	0.0	2.6	0.0	0.0	0.0	0.0
Cr_2O_3	0.0	0.0	0.0	0.0	0.0	0.0		0.0	0.0	0.0	0.1	0.0	0.0	0.0
Total	74	74	84	76	81	79		72	72	72	76	94	92	92

Distance [μm]	280	300	320	340	360	380	400	420	440	460	480	500	520
Al_2O_3	11	11	10	8	11	6	5	10	4	5		4	8
Na_2O	0.8	0.7	0.8	0.8	1.2	0.7	0.7	0.5	0.7	0.6		0.5	0.4
K_2O	1.3	1.3	1.3	1.3	1.6	1.7	1.6	1.4	1.6	1.7		1.6	1.5
MnO	0.0	0.1	0.0	0.0	0.0	0.0	0.1	0.1	0.0	0.1		0.0	0.0
TiO_2	0.1	0.0	0.0	0.0	0.0	0.0	0.0	0.0	0.0	0.0		0.1	0.0
SiO_2	76	76	79	77	77	65	52	59	56	60		54	61
MgO	0.0	0.0	0.0	0.0	0.0	0.0	0.0	0.0	0.0	0.0		0.0	0.0
CaO	2.7	2.7	2.3	2.4	2.5	2.4	2.5	2.6	2.3	2.3		2.3	2.3
FeO	0.0	0.0	0.1	0.1	0.0	0.0	0.0	0.0	0.0	0.0		0.0	0.0
Cr_2O_3	0.0	0.0	0.0	0.0	0.0	0.0	0.0	0.0	0.0	0.0		0.0	0.0
Total	92	91	94	90	94	76	62	74	65	69		63	74

(a)

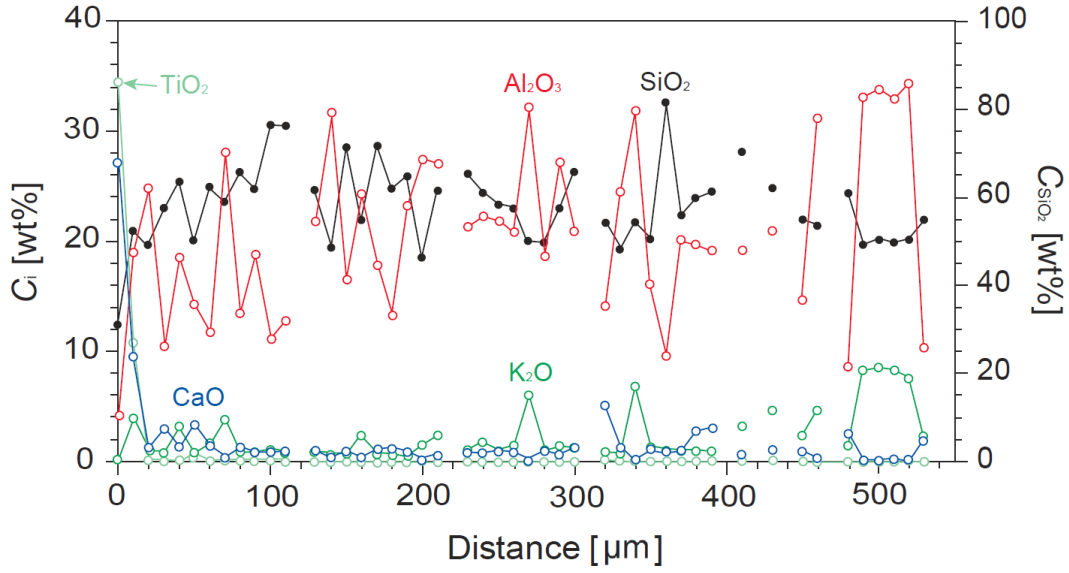

(b)

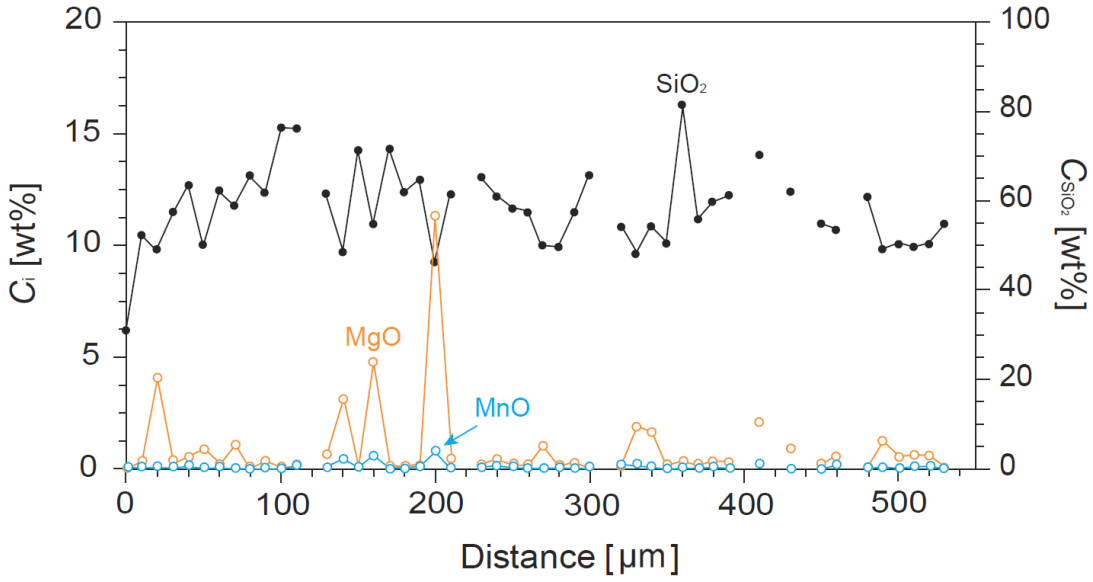

Figure 4-6 EPMA results of the concentrations of elements along the line L1 in Fig. 4-5b. (a) Al_2O_3 (red), K_2O (green), and CaO (blue). (b) MgO (yellow) and MnO (right blue). Black plots show SiO_2.

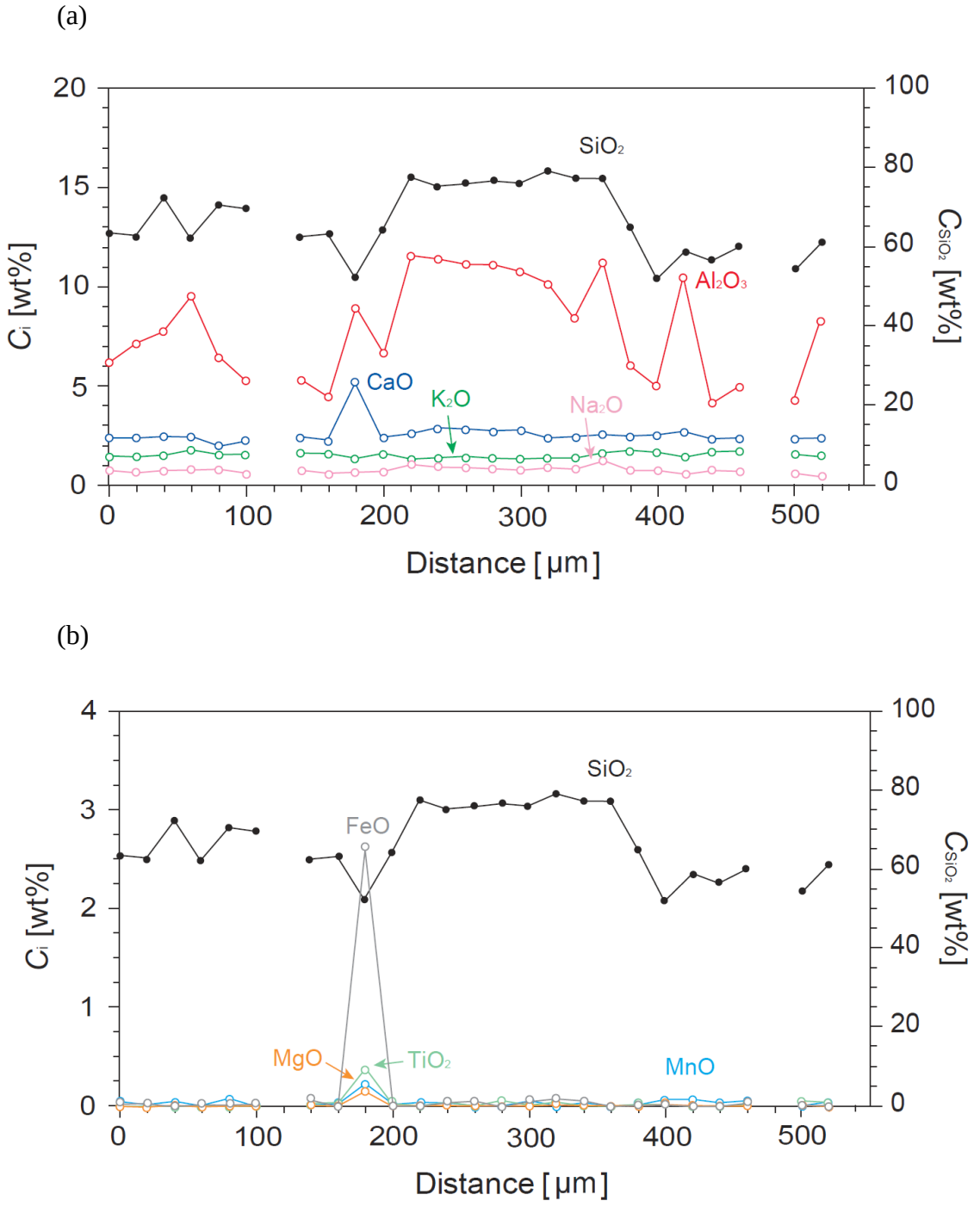

Figure 4-7 EPMA results of the concentrations of elements along the line L2 in Fig. 4-5b. (a) Na_2O (pink), Al_2O_3 (red), K_2O (green), and CaO (blue). (b) MgO (yellow), TiO_2 (right green), MnO (right blue), and FeO (grey). Black plots show SiO_2.

4.3.2. Core samples with the hydrothermal veins

The core samples were from the well KT-208(KT-208a) at the depth of 822, 1258, 1486, and 2086 m of the Kakkonda geothermal field. Temperature ranged 200–300 °C at the depth of sampling. The compositions of quartz in the vein of these samples were analyzed by using EPMA of University of Oregon. Minerals in veins were identified by analysis of Energy Dispersive X-ray Spectrometry (EDS) in University of Oregon. Figure 4-8 shows the Back Scatter Electron (BSE) images of the veins in the core samples of Kakkonda geothermal field. At the point where the concentration of elements is under the detection limit, the EPMA result shows the negative value, which can be considered as zero. The zoning was observed in SEM-CL image of the core sample at 1257 m depth (Fig. 4-8b, 4-9).

In the quartz and wairakite vein at 822 m depth (Fig. 4-8a), the concentration of Al_2O_3 ranges from 6.5×10^{-3} to 22×10^{-3} wt% (Table 4-3a). At the measured point of No. 6, high concentration of Al_2O_3 correlates with that of CaO (12 wt%; Table 4-3a). At the bright zones in the SEM-CL image of quartz in CaAl silicate vein at 1258 m depth (Fig. 4-9), Al_2O_3 concentration ranges from 5.1×10^{-3} to 49×10^{-3} wt% (Table 4-3b). The largest concentration of TiO_2 correlates with that of Al_2O_3 and K_2O, which shows no correlation with that of FeO and CaO (Table 4-3b). Na_2O was not detected in quartz

of the sample at 822 and 1257 m depth (Table 4-3a, b). In the sample of the quartz vein at 1485 m depth (Fig. 4-8c), the concentration of Al_2O_3 is up to 508×10^{-3} wt%, which is almost several ten times higher than that in quartz in the vein at other depth (Table 4-1c). In the anhydrite vein at 2086 m depth (Fig. 4-8d), the concentration of Al_2O_3 in quartz ranges from 13×10^{-3} to 25×10^{-3} wt% (Table 4-3d), which is similar to that of the quartz and wairakite vein at 822 m depth (Fig. 4-8a). The concentration of CaO is higher than that at other depth, ranging from 18×10^{-3} to 63×10^{-3} wt% (Table 4-3d). The correlation of distribution of Al_2O_3 with other elements is not clear in the sample at 1485 m and 2086 m depth (Table 4-1c, d).

(a) 822 m depth

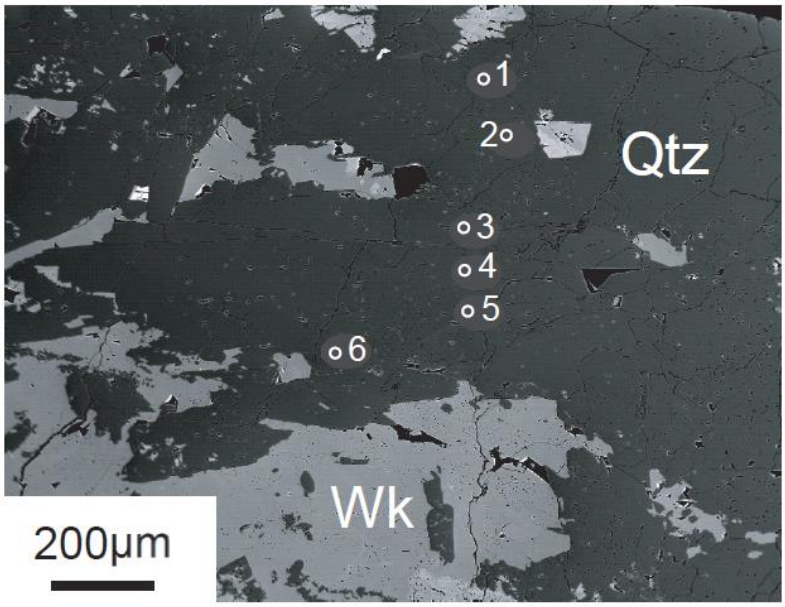

(b) 1258 m depth

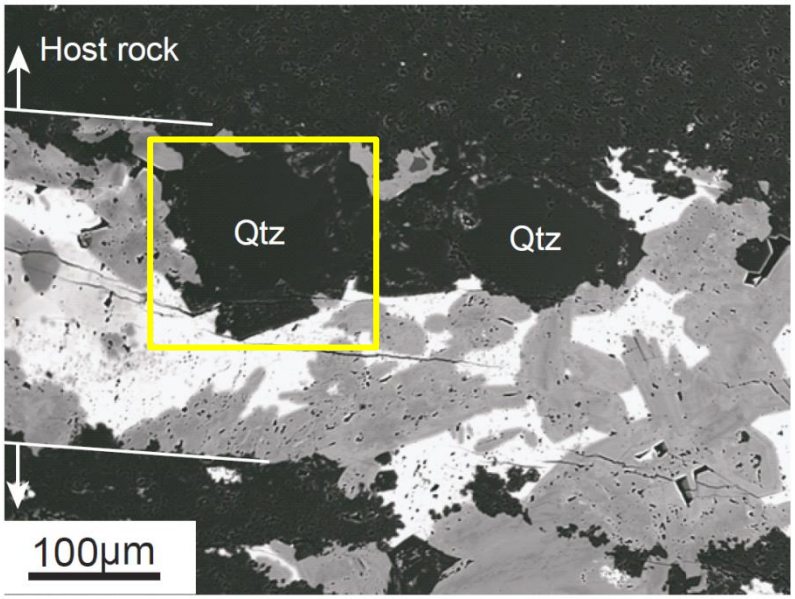

Figure 4-8

(c) 1486 m depth

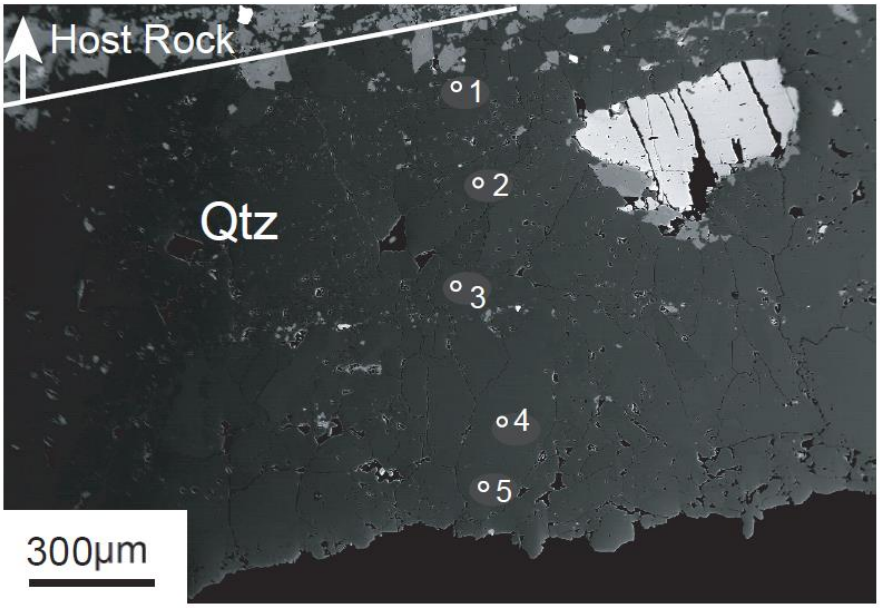

(d) 2086 m depth

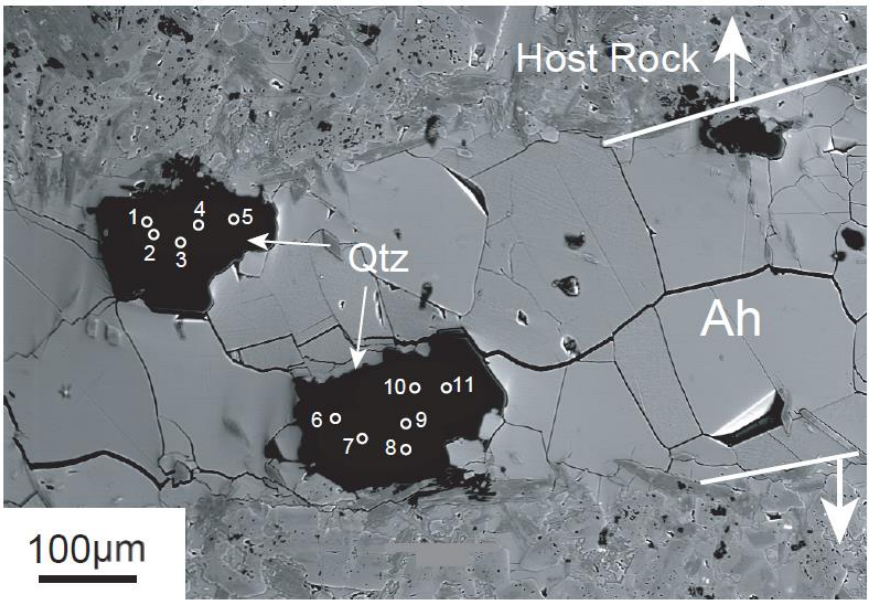

Figure 4-8 Back Scatter Electron (BSE) images of the veins of Kakkonda geothermal field. (a) Quartz (Qtz) and wairakite (Wk) vein at 822 m depth, (b) quartz (Qtz) in CaAl silicate vein at 1258 m depth, (c) quartz vein at 1486 m depth, and (d) quartz (Qtz) in anhydrite (Ah) vein at 2086 m depth. Numbers are analysis points by EPMA in Table 4-3.

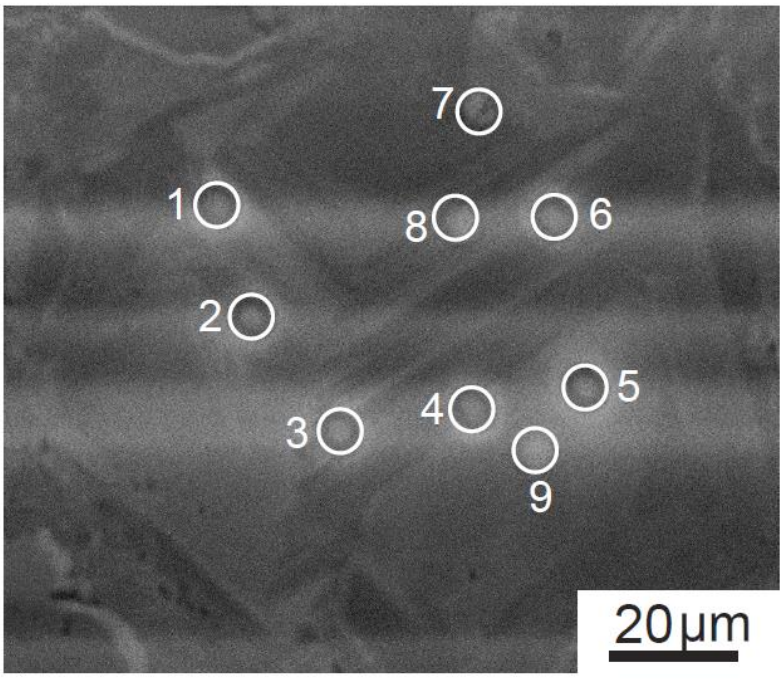

Figure 4-9 SEM-CL image of quartz at the area of the yellow box in Fig. 4-8b in the core sample at 1257 m depth of the Kakkonda geothermal field. Numbers are analysis points by EPMA in Table 4-3b.

Table 4-3 Concentrations of elements (10^{-3} wt%) in core samples of the Kakkonda geothermal field at (a) 822 m, (b) 1257 m, (c) 1485 m, and (d) 2086 m depth.

(a) 822 m depth

No.	1	2	3	4	5	6
Na_2O	-4.6	-2.6	-3.3	-5.1	-5.5	-2.4
Al_2O_3	6.5	20	17	22	10	22
FeO	-0.5	1.1	4.1	2.2	2.6	3.5
CaO	-2.8	1.4	4.7	7.8	4.4	12
K_2O	1.4	2.2	2.0	2.0	2.3	1.8

(b) 1257 m depth

No.	1	2	3	4	5	6	7	8	9
TiO_2	-3.9	-5.7	-4.8	-1.1	-4.7	-2.7	4.7	2.7	2.6
Al_2O_3	13	22	32	19	10	28	49	33	5.1
FeO	27	25	23	17	20	14	16	15	19
CaO	14	12	18	8	8	10	5.6	10	8.6
K_2O	2.1	2.0	3.5	1.9	2.8	1.2	5.7	0.4	-0.9

(c) 1485 m depth

No.	1	2	3	4	5
Na_2O	5.3	-0.9	0.4	3.7	-0.9
Al_2O_3	343	10	382	508	413
FeO	59	2.8	2.0	2.0	0.1
CaO	4.7	-3.3	2.5	1.4	4.5
K_2O	47	0.5	3.6	0.3	2.5

(d) 2086 m depth

No.	1	2	3	4	5	6	7	8	9	10	11
Na_2O	-3.5	-3.5	-0.8	-2.7	-6.3	-6.5	-3.3	-3.2	-5.1	-4.8	-3.3
Al_2O_3	17	23	13	17	25	16	17	20	25	18	19
FeO	24	24	16	22	25	23	27	36	25	17	19
CaO	30	37	18	25	56	63	26	28	26	41	32
K_2O	2.0	4.1	1.2	2.6	4.2	4.9	4.3	2.3	4.8	2.5	5.7

4.4. Quartz solubility along the WD-1a

The solubility of quartz with respect to water, $C_{Si,Qtz,eq}$ mg/kg(H_2O), was calculated for the *PT* conditions within the well WD-1a (Ikeuchi *et al*., 1998; Table 4-4; Fig. 4-10a), using the recent thermodynamic data (Manning, 1994; Akinfiev and Diamond, 2009). The fluid pressure was assumed to be hydrostatic (Table 4-2), based on reservoir pressure data (Hanano and Takanohashi, 1993), and assumed the fluid to be pure H_2O (Muramatsu *et al*., 2000). The effects on quartz solubility of salinity and of the increase of fluid pressure above hydrostatic at deeper levels were also evaluated.

Under the geothermal gradient of the Kakkonda geothermal field, quartz solubility in pure water under hydrostatic conditions increases with increasing depth to $C_{Si,Qtz,eq}$ = 345 mg/kg(H_2O) at 2350 m depth (350 °C, 18.5 MPa), decreases drastically to 195 mg/kg(H_2O) at 3100 m depth (380 °C, 24 MPa), and further to 33 mg/kg(H_2O) at 3350 m depth (450 °C, 26 MPa) (Fig. 4-10b). At deeper levels, quartz solubility increases to 55 mg/kg(H_2O) at the bottom of WD-1a, 3790 m depth (590 °C, 29 MPa) (Fig. 4-10b).

Saline fluids with 10 wt% NaCl equivalent show a higher quartz solubility than does pure water, especially at T >300 °C, and the depth of the local minimum quartz solubility becomes greater compared with pure water (Table 4-4; Fig. 4-11b). However, the trend of the quartz solubility-depth curve does not change significantly in solution

with salinity <10 wt% NaCl. Quartz solubility under lithostatic conditions is much higher than that under hydrostatic conditions, and it increases monotonically with increasing depth (Table 4-4; Fig. 4-11b).

The fluid pressure in the upper continental crust is dominantly near-hydrostatic, whereas it changes gradually from hydrostatic to lithostatic conditions in the middle crust (~10–15 km depth) (Fig. 1-4a). If the fluid pressure changes at the hydrological boundary (3100 m depth), then quartz solubility has a local minimum at this depth, and would increase drastically from 195 mg/kg(H_2O) under hydrostatic conditions to 715 mg/kg(H_2O) under lithostatic conditions (Table 4-4; Fig. 4-11b). The solution samples taken from WD-1a at 3708 m depth have Si concentrations of 39–206 mg/kg(H_2O) (Table 4-5; NEDO, 1996), more similar to quartz solubility at 3790 m depth under hydrostatic conditions ($C_{Si,Qtz,eq}$ = 55 mg/kg(H_2O)) than to quartz solubility under lithostatic conditions ($C_{Si,Qtz,eq}$ = 1312 mg/kg(H_2O)) (Table 4-4), suggesting that any fluid pressure change to significantly overpressured conditions must occur at depths greater than 3700 m.

Accordingly, even if there are some uncertainties in the values of salinity and fluid pressure of Kakkonda, it is clear that quartz solubility has a local minimum close to the hydrological boundary, indicating that quartz precipitation could occur at this depth

from both the upward- and the downward-fluid. In addition, the downward-fluid provides greater potential for silica deposition than the upward-fluid from around the hydrological boundary, because the downwards decrease in silica solubility from 2300 to 3100 m is much greater than the upwards decline in solubility beneath 3100 m (Fig. 4-10b).

Table 4-4 Quartz solubility of the well WD-1a of the Kakkonda geothermal field calculated by using the program LonerAP (Akinfiev and Diamond, 2009).

Depth [m]	Temperature [°C]	Pressure [MPa]		Quartz solubility [mg/kg(H_2O)]			
		Hydrostatic	Lithostatic	Pressure	Hydrostatic	Lithostatic	Hydrostatic
				Salinity [wt%]	0	0	10
100	145	0.6	-		54	-	0.84
150	150	1	-		58	-	1.0
250	180	2	-		88	-	3.1
350	190	2.5	-		99	-	4.6
450	203	3.4	-		116	-	7.5
550	220	4	-		141	-	14
650	230	5	-		157	-	21
780	240	6	-		174	-	137
900	250	7	-		192	-	170
1000	260	7.5	-		210	-	200
1100	258	8.5	-		207	-	195
1150	260	8.6	-		211	-	201
1250	232	9.5	-		162	-	107
1350	225	10.5	-		151	-	21
1550	290	12	-		272	-	300
1620	270	12.5	-		234	-	235
1800	320	14	-		325	-	391
1850	290	14.5	-		276	-	303
2000	310	15.5	-		315	-	366
2200	340	17	-		347	-	445
2350	350	18.5	62		345	535	467
2550	360	20	77.5		327	614	486
2900	370	22.5	76		303	652	506
3100	380	24	82		195	715	515
3150	400	25	84.5		43	815	472
3350	450	26	88		33	1031	210
3500	510	27	92.5		38	1178	69
3790	590	29	98.5		55	1312	72

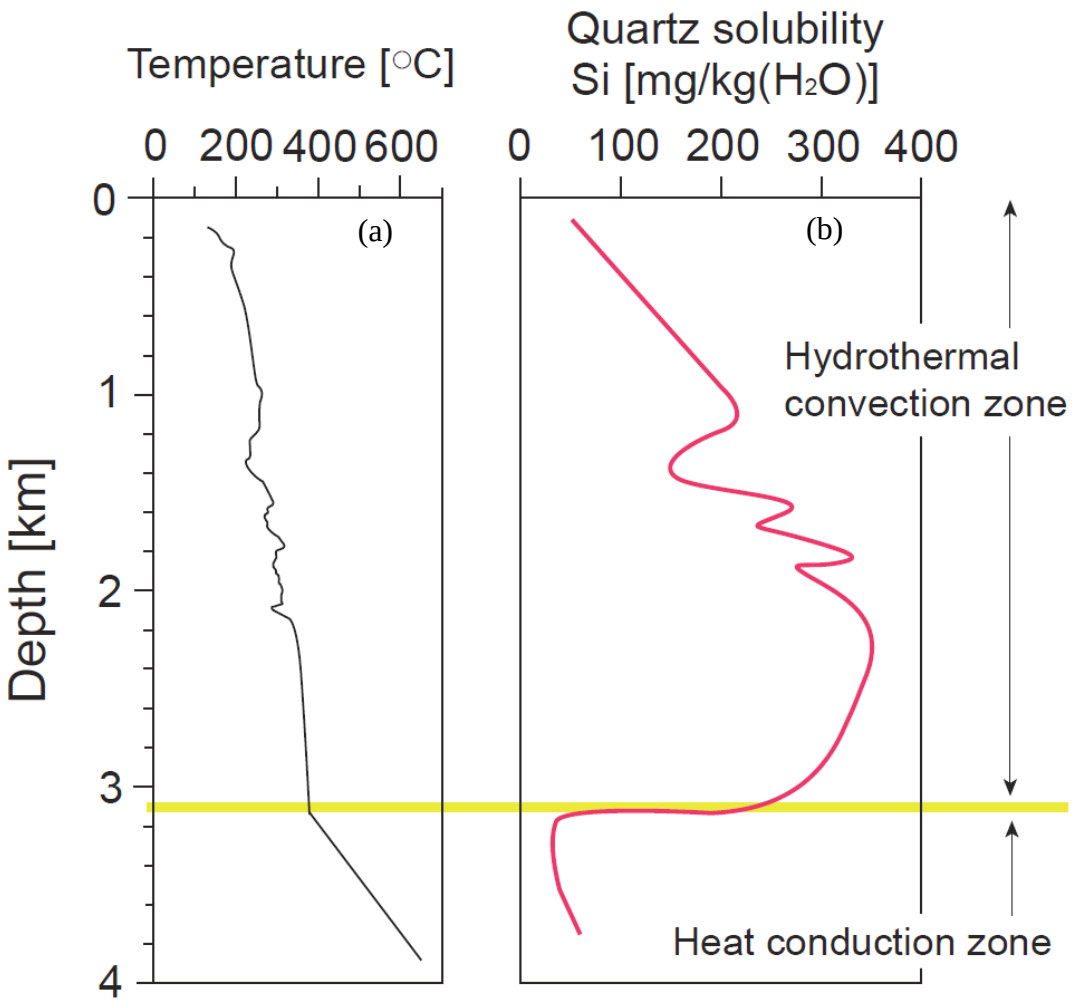

Figure 4-10 Temperature and quartz solubility profiles as a function of depth in the Kakkonda geothermal field. (a) Temperature-depth curve obtained for the drillhole WD-1a (Ikeuchi *et al*., 1998). (b) Quartz solubility with depth calculated by using the program LonerAP (Akinfiev and Diamond, 2009). The yellow line shows the boundary between the hydrothermal convection zone and the heat conduction zone (Doi *et al*., 1998). See text and Table 4-4 for detail.

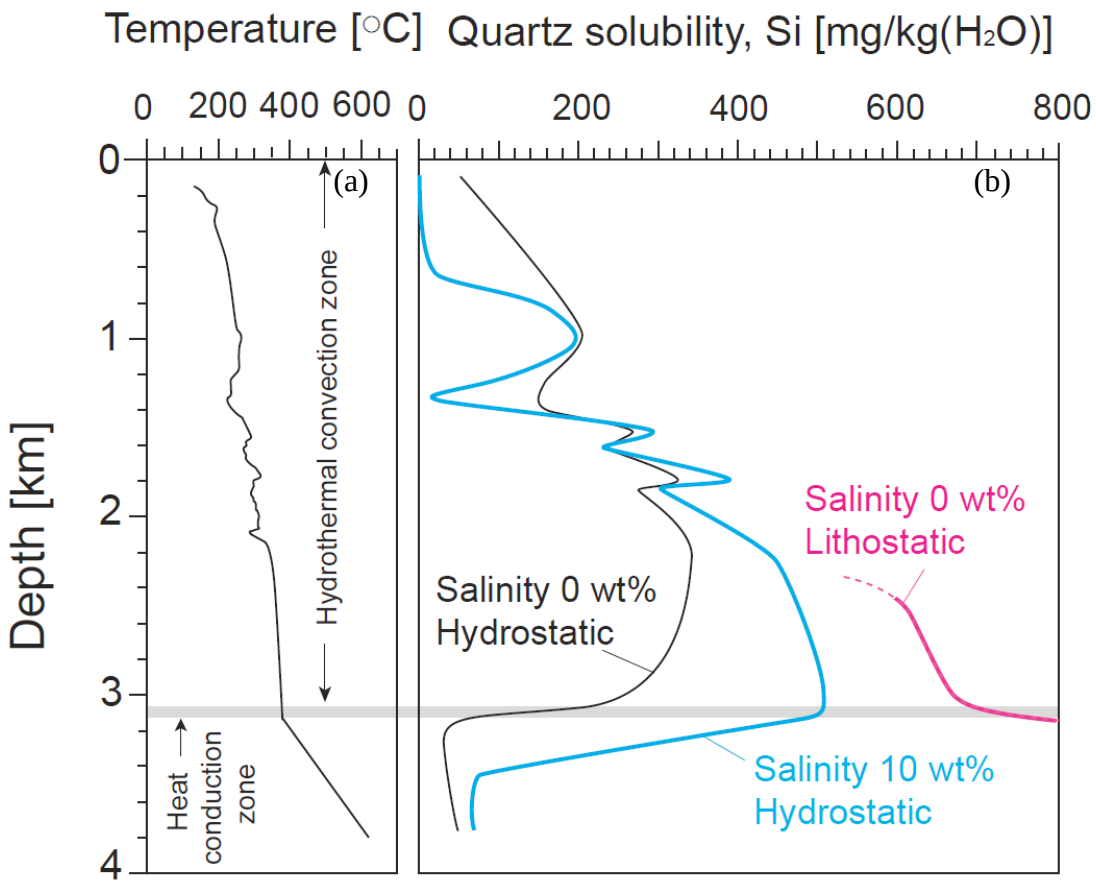

Figure 4-11 Temperature and quartz solubility profiles as a function of depth in the Kakkonda geothermal field. (a) Temperature-depth curve obtained for drillhole WD-1a (Ikeuchi *et al.*, 1998). (b) Quartz solubility with depth, calculated using the program LonerAP (Akinfiev and Diamond, 2009). Shown on the diagram are the solubility for pure H_2O under hydrostatic conditions (salinity = 0 wt%; black line), the solubility for saline fluid (10 wt% NaCl equivalent; blue line), and the solubility for pure H_2O under lithostatic conditions (salinity = 0 wt%; red line). The grey line at 3100 m depth shows the boundary between the hydrothermal convection zone and the heat conduction zone (Doi *et al.*, 1998).

Table 4-5 Conditions of the solution sampled from the well WD-1a of the Kakkonda geothermal field (modified after NEDO, 1996).

Sampling Date		Cirdculation depth [m]	pH	Density of water [g/cm^3]	Concentration [mg/kg][1]						
					Cl	SO_4	Na	K	Ca	Si	Al
7/25/1995	2:00	2500	9.1	-	4.3	8.8	3.7	0.6	12	8	1.1
	4:00	2716	9.0	-	2.8	9.9	9.6	3	12	17	2.5
	7:00	2932	8.6	-	2.3	9.9	10	6.4	9.4	29	3.7
	10:00	3158	8.1	-	3.1	15	11	6.4	11	43	6.7
	13:05	3374	5.4	-	500	29	180	88	68	103	2.8
	13:10	3374	5.5	-	250	30	79	41	31	61	2.8
	18:10	3590	5.4	-	130	14	46	28	37	61	3.7
	18:15	3590	5.3	-	260	14	79	51	54	79	6
7/25/1995	11:50	3708	5.2	1.304	190000	180	29000	41000	18000	39	3.7
	11:55	3708	5.4	1.219	190000	250	72000	25000	11000	56	0.7
	11:58	3708	6.3	1.039	27000	45	13000	2400	1600	84	2
	12:00	3708	6.2	1.009	6900	20	2900	820	530	206	4
	12:05	3708	6.1	1.004	2000	26	830	300	260	131	6.8
	12:10	3708	6.2	1.002	810	21	270	180	140	196	13
	12:15	3708	6.2	-	440	25	140	120	89	178	5
	12:20	3708	5.9	-	240	27	74	60	50	145	3

[1] Converted concentrations based on density of water at 3708 m depth.

4.5. Discussion

4.5.1. Relationship between quartz dissolution and fluid filled fractures

In the Kakkonda geothermal field, the productive fractures were expected at the margin of Kakkonda granite based on the lost circulation in the well-13 and 19 (Kato *et al*., 1993; Fig. 4-1b). Abundant near-horizontal fractures were observed in the core samples and FMI (Formation Micro-Imager) logs of WD-1a at this depth (Muraoka *et al.*, 1998). The strong reflectors at around 350 °C isotherm are interpreted to be fluid-filled fractures, based on the facts that (1) the location of the reflectors do not always consistent with the lithological boundaries (Matsushima *et al*., 2003), and (2) the quartz solubility has a local maximum at around 350 °C (Fig. 4-10b), where quartz is dissolved both in the upward- and the downward-fluids. Therefore, dissolution of quartz is important for preservation of open fractures.

4.5.2. Quartz precipitation at the permeable-impermeable boundary

4.5.2.1. Effect of mineralogy of silica precipitation on fracture sealing

The experimental results in the chapter 2 suggest the relationship among minor components in the solution, amount of silica precipitation (Fig. 2-9), and mineralogy of precipitated products (Fig. 2-14). These parameters are critical for the rate of fracture

sealing. Figure 4-12 shows the solubility of quartz (Q) and amorphous silica (AS) calculated by the program LonerAP (Akinfiev and Diamond, 2009) and SUPCRT92 (Johnson *et al*., 1992) in the conditions of the fluid pressures under lithostatic and hydrostatic along a geothermal gradient of 30 °C/km. The solubility of quartz under lithostatic conditions exceeds that of amorphous silica under hydrostatic conditions at T >400 °C. When the fluid pressure changes from lithostatic to hydrostatic at T = 480 °C, the initial solution (point A) is supersaturated not only with quartz but also with amorphous silica, similar to our experimental conditions. The experiments of minor components in the solution in the chapter 2 revealed that amorphous silica forms in low-Al solutions, whereas quartz nucleates in high Al solutions (Fig. 2-14). The amount of silica that precipitates during the change from point A to point C is more than five times greater than that during the change from point A to point B (Fig. 4-12), suggesting that trace amounts of Al and Na in fluids have a strong influence on the rate of fracture sealing at the permeable-impermeable boundary in the Earth's crust.

4.5.2.2. Effect of nucleation on fracture sealing

Highly supersaturated solutions (Ω_{Qtz} >~2) could be generated under the conditions around the hydrological boundary of the Kakkonda geothermal field and cause silica

precipitation via nucleation. For example, when the fluid flows downwards just 50 m, from 3100 m depth to 3150 m depth under the hydrostatic condition, the fluid is predicted to become highly supersaturated in silica (Ω_{Qtz} = ~4.5; Table 4-4; Fig. 4-10b). When there is a transition to overpressured conditions at 3100 m depth, a pressure drop from lithostatic to hydrostatic could generate highly supersaturated fluids in silica (Ω_{Qtz} = 3.7; Fig. 4-11b) as mentioned above. In both cases, nucleation-controlled precipitation of quartz occurs easily, and seals fractures or pores effectively even in rocks devoid of quartz, as observed in quartz veins with blocky textures (Okamoto and Tsuchiya, 2009).

4.5.2.3. Observations of fracture sealing at the permeable-impermeable boundary

In the well WD-1a, abundant quartz veins are not observed in the core samples from around the hydrological boundary, although there are a few veins and grain-boundary fillings of quartz and other minerals (Kato *et al*., 1998; Sasaki *et al*., 2003). In the Geysers geothermal field in the United States, a relatively impermeable barrier containing abundant quartz veins was observed at 3475–3600 m depth, where temperature was higher than 350–370 °C (Fournier, 1991). The lack of abundant quartz veins at the boundary of the Kakkonda geothermal field is probably because quartz

veins were missed by chance even though they are there, or because quartz creep affects the bottoming permeability as well as quartz precipitation (Fournier, 1999).

4.5.2.4. Silica precipitation at the brittle-ductile transition of geothermal fields

Supercritical fluid is divided into liquid-like and vapour-like regions (Morita *et al*., 2000; Tsuchiya and Hirano, 2007), and the *P*–*T* conditions at the hydrological boundary of the well WD-1a (380 °C and 24 MPa) correspond to the vapour-like region (Fig. 4-14). The fluid flow from the higher density liquid region into the lower density supercritical region causes a drop in quartz solubility, which drives quartz precipitation. With increasing fluid pressure from 20 to 100 MPa, the local maximum in quartz solubility shifts from ~300 to ~500 °C and the magnitude of the drop in solubility become smaller (Fig. 4-13). The high geothermal gradient (>~50 °C/km) intersects with the quartz solubility ridge in the typical temperature range of the BPT (300–450 °C; Fig. 4-14), and fracture sealing, build-up of fluid overpressure, and permeability regeneration by fracturing would repeatedly occur around the hydrological boundary. The dissolution and precipitation of silica appears to play an essential role in shaping the permeability and flow pattern and controlling the depth of the BPT in geothermal systems.

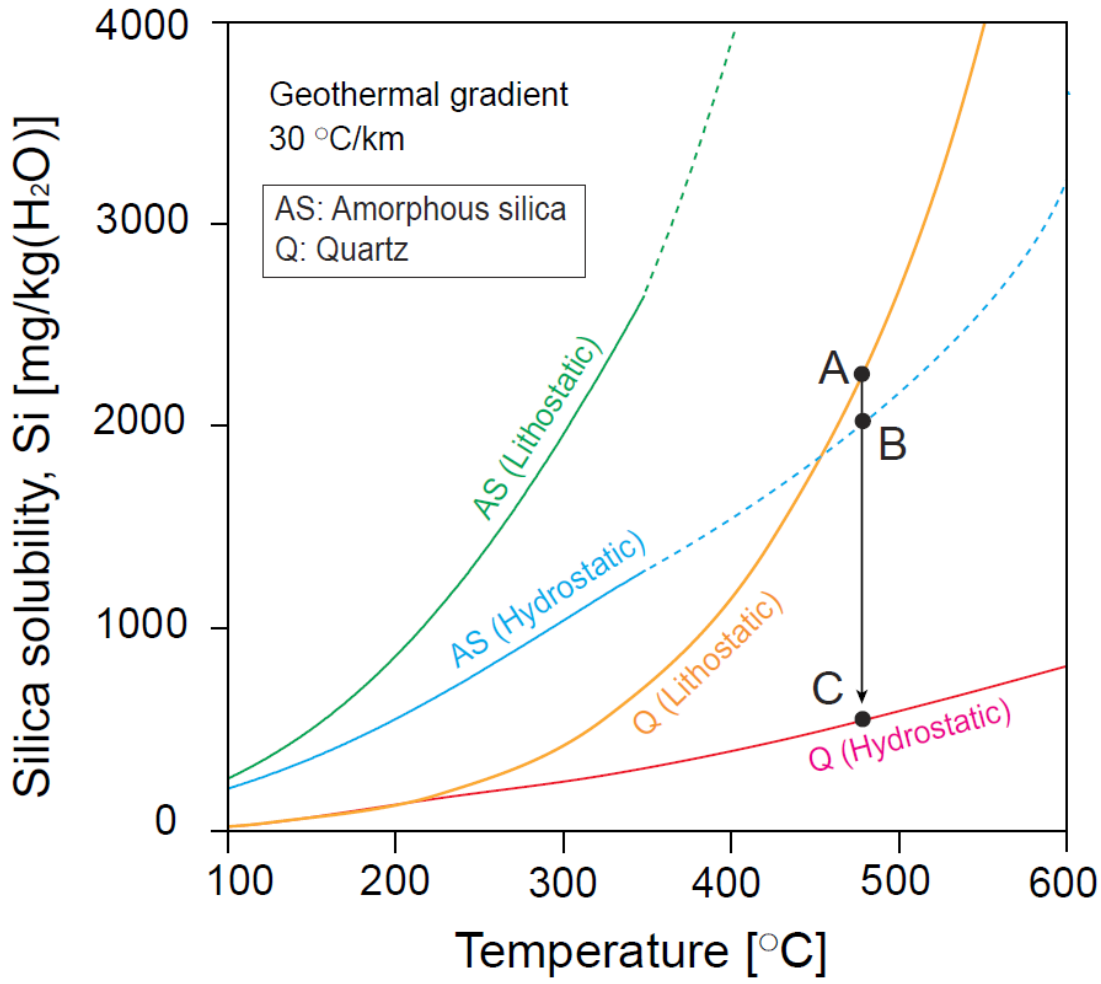

Figure 4-12 Temperature-dependent solubilities of quartz (Q) under lithostatic (yellow curve) and hydrostatic (red curve) conditions, and that of amorphous silica (AS) under lithostatic (green curve) and hydrostatic (blue curve) conditions. The solubilities are along a geothermal gradient of 30 °C/km. Consider that the fluid is initially saturated with quartz under lithostatic conditions (point A) at 480 °C. When the fluid pressure changes from lithostatic to hydrostatic, the fluid chemistry changes from point A to point B via precipitation of amorphous silica, and from point A to point C via precipitation of quartz. See text for details.

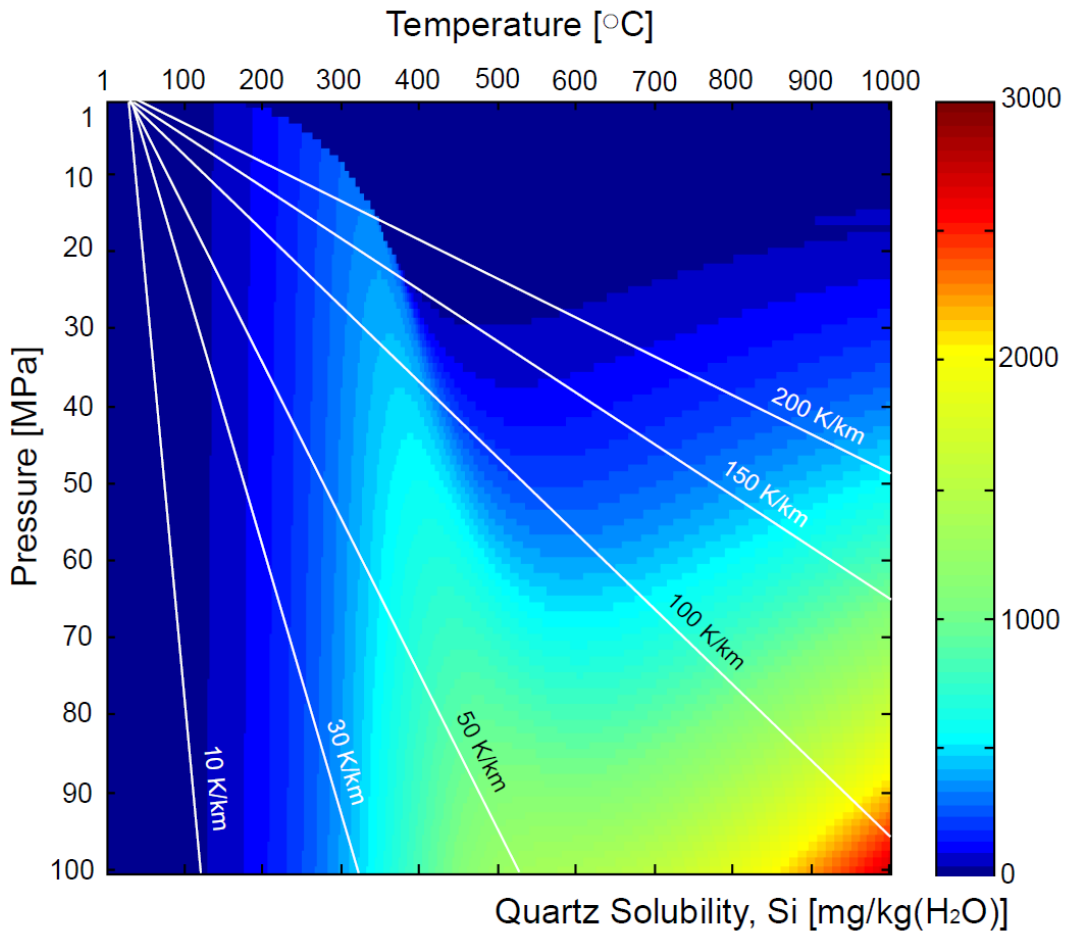

Figure 4-13 Color plots of the quartz solubility at 1–1000 °C and 1–100 MPa (ASME steam tables for industrial use, 2000; Fournier and Potter, 1980). The collar bar shows that the quartz solubility increases from 0 to 3000 mg/kg(H_2O) with changing of collar from blue to red. The white lines show the geothermal gradient of 10, 30, 50, 100, 150, and 200 K/km.

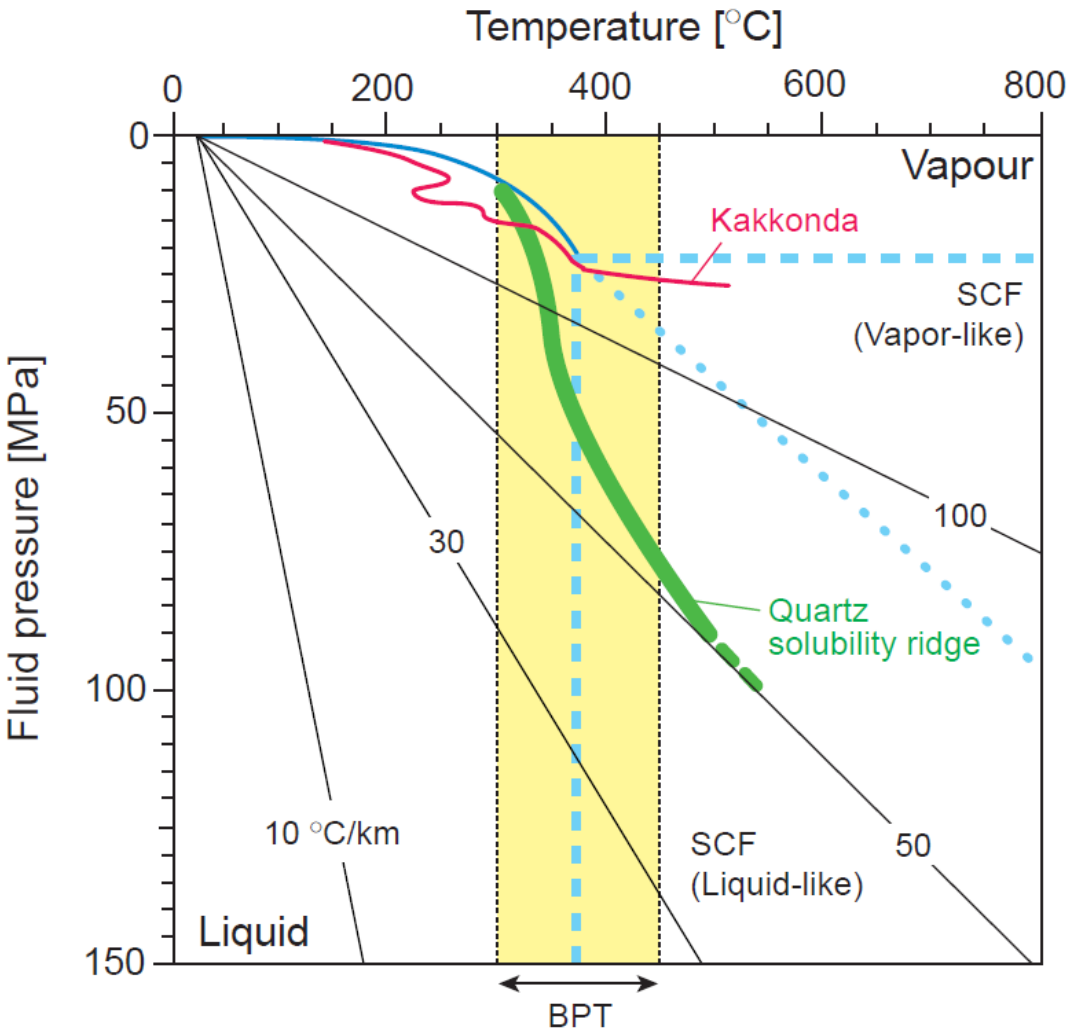

Figure 4-14 *P–T* diagram for the Kakkonda geothermal field showing the maximum quartz solubility ridge. The red line indicates the *P–T* conditions of the Kakkonda geothermal field under hydrostatic conditions. The quartz solubility ridge (bold green curve) indicates the trace of maximum quartz solubility at each pressure (see Fig. 4-13); quartz precipitates easily on the higher-temperature side of this ridge. Black lines indicate the geothermal gradients of 10, 30, 50, and 100 °C/km under hydrostatic conditions. The blue line is the boiling curve. The bold broken blue lines at 374 °C and 22 MPa are the boundaries between H_2O states: vapour, liquid, and supercritical fluid (SCF). The dotted blue line indicates that the supercritical water is divided into liquid-like and vapour-like regions (Morita *et al.*, 2000; Tsuchiya and Hirano, 2007). The yellow zone shows the temperature range of the BPT for normal continental crust (300–450 °C).

4.6. Conclusions

The hydrological system within Earth's crust is divided into the permeable zone and the underlying, much less permeable zone. In this chapter, the solubility and precipitation kinetics of silica in water were investigated under the conditions of the Kakkonda geothermal field, Japan, where the well WD-1a penetrated the boundary between the hydrothermal convection zone and the heat conduction zone. EPMA analysis of silica scale and hydrothermal vein of the Kakkonda geothermal field showed that Al was a next largest component of Si in scales. The concentration of Al correlated with K in fine-grained aggregate whereas Ca and other elements existed with Al in massive part. Calculation of quartz solubility along the well WD-1a revealed the depth of a local minimum of quartz solubility correlated with that of the hydrological boundary at ~3100 m depth (380 °C and 24 MPa), in either case of hydrostatic conditions or of fluid pressure increase above hydrostatic at deeper levels. The hydrothermal experiments of silica precipitation revealed that rapid quartz precipitation could occur via nucleation when fluids are brought from the liquid region to the supercritical region. The preferential precipitation of quartz at a specific depth plays a significant role in forming and sustaining the permeable-impermeable boundary in the crust.

5. GEOCHEMICAL EVOLUTION OF THE PERMEABLE-IMPERMEABLE BOUNDARY

5.1. Introduction

In the chapter 4, the characteristic trend of the quartz solubility along depth was expected to affect to the form of the fluid-filled fractures and the permeable-impermeable boundary. If flow rate is slow, fluid is saturated with quartz. In this case, the depth of dissolution and precipitation of silica minerals is determined from the equilibrium theory. The temperature structure has been discussed based on the numerical results in the Kakkonda geothermal field (Hanano, 1998; Ehara, *et al*., 2001). Based on these data, the temporal silica-water interaction of the Kakkonda geothermal field could be simulated by calculating quartz solubility as a function of temperature and pressure (or density of water).

However, fluid saturated with quartz is not always realized depending on flow rate. Extremely high rate of fluid ascent during blocky vein formation (10^{-2} to 10^{-1} m/s) could be occurred due to the low viscosity of the hydrothermal fluid (~10^{-4} Pa·s) probably because of the injection of fluids from mobile hydrofractures within deeper levels of the subduction zone (Okamoto and Tsuchiya, 2009). At the permeable-impermeable boundary, the rapid change of pressure from lithostatic to

hydrostatic may also result the fast fluid flows. In addition, the compositions of crustal fluid and the reaction surface area of quartz in the host rocks are various spatially. Because the dissolution and precipitation rate of silica minerals depends on not only quartz solubility but also flow rate, surface area of quartz, and compositions of fluid, temporal and spatial evolution of crustal conditions should be estimated based on the kinetic theory.

In this chapter, simulation of the precipitation rate of silica minerals along the well WD-1a in the Kakkonda geothermal field revealed the geochemical evolution of the crustal conditions, especially the permeable-impermeable boundary within the Earth's crust.

5.2. Components of crustal fluid in the Kakkonda geothermal field

The fluid sampled from the well WD-1a at 2900–3708 m depth revealed the composition of the crustal fluid across the permeable-impermeable boundary of the Kakkonda geothermal field. Si concentration in the fluid ranges from 8 to 29 mg/kg in the hydrothermal convection zone (<3100 m depth) and increases up to 103 mg/kg(H_2O) in the heat conduction zone at 3150–3590 m depth (NEDO, 1996; Table 4-5). Al concentration in the fluid of the well WD-1a increases from 1.1 to 6.7

mg/kg(H_2O) with increasing depth toward the permeable-impermeable boundary (NEDO, 1996; Table 4-5). Si and Al concentrations in the fluid from the bottom of the well WD-1a range 39–206 mg/kg(H_2O) and 0.7–13 mg/kg(H_2O) under the boundary probably because the fluid composition changed with time during fluid sampling (eight samples during 30 minutes); Si concentration is 39–84 mg/kg(H_2O) within 10 minutes, and then it increases to 131–206 mg/kg(H_2O) in 10–30 minutes (NEDO, 1996; Table 4-5). Because the salinity of the fluids decreases with time by 1–2 orders during the fluid sampling (NEDO, 1996; Table 4-5), it has been interpreted that the compositions of the fluid which was sampled <10 minutes represent the close to the original bottom fluids. The relationship of concentrations of Si and Al in the fluid from the well WD-1a is shown in Figure 5-1 with that of the input solutions of the precipitation experiments of minor components in the chapter 2 (Table 2-5).

The concentrations of Al^{3+} and H_4SiO_4 in the solution in equilibrium with albite and H_2O was calculated by using the program SOLVEQ-XPT (Reed *et al.*, 2010). Pressure was set to be 30 MPa, which is the same as the experimental condition of minor components. Temperature was 350 °C where amount of albite dissolution is maximum in the pre-experiment (Table 2-3; Fig. 2-5). Si concentration was 350 mg/kg(H_2O). Al and Na concentrations varied 0, 1, 3, 7, 10, 12, 17, and 30 mg/kg(H_2O).

The value of pH was set to be 8 for the solution of C_{Al} = 30 mg/kg(H_2O) and to be 7 for other conditions based on the pH values in the experiments of this study (Table 2-5). For taking a balance of ion charge, SO_4^{2-} of 0.01 mg/kg(H_2O) was input in the initial conditions because S is assumed to dissolve from SUS316 tube. The dissolution of albite in water is written as

$$NaAlSi_3O_8 + 4H_2O + 4H^+ = Na^+ + Al^{3+} + 3H_4SiO_4 . \quad (40)$$

Then the equilibrium constant, K, is given by

$$K = \frac{a_{Na^+} a_{Al^{3+}} \left(a_{H_4SiO_4}\right)^3}{a_{NaAlSi_3O_8} \left(a_{H_2O}\right)^4 \left(a_{H^+}\right)^4} \quad (41)$$

$$\log K = \log a_{Na^+} + \log a_{Al^{3+}} + 3\log\left(a_{H_4SiO_4}\right) - 4\log\left(a_{H^+}\right) \quad (42)$$

where a_i is activity of element i. In the solution of each concentrations of Al and Na, the activity of H_4SiO_4 is

$$\log a_{H_4SiO_4} = \frac{\log K + 4\log\left(a_{H^+}\right) - \log a_{Na^+} - \log a_{Al^{3+}}}{3} . \quad (43)$$

The value of activity of H_4SiO_4 is converted to molality

$$b_{H_4SiO_4} = a_{H_4SiO_4} / \gamma_{H_4SiO_4} \quad (44)$$

where $b_{H_4SiO_4}$ is the molality of H_4SiO_4 (mol/kg) and $\gamma_{H_4SiO_4}$ is the activity coefficient of H_4SiO_4, respectively. In this calculation, $\gamma_{H_4SiO_4}$ is derived to be 1. Concentration of Si, C_{Si}, is given by

$$C_{Si} = b_{H_4SiO_4} \times m_{Si} \times 1000 \quad (45)$$

where m_{Si} is the molecular mass of Si, 28.09 g/mol.

Equilibrium concentration of Si in the solution is higher than 300 mg/kg(H_2O) in the solution of Al and Na concentrations <7 mg/kg(H_2O) whereas it decreases with increasing of Al (= Na) concentration to 30 mg/kg(H_2O) (Fig. 5-1). The compositions of the solutions made by dissolution of albite and silica minerals in this study (quartz or amorphous silica; Table 2-5; Fig. 2-6) correlates with the calculated curve of Si and Al concentration (Fig. 5-1). The reason why the input solution of C_{Si} >300 mg/kg(H_2O) with C_{Al} >10 mg/kg(H_2O) could not be prepared experimentally is suspected that Si

concentration is controlled by Al concentration, or vice versa, in the equilibrium state. Thus, the possible compositions of Al and Si in the crustal fluid were covered in the experiments of this study (Fig. 5-1). The Si and Al concentrations in the Kakkonda geothermal fluid distributes below the equilibrium curve of albite-H_2O. In addition, the Si concentration in the Kakkonda geothermal fluid is higher than that expected from the stoichiometry of albite, 0.33 (Al:Si = 1:3) (Fig. 5-1). The host rock at the depth of the fluid sampling (>2900 m) in the well WD-1a is Kakkonda granite (Doi *et al*., 1998). Therefore, it is reasonable to consider that Si and Al concentrations in the Kakkonda geothermal fluid are controlled by dissolution of granite and that the compositions are similar to those in the experiments of this study.

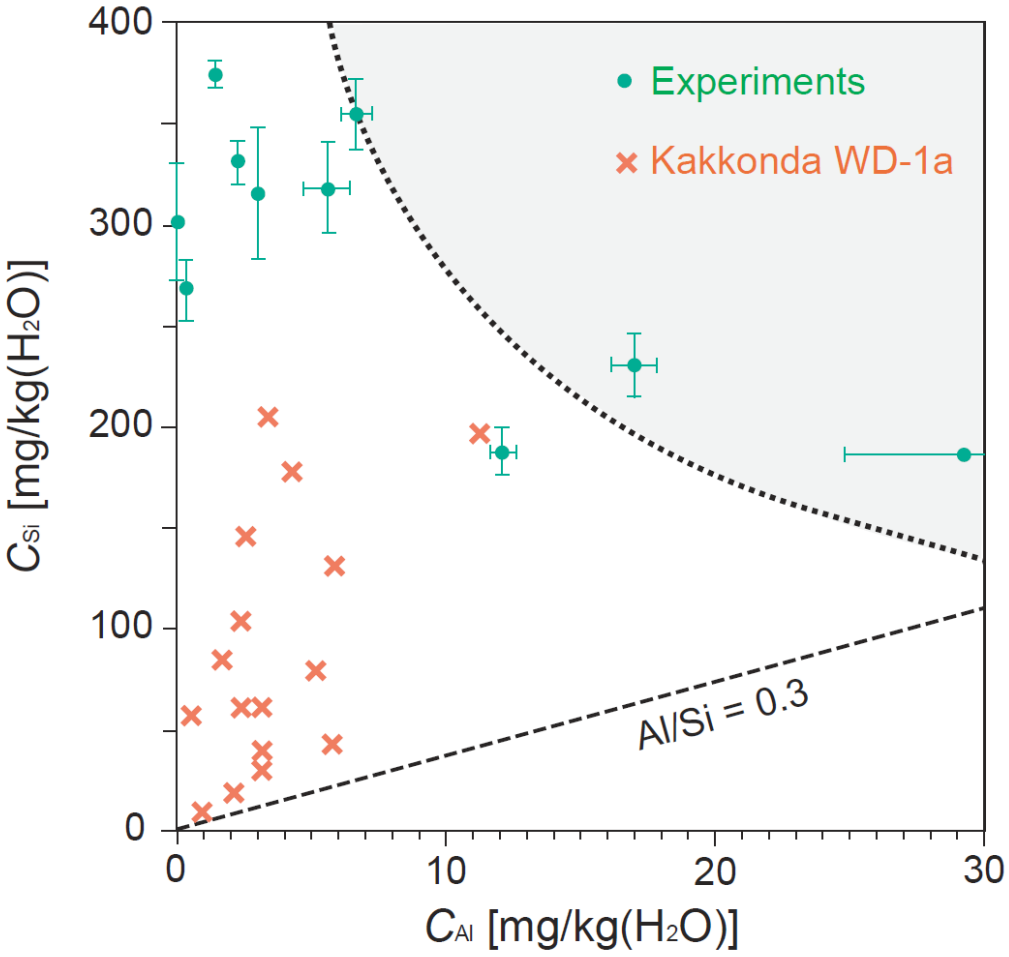

Figure 5-1 Al and Si concentrations in the input solutions in the experiments of minor components in the solution (green circle) and that in the solution sampled from the well WD-1a of the Kakkonda geothermal field (red cross). The dotted line shows the equilibrium concentrations related with albite-H_2O reaction at 350 °C and 30 MPa calculated by using the program SOLVEQ-XPT (Reed *et al.*, 2010). The broken line shows the stoichiometric ratio of Al and Si, Al/Si = 0.3.

5.3. Calculation of silica-water interaction in the Kakkonda geothermal field

In this section, the reaction rates of dissolution and precipitation of silica minerals in the Kakkonda geothermal fluid were estimated by applying to the empirical kinetic equation in the chapter 3. The parameters of the kinetic equation are the ratio of reaction surface and mass of water, A_{Qtz} / M_{H_2O}, residence time in the system, quartz solubility, and Si and Al concentrations in the input solution. For simplify, a fracture of parallel planes was considered.

Reaction rate of dissolution and precipitation of silica was estimated along the condition of the Kakkonda geothermal field, at which quartz solubility was calculated in the chapter 4 (Table 4-2). Direction of fluid flow was considered in two ways, upward and downward, because the geothermal fluids in the shallow reservoir are interpreted to result from the mixing of hypersaline fluids from a residual magma with heated large amount of meteoric water (Muramatsu *et al*., 2000; Kasai *et al*., 1998). Example of the direction of fluid flow is shown in Fig. 5-2a. Fluid flows from the start point where the solution is saturated with quartz to the end point that is one step shallower or deeper part of the start point (Fig. 5-2a). At each depth, the initial fluid was assumed to be saturated with quartz. Therefore, the value of quartz solubility in Eq. 33, $C_{Si,Qtz,eq}$, was that at the depth of the start point. Dissolution or precipitation occurs reflecting the

difference of quartz solubilities between the start and end points. The Si concentration in the fluid at ground, 0 m depth, was assumed to zero.

A parallel fracture of 1 mm width is assumed to be in the system of the rectangle of the cross section of 1 m^2 and the height of the distance from the start point to the end point of fluid flow, *dL* m (Fig. 5-2b). One side of reaction surface faces with another surface, thus there are 2 sides of reaction surfaces. The one side area of fracture surface was 1 × *dL* m^2. The area of quartz surface, A_{Qtz}, is assumed to occupy 30 % of the host rock (e.g., granite). The cross section of the fracture, A_f, is 0.01 m^2. The ratio of quartz surface and mass of water, A_{Qtz} / M_{H_2O} [m^2/kg], is determined as follows:

$$\frac{A_{Qtz}}{M_{H_2O}} = \frac{2dL \times 0.3}{A_X \times dL \times \rho_{H_2O}} \tag{46}$$

where ρ_{H_2O} is the density of water [kg/m^3] calculated by using the program LonerAP (Akinfiev and Diamond, 2009). The fracture permeability ranged from 1 × 10^{-9} to 1 × 10^{-14} m^2. The residence time of fluid in the system, Q_f/A_f [m/s], is estimated by using Darcy's law

$$\frac{Q_{\mathrm{f}}}{A_{\mathrm{f}}} = -\frac{\kappa}{\mu}\frac{dP}{dL} \tag{47}$$

where Q_{f} is flow rate [m^3/s], κ is permeability [m^2], μ is viscosity [Pa s], respectively. The vertical bulk permeability of the Kakkonda geothermal field ranges from 10^{-14} to 10^{-17} m^2 (Hanano and Takanohashi, 1993; Fujimoto *et al*., 2000). The fracture permeability, μ, is varied from 1×10^{-9} to 1×10^{-16} m^2 in this calculation, covering the permeability range of the Kakkonda geothermal field. Viscosity of pure water is set based on ASME international steam tables (Parry, 2000; Table 5-2). Difference of pressure between the depth of the start and the end points, *dP* [Pa], is following the conditions of quartz solubility at the Kakkonda geothermal field (Table 4-1). The residence time, *t* [sec], is given by

$$t = dP \times \left(\frac{Q_{\mathrm{f}}}{A_{\mathrm{f}}}\right)^{-1}. \tag{48}$$

The rate constants of surface reaction and nucleation at each depth are shown in Figure 5-4b. The rate constant of surface reaction was calculated by using Eq. 27 (Okamoto *et al*., 2010) and temperature data of the WD-1a (Ikeuchi *et al*., 1998; Fig. 4-10a). At the depth of ~3200 m of the well WD-1a, Al concentration in the solution,

C_{Al}, which is needed to determine the rate constant of nucleation, are derived in a function of depth as follows:

$$C_{Al} = 1.6 \times 10^{-3} \exp(2.7x) \quad (49)$$

where x is depth along the well (km) (Fig. 5-3). Al concentration in the solution at deeper part of >3200 m depth was determined based on the average of the observed values (Table 5-1; Fig. 5-3). Al concentration in the solution of the well WD-1a is larger than 1 mg/kg(H_2O) and less than 8 mg/kg(H_2O) (Table 5-1; Fig. 5-4a). Therefore, the rate constants of nucleation, k_N, were calculated by using Eq. 38 (Table 5-1; Fig. 5-4b). *PT* condition is 370 °C and 22.4 MPa at 2900 m depth of the WD-1a (Table 4-2). Considering the critical condition of water at 374 °C and 22 MPa, silica-water interaction at deeper parts of 2900 m depth occurs in the supercritical conditions of water. Therefore, the nucleation parameter, α, is 1 at the depth of >2900 m, leading that the nucleation rate is determined only at >2900 m depth to apply the nucleation term in Eq. 33 in the calculation (Table 5-1; Fig. 5-4b).

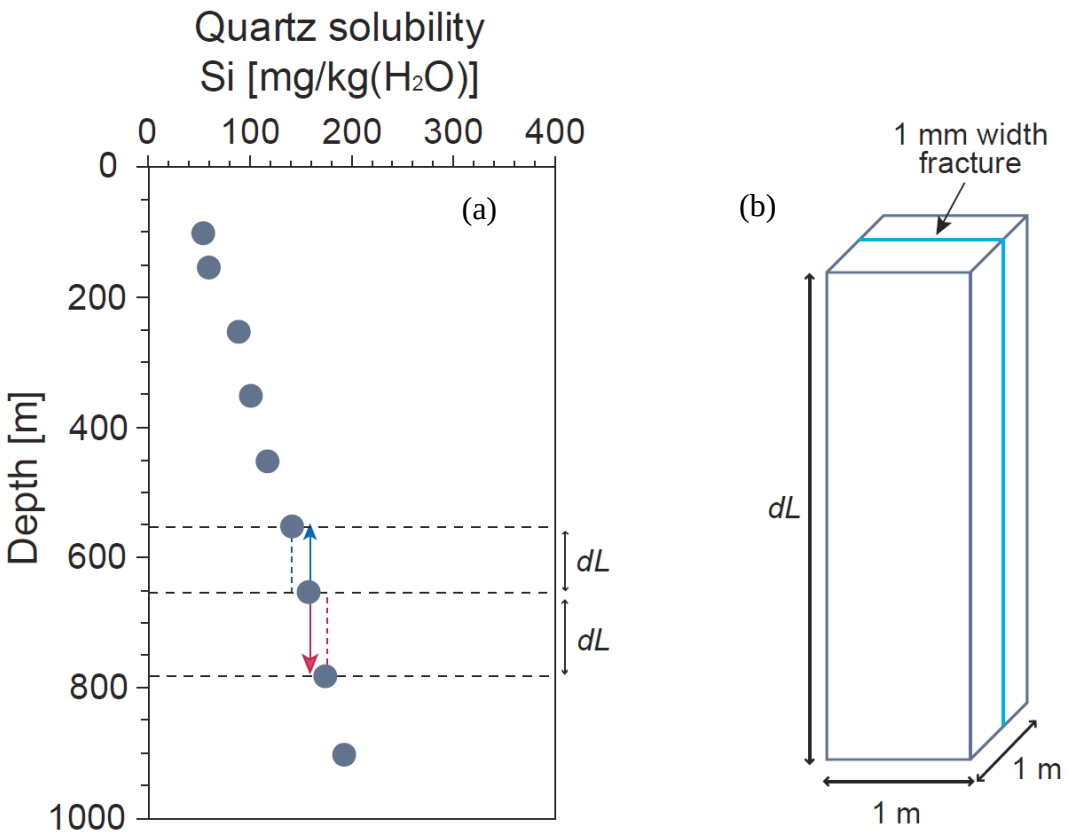

Figure 5-2 (a) Quartz solubility at the depth of 0-1 km in the well WD-1a of Kakkonda geothermal field (see Table 4-1), and the directions of fluid as an example; the start point at 650 m depth, direction of up (blue) and down (red), and the end points at 550 and 780 m depth, respectively. (b) A parallel fracture system for estimation of the reaction rate of silica dissolution or precipitation during fluid flow-through from the start point to the end point shown in Fig. 5-2a. The distance between the start and the end points is *dL* (m). The fracture width is 1 mm.

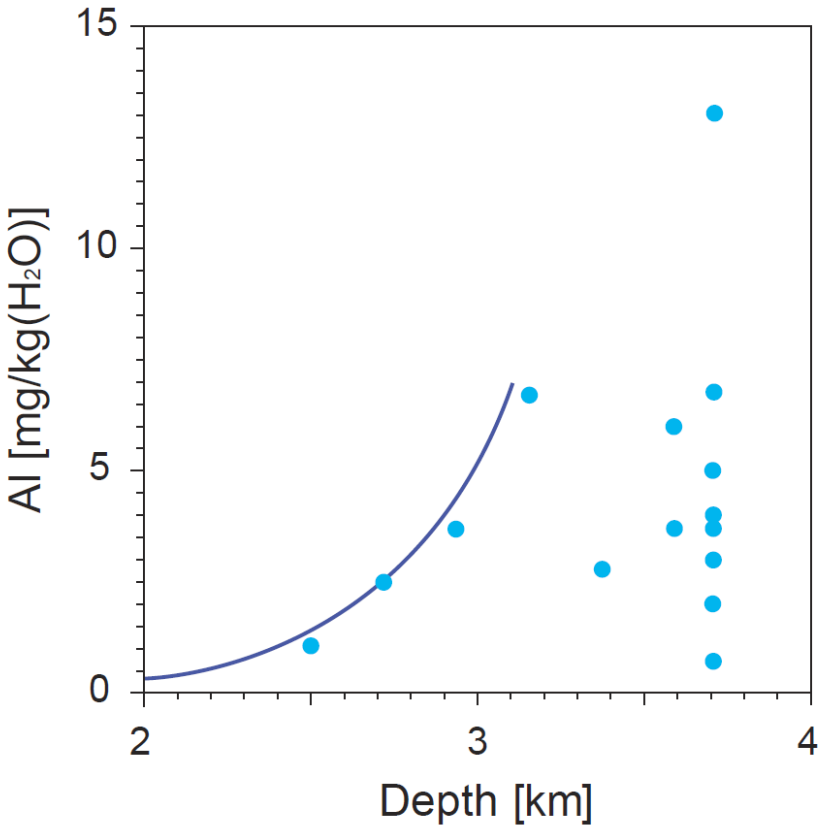

Figure 5-3 Al concentration in the fluid sampled at the depth of 2900–3708 m of the well WD-1a of the Kakkonda geothermal field (Table 4-5).

Table 5-1 *PT* conditions and reaction rate constant along the well WD-1a of the Kakkonda geothermal field.

Depth [m]	Pressure [MPa]	Temperature [°C]	C_{Al} [1] [mg/kg(H_2O)]	$Log_{10} k_S$ [2]	$Log_{10} k_N$ [3]
100	0.6	145	0.002	-6.4	-
150	1.0	150	0.002	-6.3	-
250	2.0	180	0.003	-5.9	-
350	2.5	190	0.004	-5.8	-
450	3.4	203	0.005	-5.6	-
550	4.0	220	0.007	-5.4	-
650	5.0	230	0.009	-5.3	-
780	6.0	240	0.013	-5.2	-
900	7.0	250	0.018	-5.1	-
1000	7.5	260	0.024	-5.0	-
1100	8.5	258	0.031	-5.1	-
1150	8.6	260	0.036	-5.0	-
1250	9.5	232	0.047	-5.3	-
1350	10.5	225	0.061	-5.4	-
1550	12.0	290	0.105	-4.8	-
1620	12.5	270	0.127	-4.9	-
1800	14.0	320	0.206	-4.5	-
1850	14.5	290	0.236	-4.8	-
2000	15.5	310	0.354	-4.6	-
2200	17.0	340	0.608	-4.4	-
2350	18.5	350	0.911	-4.3	-
2550	20.0	360	1.564	-4.3	-
2900	22.5	370	4.024	-4.2	-2.3
3100	24.0	380	6.905	-4.1	-2.1
3150	25.0	400	7.903	-4.0	-2.0
3350	26.0	450	2.800	-3.7	-2.3
3500	27.0	510	4.850	-3.5	-2.2
3790	29.0	590	4.775	-3.1	-2.2

[1] Al concentration in the solution.

[2] Rate constant of surface reaction of quartz.

[3] Rate constant of nucleation of silica minerals.

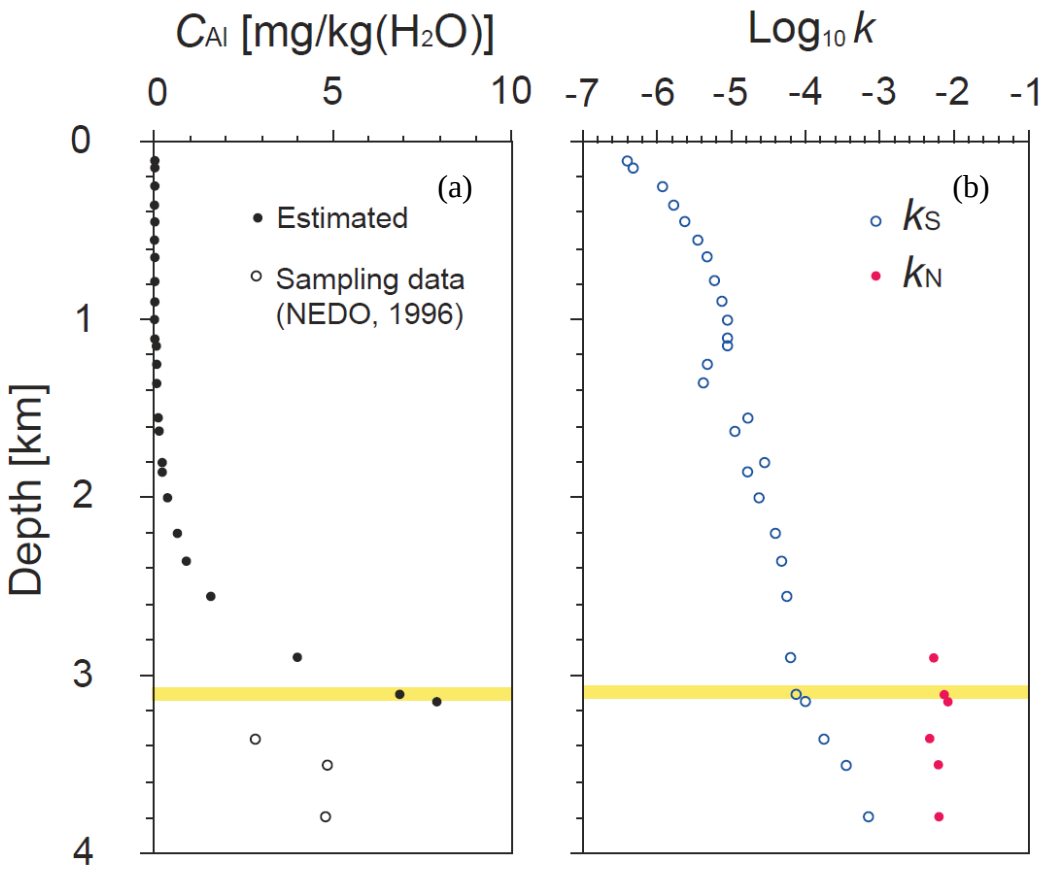

Figure 5-4 (a) Al concentration in the solution along the well WD-1a of the Kakkonda geothermal field. The values from the ground to 3200 m depth were estimated by using Eq. 49 (black circles). At the depth of >3200 m, observed values (Table 4-5) are plotted (white circles). (b) Rate constant of surface reaction of quartz (blue) calculated by using temperature data in the well WD-1a of the Kakkonda geothermal field (Table 5-1; Fig. 4-10a) and that of nucleation of silica minerals (red) calculated in Eq. 38 by using Al concentration in the solution (Table 5-1; Fig. 5-4a). The permeable-impermeable boundary in the well WD-1a of the Kakkonda geothermal field is at 3100 m depth (yellow line).

5.4. Results

Difference of Si concentration in the solution between the start point and the end point, dC_{Si} mg/kg(H_2O), were calculated at each depth of the Kakkonda geothermal field (following the model; Fig. 5-2) by using the new kinetic equation of overall silica-water reaction (Eq. 33) with the calculated rate constants of quartz surface reaction and nucleation of silica minerals (Table 5-1). The positive and negative values of dC_{Si} suggest dissolution and precipitation, respectively.

At the fracture permeability of $\mu = 1 \times 10^{-9}$ m^2, the dC_{Si} at the shallower part of >2900 m depth in liquid phase is nearly zero in both upward- and downward-fluids (Table 5-3, 5-4; Fig. 5-5a, b). Around the permeable-impermeable boundary, dissolution of quartz results dC_{Si} = 12 mg/kg at 2900 m (Table 5-3; Fig. 5-5a) because the reaction rate increases with increasing of temperature to 370 °C (Table 5-1; Fig. 5-4b) and large increase of quartz solubility from 195 mg/kg(H_2O) at 3100 m depth (start point) to 303 mg/kg(H_2O) at 2900 m depth (end point) (Table 5-3). On the other hand, the largest amount of silica precipitation occurs in the downward-fluid at 3150 m depth (Table 5-4; Fig. 5-5b) because of applying the reaction rate via nucleation of silica minerals with the surface reaction rate in the supercritical conditions of water (Fig. 5-4) and the large

decrease of quartz solubility from 195 mg/kg(H_2O) at 3100 m depth (start point) to 43 mg/kg(H_2O) at 3150 m depth.

Amount of change of Si concentration in the solution, dC_{Si}, increases with decreasing of the fracture permeability from 1×10^{-9} to 1×10^{-13} m^2. The largest amount of dC_{Si} in the upward-fluid is shifted from 2900 m to 3100 m depth at the permeable-impermeable boundary with increasing of the fracture permeability from 1×10^{-9} m^2 to 1×10^{-11} m^2 (Table 5-3; Fig. 5-5). Residence time of fluid in the system increased due to permeability and became enough for the fluid in equilibrium state (Table 5-3, 5-4; Fig. 5-5). At permeability of 1×10^{-14} m^2, the upward- and the downward-fluids become saturated with quartz at the end point of all depth (Table 5-3, 5-4). Thus, the dC_{Si} values at the fracture permeability from 1×10^{-14} to 1×10^{-16} m^2 are same due to the difference of quartz solubility between the start and the end points. However, the fluid becomes saturated even at permeability of higher than 1×10^{-14} m^2 in the supercritical conditions of water at the depth of >2900 m (Table 5-3, 5-4). Especially for precipitation (dC_{Si} <0 mg/kg(H_2O)), both upward- and downward- fluid become saturated to quartz during the flow-through from the start point to the end point even at the fracture permeability of 1×10^{-9} m^2 whereas the fluid is not saturated by dissolution of silica minerals. For example, the downward-fluid is saturated at 2900 m

depth in the condition of permeability, $\mu = 1 \times 10^{-9}$ m^2 (Table 5-4). This trend is caused by the rapid precipitation rate of nucleation of silica minerals.

Calculated amount of silica precipitation revealed how long it takes for sealing a parallel fracture in the system. Figure 5-6 shows the timescale of fracture sealing at the fracture permeability of 1×10^{-13} m^2. At the shallower part of >1000 m depth, precipitation occurs only in the upward-fluid. The fastest fracture sealing at the part of >1000 m depth occurs at 900 m depth and takes at least 4.7×10^5 years. At 1000–2000 m depth, silica precipitation occurs in both upward- and downward-fluids and seals a fracture for >1000 years. At the depth from 2000 to 3200 m under the permeable-impermeable boundary, fracture sealing is caused by silica precipitation in the downward-fluid. The fastest sealing of a fracture is at 3150 m depth for 896 years.

The timescale for fracture sealing depends on the fracture permeability (Fig. 5-7). At the fracture permeability of 1×10^{-9} m^2, the fracture at 3150 m depth could be sealed for 52 days. The time for fracture sealing increases with decreasing of permeability.

Table 5-2 Conditions of water along the well WD-1a.

Depth [m]	Pressure [MPa]	Temperature [°C]	Specific volume of water [cm^3/g]	Dynamic viscosity [10^{-4} Pa s]
100	0.6	145	1.1	1.9
150	1.0	150	1.1	1.8
250	2.0	180	1.1	1.5
350	2.5	190	1.1	1.4
450	3.4	203	1.2	1.3
550	4.0	220	1.2	1.2
650	5.0	230	1.2	1.2
780	6.0	240	1.2	1.1
900	7.0	250	1.2	1.1
1000	7.5	260	1.3	1.0
1100	8.5	258	1.3	1.0
1150	8.6	260	1.3	1.0
1250	9.5	232	1.2	1.2
1350	11	225	1.2	1.2
1550	12	290	1.3	0.9
1620	13	270	1.3	1.0
1800	14	320	1.5	0.8
1850	15	290	1.3	0.9
2000	16	310	1.4	0.9
2200	17	340	1.6	0.7
2350	19	350	1.7	0.7
2550	20	360	1.8	0.6
2900	23	370	2.0	0.6
3100	24	380	2.6	0.5
3150	25	400	5.1	0.3
3350	26	450	6.2	0.3
3500	27	510	7.1	0.3

Table 5-3 Amount of Si concentration change in the upward-fluid.

Depth [m]	Quartz solubility, Si [mg/kg(H_2O)]	Ω_{Qtz} [1]	Log_{10} Permeability, μ [m^2]							
			-9	-10	-11	-12	-13	-14	-15	-16
			dC_{Si} [mg/kg(H_2O)]							
0	0	-	-	-	-	-	-	-	-	-
100	54	1.1	0	0	0	-1	-4	-4	-4	-4
150	58	1.5	0	0	-2	-13	-29	-29	-29	-29
250	88	1.1	0	0	-3	-11	-12	-12	-12	-12
350	99	1.2	0	0	-3	-14	-17	-17	-17	-17
450	116	1.2	0	-1	-7	-24	-24	-24	-24	-24
550	141	1.1	0	-1	-4	-15	-16	-16	-16	-16
650	157	1.1	0	-1	-8	-17	-17	-17	-17	-17
780	174	1.1	0	-1	-9	-18	-18	-18	-18	-18
900	192	1.1	0	-2	-13	-19	-19	-19	-19	-19
1000	210	1.0	0	0	1	3	3	3	3	3
1100	207	1.0	0	-1	-3	-4	-4	-4	-4	-4
1150	211	0.8	0	4	27	49	49	49	49	49
1250	162	0.9	0	0	4	11	11	11	11	11
1350	151	1.8	-1	-11	-74	-121	-121	-121	-121	-121
1550	272	0.9	0	4	27	38	38	38	38	38
1620	234	1.4	-2	-16	-77	-91	-91	-91	-91	-91
1800	325	0.9	0	5	31	48	48	48	48	48
1850	276	1.1	-1	-10	-37	-39	-39	-39	-39	-39
2000	315	1.1	-1	-12	-31	-31	-31	-31	-31	-31
2200	347	1.0	0	0	1	1	1	1	1	1
2350	345	0.9	2	11	18	18	18	18	18	18
2550	327	0.9	4	21	24	24	24	24	24	24
2900	303	0.6	12	75	108	108	108	108	108	108
3100	195	0.2	2	19	112	152	152	152	152	152
3150	43	0.8	3	10	10	10	10	10	10	10
3350	33	1.1	-5	-5	-5	-5	-5	-5	-5	-5
3500	38	1.5	-17	-17	-17	-17	-17	-17	-17	-17
3790	55	-	-	-	-	-	-	-	-	-

[1] Si saturation ratio with respect to quartz.

Table 5-4 Amount of Si concentration change in the downward-fluid.

Depth [m]	Quartz solubility, Si [mg/kg(H_2O)]	Ω_{Qtz} [1]	Log_{10} Permeability, μ [m^2]							
			-9	-10	-11	-12	-13	-14	-15	-16
			dC_{Si} [mg/kg(H_2O)]							
0	0	-	-	-	-	-	-	-	-	-
100	54	0.0	0	0	2	14	52	54	54	54
150	58	0.9	0	0	0	2	4	4	4	4
250	88	0.7	0	1	7	27	29	29	29	29
350	99	0.9	0	0	2	10	12	12	12	12
450	116	0.9	0	1	5	16	17	17	17	17
550	141	0.8	0	1	7	23	24	24	24	24
650	157	0.9	0	1	8	16	16	16	16	16
780	174	0.9	0	1	9	17	17	17	17	17
900	192	0.9	0	2	13	18	18	18	18	18
1000	210	0.9	0	1	10	19	19	19	19	19
1100	207	1.0	0	0	-2	-3	-3	-3	-3	-3
1150	211	1.0	0	0	2	4	4	4	4	4
1250	162	1.3	0	-2	-17	-48	-49	-49	-49	-49
1350	151	1.1	0	-1	-7	-11	-11	-11	-11	-11
1550	272	0.6	1	14	86	121	121	121	121	121
1620	234	1.2	-1	-7	-33	-38	-38	-38	-38	-38
1800	325	0.7	1	9	59	91	91	91	91	91
1850	276	1.2	-1	-12	-46	-48	-48	-48	-48	-48
2000	315	0.9	2	15	39	39	39	39	39	39
2200	347	0.9	1	11	31	31	31	31	31	31
2350	345	1.0	0	-1	-1	-1	-1	-1	-1	-1
2550	327	1.1	-3	-16	-18	-18	-18	-18	-18	-18
2900	303	1.1	-24	-24	-24	-24	-24	-24	-24	-24
3100	195	1.6	-68	-108	-108	-108	-108	-108	-108	-108
3150	43	4.6	-152	-152	-152	-152	-152	-152	-152	-152
3350	33	1.3	-10	-10	-10	-10	-10	-10	-10	-10
3500	38	0.9	4	5	5	5	5	5	5	5
3790	55	-	-	-	-	-	-	-	-	-

[1] Si saturation ratio with respect to quartz.

(a)

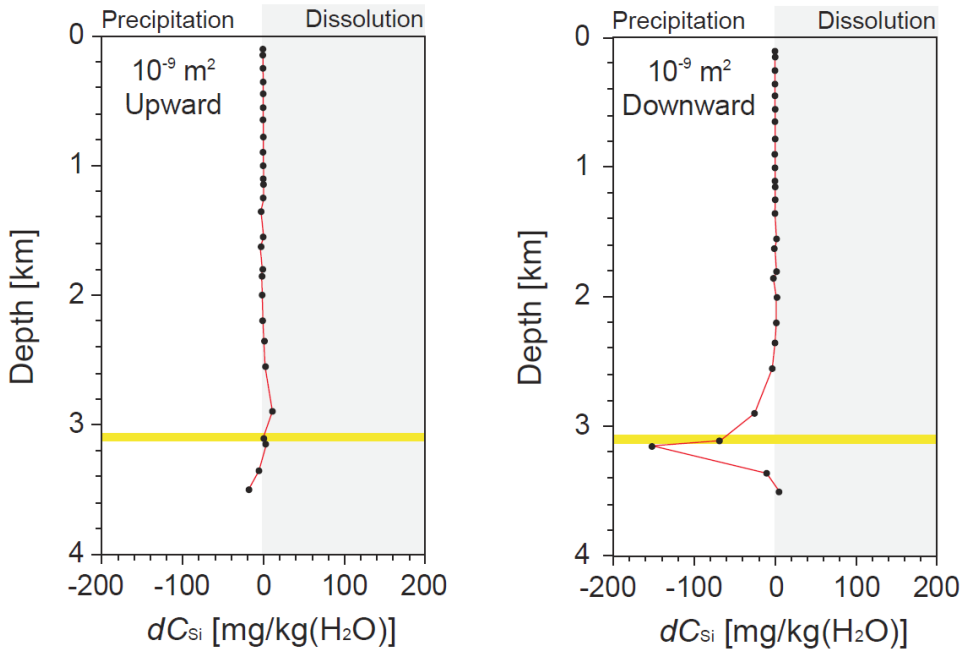
Precipitation
Dissolution
10-9 m2
Upward
Depth [km]
0
1
2
3
4
-200
-100
0
100
200
dCSi [mg/kg(H2O)]
Precipitation
Dissolution
10-9 m2
Downward
Depth [km]
dCSi [mg/kg(H2O)]

(b)

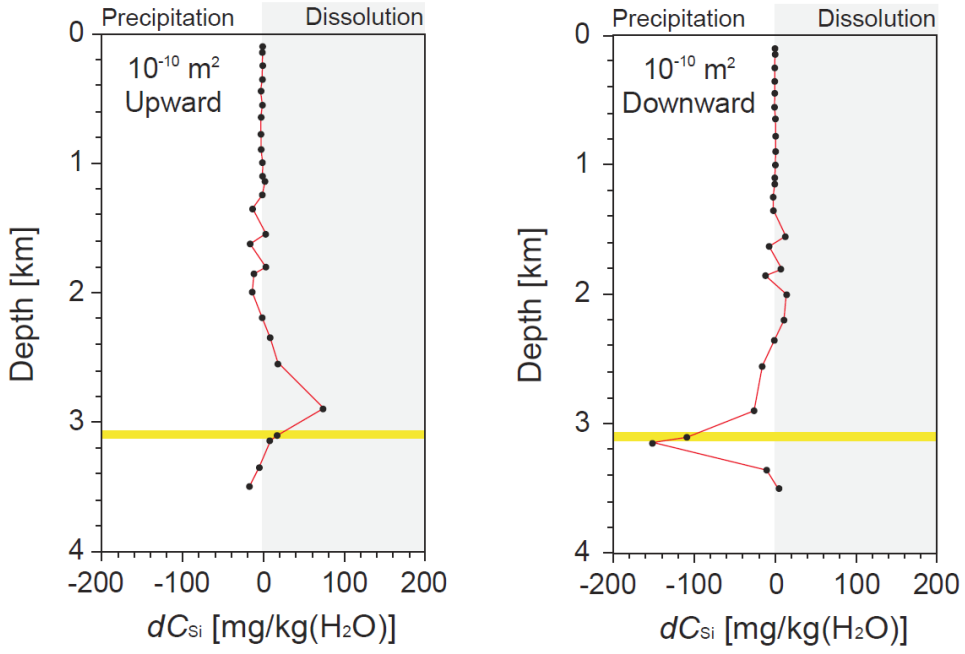
Precipitation
Dissolution
10-10 m2
Upward
Depth [km]
0
1
2
3
4
-200
-100
0
100
200
dCSi [mg/kg(H2O)]
Precipitation
Dissolution
10-10 m2
Downward
Depth [km]
dCSi [mg/kg(H2O)]

Figure 5-5

(c)

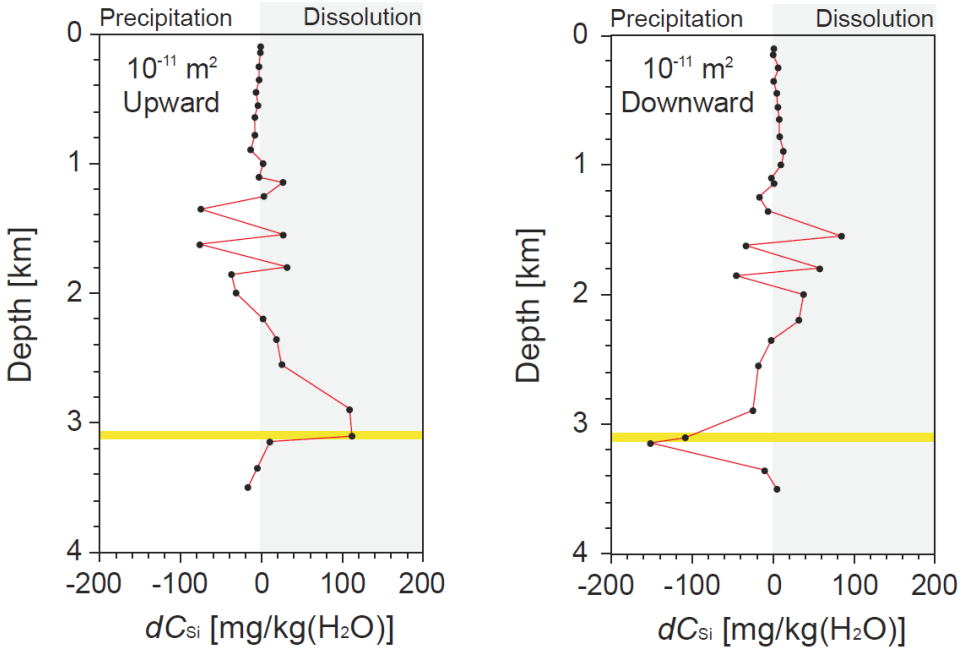
Precipitation
Dissolution
10-11 m2
Upward
Depth [km]
dCSi [mg/kg(H2O)]
Precipitation
Dissolution
10-11 m2
Downward
Depth [km]
dCSi [mg/kg(H2O)]

(d)

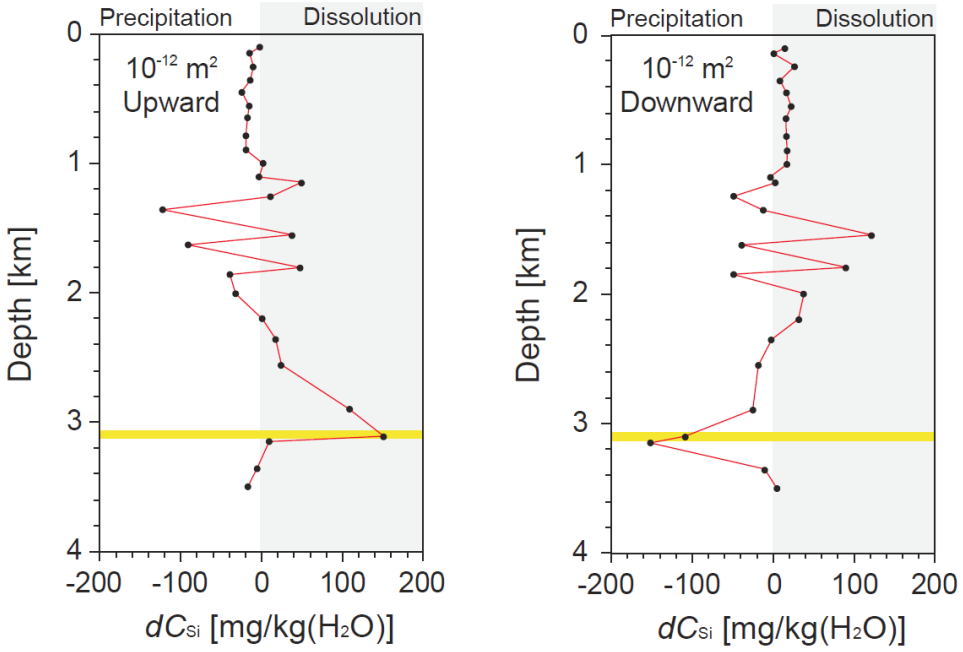
Precipitation
Dissolution
10-12 m2
Upward
Depth [km]
dCSi [mg/kg(H2O)]
Precipitation
Dissolution
10-12 m2
Downward
Depth [km]
dCSi [mg/kg(H2O)]

Figure 5-5

(e)

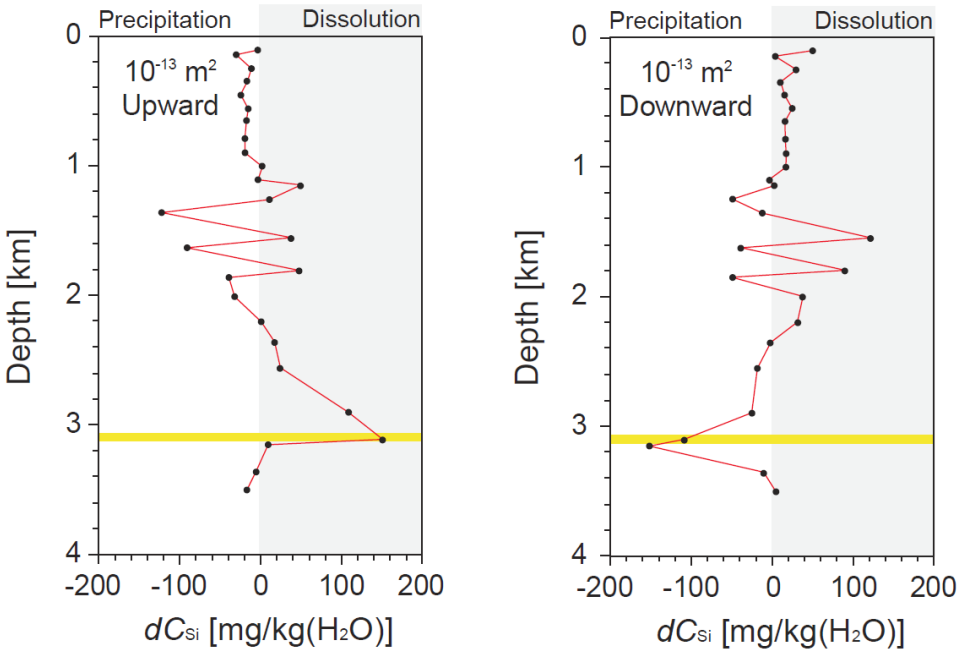
Precipitation
Dissolution
10-13 m2
Upward
Depth [km]
dCSi [mg/kg(H2O)]
Precipitation
Dissolution
10-13 m2
Downward
Depth [km]
dCSi [mg/kg(H2O)]

(f)

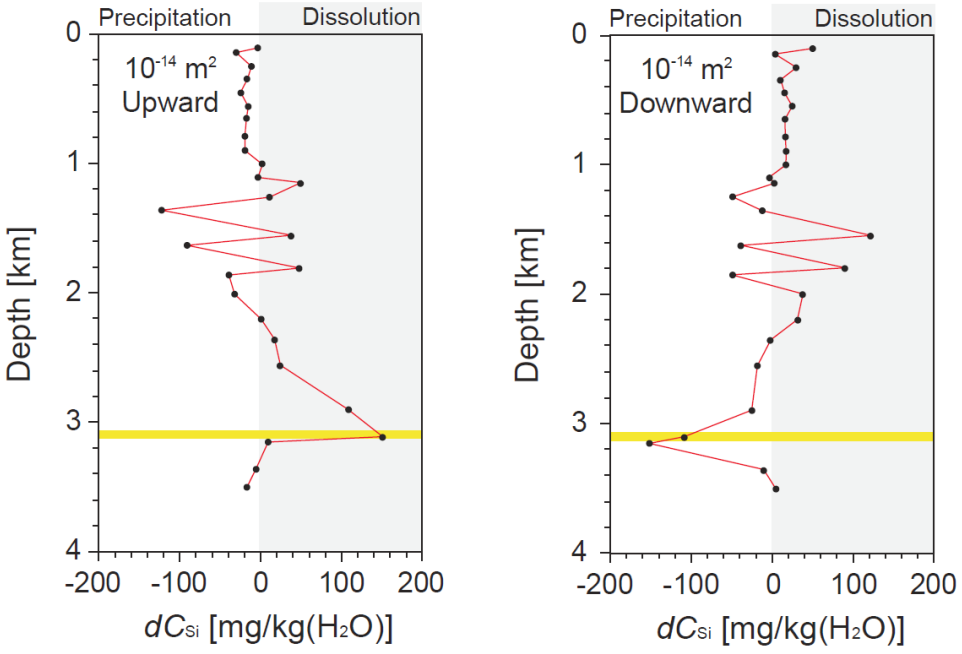
Precipitation
Dissolution
10-14 m2
Upward
Depth [km]
dCSi [mg/kg(H2O)]
Precipitation
Dissolution
10-14 m2
Downward
Depth [km]
dCSi [mg/kg(H2O)]

Figure 5-5

Figure 5-5 Amount of change of Si concentration in the fluid, dC_{Si} mg/kg(H_2O), at the fracture permeability, μ, of (a) 1×10^{-9} m^2, (b) 1×10^{-10} m^2, (c) 1×10^{-11} m^2, (d) 1×10^{-12} m^2, (e) 1×10^{-13} m^2, and (f) 1×10^{-14} m^2. The direction of fluid is upward (left) and downward (right). Positive and negative values of dC_{Si} indicate dissolution (grey zone) and precipitation (white zone) of silica minerals, respectively. The permeable-impermeable boundary in the well WD-1a of the Kakkonda geothermal field is at 3100 m depth (yellow line).

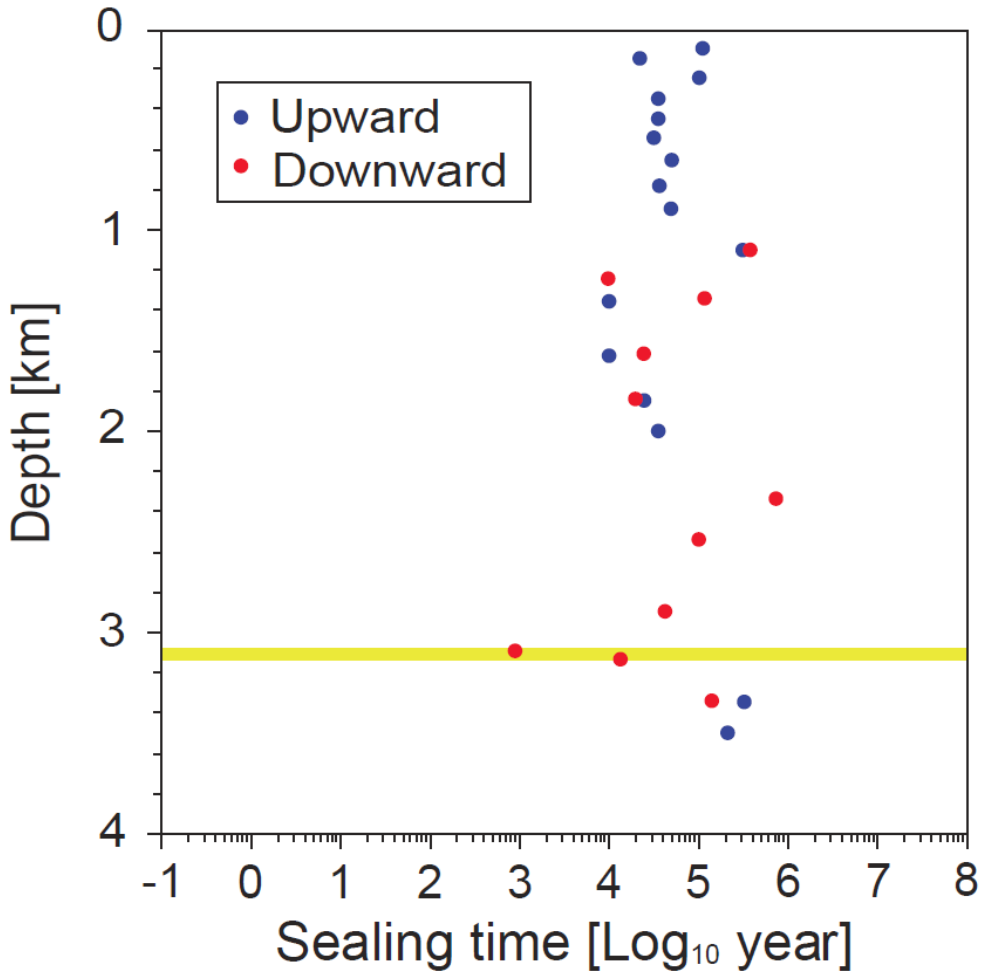

Figure 5-6 Sealing time of a parallel fracture at the fracture permeability of 1×10^{-13} m^2. Silica precipitation occurs in the upward- (blue) and the downward- (red) fluids. The permeable-impermeable boundary in the well WD-1a of the Kakkonda geothermal field is at 3100 m depth (yellow line).

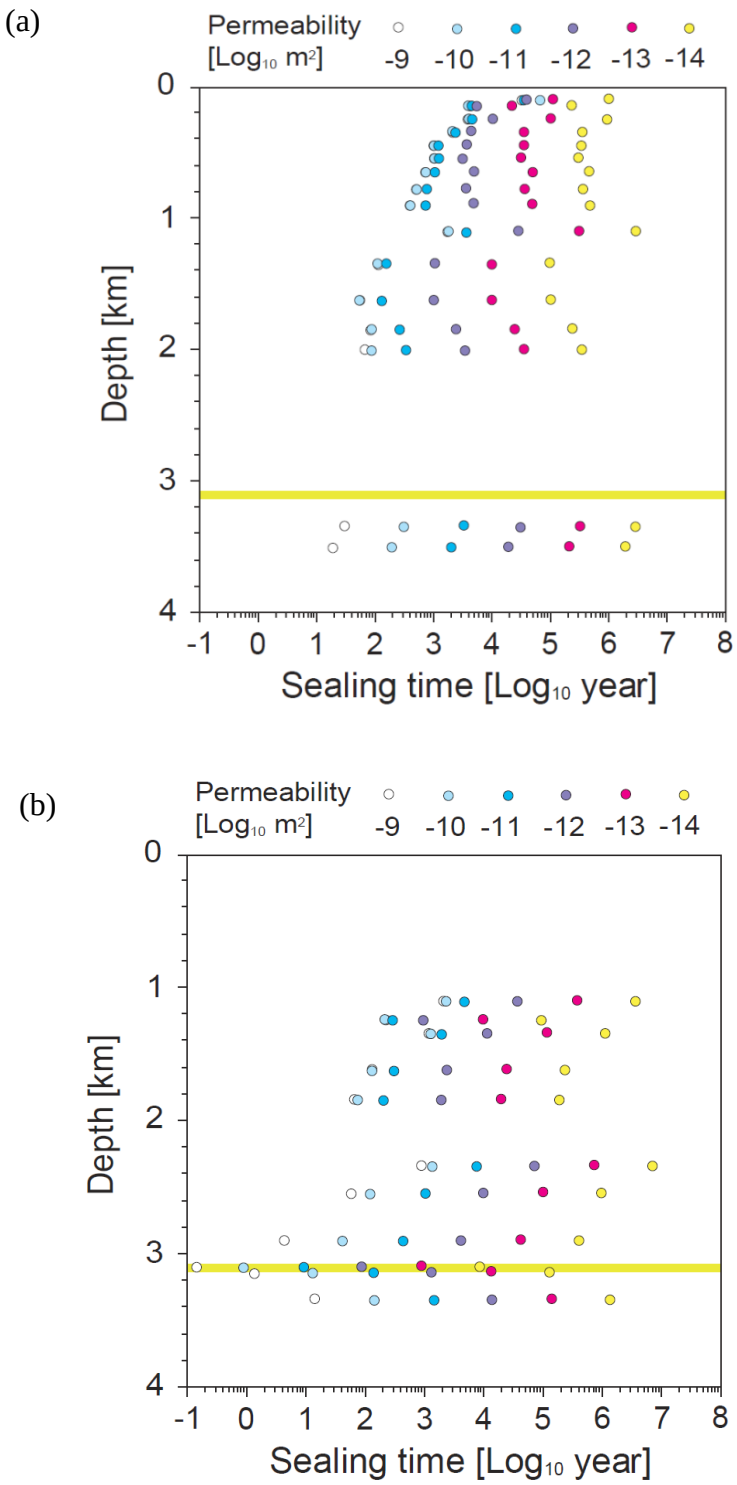

Figure 5-7 Sealing time of a parallel fracture by silica precipitation at the fracture permeability from 1×10^{-9} to 1×10^{-14} m^2. Silica precipitation occurs in (a) the upward- and (b) the downward-fluids. The permeable-impermeable boundary in the well WD-1a of the Kakkonda geothermal field is at 3100 m depth (yellow line).

5.5. Discussion

5.5.1. Variation of Si concentration in the Kakkonda geothermal fluid

At the depth from 1 to 2 km, relative large amount of dissolution or precipitation occurs in liquid phase (Fig. 5-5) is caused by the fluctuation of temperature in the well WD-1a (Ikeuchi *et al*., 1998; Fig 4-10a). The local minimum values of quartz solubility at 1100, 1350, and 1850 m depth (Table 5-3, 5-4; Fig. 4-10b) may introduce the relatively rapid silica dissolution and precipitation by surface reaction at the shallower depth, which could cause the local permeable and impermeable zones at shallower depth. At the Kakkonda geothermal field, the lower limits of the lost circulations in the well-21 and the well WD-1a were at the shallower part of the Kakkonda granite, 1214 m and 2137 m depth, respectively (Doi *et al*., 1995, 1998; Muraoka *et al*., 1998). In the upward-fluid, the depth of the fastest dissolution of quartz is 2900 m depth, which is above the permeable-impermeable boundary, and it shifts to 3100 m with decrease of permeability from 1×10^{-10} m^2 to 1×10^{-11} m^2 (Table 5-3; Fig. 5-5b, c) reflecting the enough time for fluid to be saturated with quartz with decrease of permeability. The productive fractures have been expected at the margin of the Kakkonda granite because the complete lost circulations occurred at 2344 m and 2550 m depth in the well-13 and the well-19, respectively (Kato *et al*., 1993).

At around the permeable-impermeable boundary (3100 m depth), fastest precipitation occurs at 3150 m depth. In the supercritical conditions of water under 2900 m depth, silica precipitation via nucleation occurs regardless of the quartz surfaces. The fracture sealing could be controlled by nucleation process of silica minerals, whereas quartz overgrowth would less effective. At the permeable-impermeable boundary, the mixture of the upward- and the downward-fluids may be easier than that at shallower part because the boundary has a role as a bottom of the hydrothermal convection zone where meteoric water circulates. Due to upward increase of quartz solubility, quartz dissolution also occurs in the upward-fluid above the permeable-impermeable boundary (2900–3100 m depth; Fig. 5-5). Based on the plot of amount of Si concentration change in the solution in this study (Fig. 5-5), permeability increases due to dissolution of quartz above the permeable-impermeable boundary (2900–3100 m depth), whereas precipitation of silica minerals causes decrease of permeability and sealing of fracture under the boundary at 3150 m depth. The drastic change of reaction from dissolution to precipitation could occur in the area of 250 m, indicating the fluctuation of reactions between dissolution and precipitation might be occur with mixture of the dominant direction of fluid flows.

5.5.2. Ages of the Kakkonda geothermal field and adjacent areas

Ages of the Kakkonda geothermal field and adjustcent areas were observed in previous studies. The K-Ar ages of minerals of the Kakkonda granite ranges from 0.7 to under 0.1 Ma (Koshiya *et al*., 1993; Kanisawa *et al*., 1994; Doi *et al*., 1998; Ehara *et al*., 2001). In addition, Fission track ages and the K-Ar ages of Tamagawa welded tuff were determined from 1.2 ± 0.3 Ma to 2.5 ± 0.6 Ma (Tamanyu and Suto, 1978) and from 1.77 to 1.93 Ma (Tamanyu and Lanphere, 1983), and that of Kashinai formation were interpreted 0.09–1.77 Ma (Tamanyu and Lanphere, 1983), respectively. Based on these previous studies, the ages of the Kakkonda geothermal field could be suspected roughly ~1 Ma for the formations of the Kakkonda granite and less than 0.1 Ma for that of the fracture system.

Calculation of this chapter shows that timescale for fracture sealing depends on the fracture permeability (Fig. 5-5, 5-7). At the shallower part of <2000 m depth, where the hydrothermal quartz vein could form via quartz growth on quartz surfaces, the relative short times for fracture sealing are expected between 1000 m and 2000 m depth (Fig. 5-7). In the condition of the fracture permeability of 1×10^{-13} m^2, for example, the times for fracture sealing at 1850 m depth are 10296 and 9972 years at 1350 and 1680 m depth, respectively, in the upward-fluid, and that is 18792 years in the downward-fluid

(Fig. 5-6), which is correlated with 0.2 ± 0.1 Ma of the K-Ar ages of K-feldspars in the hydrothermal veins of the Kakkonda geothermal field (Koshiya *et al*., 1993).

The timescale of fracture sealing decreases with increasing of the fracture permeability. Even in liquid phase of 1680 m depth, fracture could be sealed by precipitates of silica minerals for 53 years in the upward-fluid at the fracture permeability of 1×10^{-9} m^2 (Fig. 5-7a). However, the actual time for fracture sealing is expected to be much longer than 53 years because permeability decreases with increasing of amount of precipitates. In addition, surface reaction of quartz precipitation via growth could occur only on quartz surfaces in host rocks (e.g., 30 % in granite) at the shallower part in liquid phase. The effective surface area for quartz growth may decrease and the reaction rate may become smaller because quartz growth is dominant in the direction of c-axis (Okamoto and Sekine, 2011).

At deeper part of around the permeable-impermeable boundary, a fracture at 3100 m depth could be sealed in the downward-fluid for 896 years in the fracture permeability of 1×10^{-13} m^2 (Fig. 5-7b). This timescale of fracture sealing is from one to several hundred times faster than that at shallower part of liquid phase (0.1–0.2 Ma) because of nucleation of silica minerals. The time difference of fracture sealing between at the shallow part and at the permeable-impermeable boundary may be much larger

than two orders because fracture sealing at the shallower part depends on the quartz surfaces and may be longer than that estimated by using the kinetic equation of the overall silica-water reaction (Eq. 33), whereas nucleation of silica mineral is regardless of the surface area of quartz. Therefore, fracture sealing at the permeable-impermeable boundary are regarded to be occurred by the largest and fastest silica precipitation in the earth's crust in equilibrium and kinetic considerations. The division of the permeable and the impermeable areas might occur in the initial time of formation of the Kakkonda geothermal field, when the hydrothermal veins at shallower part would still not be formed.

Thermal structure of the Kakkonda geothermal field has changed since the intrusion of the Kakkonda granite occurred. Because the quartz solubility and reaction rate of silica-water interaction are written as the function of temperature, the solubility and reaction rate constants of silica minerals are affected by the thermal history of temperature. At the moment of the intrusion of the Kakkonda granite, the permeable-impermeable boundary has been shallower than 3100 m depth because temperature at that time was higher than its present value. Therefore, the depth of the permeable-impermeable boundary may have moved down with cooling of the Kakkonda geothermal field. The brittle-ductile transition of the field of the typical

geothermal gradient (30 °C/km) has been considered to range from 10 to 20 km depth, which is deeper than that in the Kakkonda geothermal field of ~100 °C/km geothermal gradient. In the case that the brittle-ductile transition is correlated with the permeable-impermeable boundary, the deeper boundary at the field of the typical geothermal gradient may be a result of cooling of the field and moving down of the permeable-impermeable boundary.

5.5.2.1. The geochemical evolution of the Kakkonda geothermal field

In this study, the geochemical evolution of the Kakkonda geothermal field was discussed in equilibrium and kinetic theories in the chapter 4 and this chapter, respectively. Figure 5-8 shows the summarized model of the geochemical evolution of the Kakkonda geothermal field. At the permeable zone, dissolution and precipitation of quartz occurs in the downward- and the upward-fluids, respectively. Dominant reaction of precipitation in the permeable zone is quartz growth on quartz surfaces, which is related with the hydrothermal quartz vein at shallower depth. Nucleation of silica minerals is difficult to occur in fractures of crustal rocks because of low temperature and low Si saturated fluid, which reflects the gradual change of quartz solubility (Fig. 4-10b). At the deep reservoir, dissolution of silica minerals is a dominant reaction

because of the local maximum of the quartz solubility (Fig. 4-10b). Large amount of Si dissolution may cause the formation of the open fracture zone filled with fluid, which is observed as the reflectors at 2–3 km depth (Matsushima *et al.*, 2003). At the permeable-impermeable boundary, significant large and rapid precipitation of silica minerals via growth and nucleation could occur in the downward-fluid. The local impermeable area, which divides the shallow permeable zone and the deep impermeable zone, could be formed by precipitation of silica minerals via nucleation. In the upward-fluid, dissolution rate of quartz is relatively higher than that at shallower part. Because the permeable-impermeable boundary is the bottom of the hydrothermal convection zone, the direction of fluid may fluctuate between up and down. However, the reaction rate of precipitation in the supercritical conditions of water is almost ten times larger than that of dissolution (Table 5-1; Fig. 5-4b). Therefore, if open fractures forms mechanically or via dissolution of quartz at the depth of the permeable-impermeable boundary, the impermeable zone could be reproduced by precipitation of silica minerals, which cause the sustainable division between the permeable zone and the impermeable zone in the Earth's crust.

On the ground surface, amorphous silica has been observed as silica sinter and scale. The application of the empirical kinetic equation in this study for precipitation of

amorphous silica at below 100 °C is unclear because of the experimental condition was high temperature and pressure, and in supercritical conditions of water. However, Al has been recognized as one of the important components to affect to the silica solubility and silica-water interaction (Iler, 1973; Yokoyama *et al*., 1993; Carroll *et al*., 1998; Nishida *et al*., 2009; Miyoshi, 2005; Jordan, 2009). At 180 °C, silica precipitation occurs even though the silica concentration of the water is near or below the amorphous silica solubility perhaps because of impurity in the solution dissolved from a gold reaction vessel (Fe, Ni) (Rothbaum and Rohde, 1979). On the other hand, silica scale of the geothermal plant is also formed by boiling of water, which causes the high Si supersaturated fluid during the rapid fluid upward along the pipeline of the production well. In the injection well of the geothermal plant, there is a problem of decrease of the amount of the injection water probably related to fracture sealing at around the bottom of the well. Because the experimental apparatus constructed of SUS tube in this study is similar to the pipeline of the geothermal plants, and temperatures in the production and the injection wells are higher than that in the pipelines of the ground equipment, I hope to develop empirically the kinetic equation for silica precipitation in all phase of water (liquid, vapour, and the supercritical conditions of water) as a function of minor components in the solution in the future works.

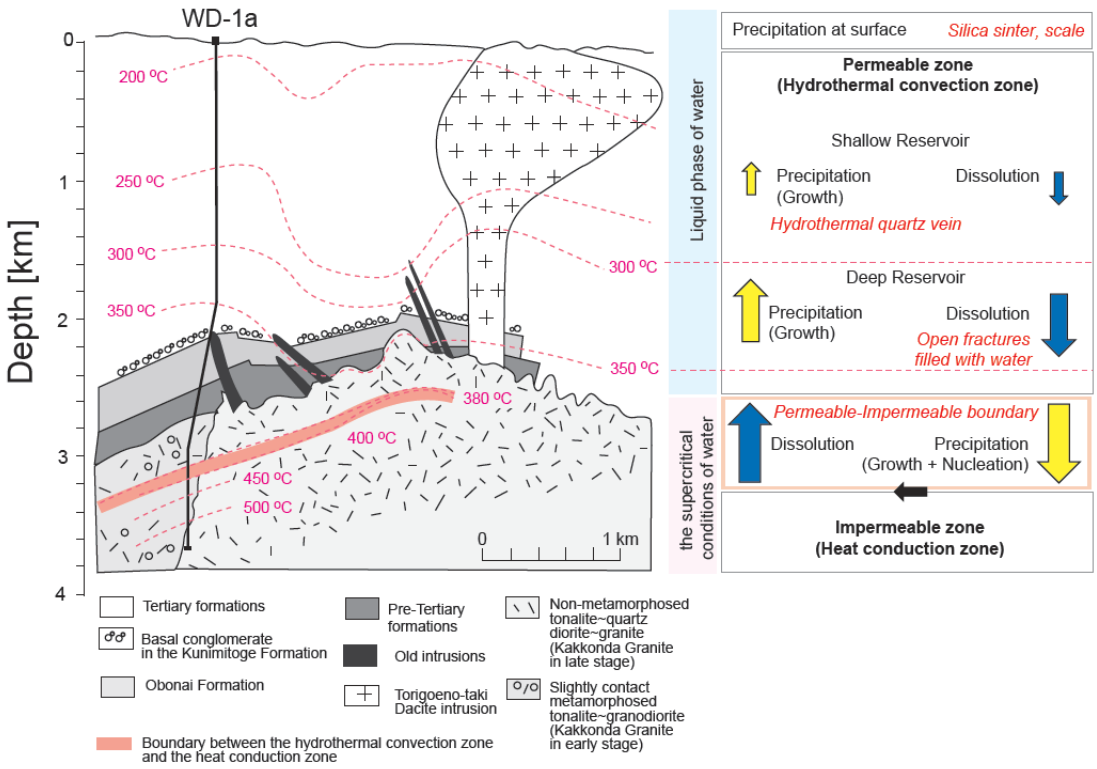

Figure 5-8 Schematic image of the geochemical evolution of the Kakkonda geothermal field. Schematic cross-section of the Kakkonda geothermal system is modified after Doi *et al*. (1998) (Fig. 4-1b). The permeable zone is in liquid phase of water (blue zone). The permeable-impermeable boundary and the impermeable zone are in the supercritical conditions of water (red zone). The direction and size of arrows indicate the direction of fluid flow (upward and downward) and the reaction rate, respectively. Silica-water interaction is dissolution (blue arrows) and precipitation (yellow arrows). The characteristic conditions related to silica-water interaction in the Earth's crust are shown in italic red words.

5.6. Conclusions

The conditions of fluid and silica deposits in the Kakkonda geothermal field were revealed by equilibrium calculation and analysis of natural samples. The concentrations of Al and Si in the fluid of the Kakkonda geothermal field distribute below the equilibrium curve of albite-H_2O, which was estimated by using the program SOLVEQ-XPT (Reed *et al.*, 2010). Simulation of dissolution and precipitation of silica minerals along the well WD-1a of the Kakkonda geothermal field was conducted by using the kinetic equation determined in the chapter 4 (Eq. 32). Amount of dissolution and precipitation of silica minerals increases and the fluid is saturated with decreasing of the fracture permeability from 1×10^{-9} to 1×10^{-13} m^2. The largest amount of silica precipitation occurs in the downward-fluid at 3150 m depth regardless of the permeability. At the shallower part, the time for fracture sealing at the fracture permeability of 1×10^{-13} m^2 correlates with the previous observations of the Kakkonda geothermal field, whereas that at the permeable-impermeable boundary is several hundred times larger than the estimations in the previous works, indicating that the division of the permeable and impermeable area might occur in the initial age of formation of the Kakkonda geothermal field.

6. CONCLUSIONS

Silica is one of the dominant constituents of the Earth's crust, and its dissolution-precipitation behavior has a marked effect on the crust's hydrological and mechanical properties. However, the mechanism of silica precipitation and the role of silica-water interaction on the conditions of the Earth's crust have been unclear. Based on the hydrothermal experiments of silica precipitation, this study revealed that the geochemical evolution of the hydrological properties, especially the permeable-impermeable boundary, of the Earth's crust could be controlled by dissolution and precipitation of silica minerals.

<Chapter 2>

- Large amount of precipitation of silica minerals occurred via nucleation only in the supercritical region of water.
- The hockey-like trend of the temperature dependence of silica precipitation is explained by the homogeneous nucleation of quartz in the surface energy of quartz, σ = 130 mJ/m^2, which is similar to the value in the previous study (Hiraga *et al.*, 2002)

- The relation of Si and Al concentrations in the solution made by dissolution of albite and quartz is controlled by the equilibrium of albite-H_2O system.
- With increasing of Al concentration in the input solutions, $C_{Al,in}$, the dominant precipitated products changes from amorphous silica ($C_{Al,in}$ <1 mg/kg(H_2O)), to cristobalite ($C_{Al,in}$ = ~3 mg/kg(H_2O)), quartz ($C_{Al,in}$ = ~7 mg/kg(H_2O)), and albite and analcite ($C_{Al,in}$ >10 mg/kg(H_2O)).
- Amount of overall precipitated products increases with increasing of Al concentration in the input solutions, $C_{Al,in}$, from 0 to 7 mg/kg(H_2O), whereas the amount of the products of $C_{Al,in}$ >10 mg/kg(H_2O) is lower than that of $C_{Al,in}$ <10 mg/kg(H_2O).
- The solution analyses revealed that differences of Al and Na concentrations between the input and output solutions were almost one-on-one. EPMA analysis showed that a positive correlation of Al and Na contents in quartz, which precipitated from the solutions of Al concentration of 3–7 mg/kg(H_2O). These characters of solutions and products suggests that the presence of Al^{3+} and Na^{+} in solution reduces the energetic barrier of quartz nucleation, and Al is incorporated into quartz mainly by the substitution $Si^{4+} = Al^{3+} + Na^{+}$.

- Equilibrium calculation showed the possibility of precipitation of albite and analcite in the solution of high Al concentration >10 mg/kg(H_2O) made by dissolution of quartz and albite.

<Chapter 3>

- A new kinetic equation of overall silica-water reactions was proposed. The first term for surface reaction following the previous equation (Rimstidt and Barnes, 1980) and the second term for nucleation.
- Reaction rate order, *n*, of nucleation controlled precipitation was determined as 1 by using integral methods in the precipitation experiment of flow rate (residence time).
- The nucleation parameter α, which relates with the applicability of nucleation of silica minerals, was introduced; the value is 1 in the conditions of the supersaturated solution respect to quartz and supercritical of water, whereas it is zero in other conditions.
- The nucleation rate constant, k_N, of nucleation controlled precipitation was derived as a function of Al concentration in the input solution based on the experimental results of minor components (chapter 2).

- The kinetic equation of overall silica-water reactions simulated well the Si concentrations in the output solutions in the experiments of minor components without rock/mineral substrates.

<Chapter 4>

- The quartz solubility has a local minimum at the permeable-impermeable boundary of the Kakkonda geothermal field at 3100 m depth and in the supercritical conditions of water (380 °C, 24 MPa), which was observed in the well WD-1a (Doi et al., 1998). This trend of quartz solubility is possible in the conditions of fluid pressure ranged from hydrostatic to lithostatic and that of salinity up to 10 wt%.
- Based on the results of hydrothermal experiments of temperature dependence (chapter 2), rapid quartz precipitation is considered to occur via nucleation when fluid flows downward and H_2O state changes from the liquid phase to the supercritical conditions of water.
- The local maximum of quartz solubility at around 2000–3000 m depth of the Kakkonda geothermal field may indicate that the preservation of open fractures at the margin of the Kakkonda granite is controlled by dissolution of quartz.

- The permeable-impermeable boundary of the Kakkonda geothermal field could be formed by large amount of quartz precipitation via nucleation, which occurs at the depth of the local minimum of quartz solubility and in the supercritical conditions of water.
- The preferential precipitation of quartz at a specific depth of geothermal fields has a significant role in forming and sustaining the permeable-impermeable boundary within the Earth's crust.

<Chapter 5>

- Chemical compositions of fluid and silica deposits in the Kakkonda geothermal field are similar to that of experiments in this study.
- The fastest precipitation of silica minerals via quartz growth and nucleation could occur at the permeable-impermeable boundary of the Kakkonda geothermal field in the downward-fluid by using the new kinetic equation determined in the chapter 3.
- Time to seal a fracture at the fracture permeability of 1×10^{-13} m^2 under 1 Ma correlates with the estimations of formation ages of the Kakkonda geothermal field by observations of natural samples of the Kakkonda and surrounding areas.

- The rate of fracture sealing at the permeable-impermeable boundary is several hundred times faster than that at shallower part in the same condition of the fracture permeability, indicating that the division of the permeable and the impermeable areas might occur at the initial time of formation of the Kakkonda geothermal field.
- The equilibrium and kinetic considerations in this study indicates that, if open fractures forms mechanically or via dissolution of quartz at the depth of the permeable-impermeable boundary, the impermeable zone could be reproduced by precipitation of silica minerals, which cause the sustainable division between the permeable zone and the impermeable zone in the Earth's crust.

ACKNOWLEDGEMENTS

I would like to show my greatest appreciation to Professor Noriyoshi Tsuchiya of Graduate School of Environmental Studies, Tohoku University, for giving me invaluable suggestions, opportunities, and warm encouragement.

I am indebted to Professor Chihiro Inoue and Professor Takeshi Komai of Graduate School of Environmental Studies, Tohoku University, for valuable discussions and advice in the course of completing this thesis for Ph.D. degree.

I am deeply grateful to Associate Professor Atsushi Okamoto of Graduate School of Environmental Studies, Tohoku University, for frequent discussions, insightful coaching, and warm encouragement.

I would like to show appreciation from my heart to Professor Mark H. Reed of Department of Geological Sciences, University of Oregon. His constructive comments and the programs (SOLVEQ-XPT and CHIM) have been helpful for my research. I would also like to express my gratitude to Karen, his wife. Without Mark and Karen's sweet supports of my stay in Oregon, my study in University of Oregon could not have been possible.

I would like to thank Associate Professor Nobuo Hirano of Graduate School of Environmental Studies, Tohoku University, for giving me the opportunity to belong Tsuchiya laboratory, kind coaching, and helpful technical and methodological knowledge.

I appreciate Associate Professor Masanobu Kamitakahara of Graduate School of Environmental Studies, Tohoku University, for insightful suggestions.

I appreciate the generous support of analytical knowledge and my life in the laboratory from Assistant Professor Takahiro Watanabe of Graduate School of Environmental Studies, Tohoku University.

I am grateful to Assistant Professor Noriaki Watanabe of Graduate School of Environmental Studies, Tohoku University, for constructive comments on my research and kind support of experiments and conferences.

Thoughtful comments and invaluable fieldwork experiments were given by Research Fellow Ryoichi Yamada of Graduate School of Environmental Studies, Tohoku University. I would like to express my gratitude.

My heartfelt appreciation goes to Research Fellow Shinichi Yamasaki of Graduate School of Environmental Studies, Tohoku University, for invaluable suggestions and support for analyses.

I really thank for useful support for analysis and comment for research by Assistant Professor Fumiko Watanabe Nara of Graduate School of Environmental Studies, Tohoku University.

Assistant Professor Tatsu Kuwatani of Graduate School of Environmental Studies, Tohoku University, gives me valuable comments and assistance with EPMA analyses. I would like to offer my special thanks.

I would like to express my gratitude to Professor Michihiko Nakamura of Department of Earth Science, Tohoku University, for constructive comments and warm supports.

I thank Assistant Professor Satoshi Okumura and Assistant Professor Jun Muto of Department of Earth Science, Tohoku University, for technical supports and intellectual discussions. I also appreciate Jun-ichi Fukuda of Department of Earth Science, Tohoku University, for meticulous supports.

I would like to show my appreciation to Professor Eiichi Takahashi of Department of Earth and Planetary Sciences, Graduate School of Science and Engineering, for invaluable discussions and kind encouragements.

I would like to offer my special thanks to Associate Professor Akihisa Kizaki of Akita University, for tolerant supports of my life in the laboratory.

I am grateful to Associate Professor Yoshihiro Ito of Research Center for Earthquake Prediction (RCEP), Disaster Prevention Research Institute Kyoto University, for useful comments and discussions.

I thank Research Associate James Palandri of Department of Geological Sciences, University of Oregon, for enormous contribution to study the program SOLVEQ-XPT and CHIM. I would also like to express my gratitude to John J. Donovan and Julie Chouinard of Department of Geological Sciences, University of Oregon, and Adam J.R. Kent of Department of Geosciences, Oregon State University, for kindly supports of analysis and observations.

I have had the encouragement of Kasumi Yasukawa, Keiichi Sakaguchi, and Hiroshi Asanuma of Renewable Energy Research Center, National Institute of Advanced Industrial Science and Technology (AIST). I am deeply grateful to them.

I would like to thank Norio Yanagisawa of Institute for Geo-Resources and Environment, National Institute of Advanced Industrial Science and Technology (AIST), for giving valuable suggestions and offering the report of Kakkonda deep drilling project.

I appreciate Toshiyuki Tosha of Geothermal Resource Development Department, Japan Oil, Gas and Metals National Corporation (JOGMEC), for kindly providing the seismic data of the Kakkonda geothermal field.

I would like to offer my special thanks to Yumiko Harigane of Institute of Geology and Geoinformation, National Institute of Advanced Industrial Science and Technology (AIST), for kindly support in conferences.

Osamu Kato, Tohoku Hydropower and Geothermal Energy Co., Inc. (TOHGEC), offered the valuable samples of silica scale and drilling core of the Kakkonda geothermal plant. He has also given me useful comments. I am grateful to him.

I am also grateful to Isao Hino, Kenko-sha, for making beautiful thin sections.

This study was supported by a Grant-in-Aid for Scientific Research (No. 22109501) from the Ministry of Education, Culture, Sports, Science and Technology of Japan, awarded to A. Okamoto, and by a Grant-in-Aid for Young Scientists (No. 4630) from the Japan Society for the Promotion of Science, awarded to H. Saishu.

This study was also supported by Tohoku University Global COE Program “Global Education and Research Center for Earth and Planetary Dynamics” to join the international conference and to study in University of Oregon, U.S.A.

Tohoku University Environmental Leader Program, Strategic Energy and Resource Management and Sustainable Solutions (SERMSS), was also helpful for this study.

I would like to express my gratitude to all teachers and staffs of these programs.

Special thanks to Senior Lecturer Burenjargal Ulziiburen of School of Geology and Petroleum, Mongolian University of Science and Technology, and Putri Setiani and Masaoki Uno of Graduate School of Environmental Studies, Tohoku University, for warm encouragements.

I wish to express gratitude for the kind support of Ph.D. from all of the members in GeoMaterials and Energy Science, Tsuchiya Laboratory, Graduate School of Environmental Studies, Tohoku University.

And, my deep appreciation goes to my family who has understood and supported my study for long time.

REFERENCES

Akinfiev, N.N., and Diamond, L.W. (2009) A simple predictive model of quartz solubility in water-salt-CO_2 systems at temperatures up to 1000 °C and pressures up to 1000 MPa. *Geochimica et Cosmochimica Acta*, **73**, 1597–1608.

Alekseyev, V.A., Medvedeva, L.S., and Starshinova, N. P. (2009) Kinetics of Silica Precipitation on Quartz Seeds at 200–300 °C. *Geochemistry International*, **47**, 731–735.

Alekseyev, V.A., Medvedeva, L.S., Kochnova, L.N., and Tytyunnik, O.A. (2010) Mechanisms of silica precipitation from hydrothermal solutions: The effects of solution evaporations and quartz seed crystals. *Geochemistry International*, **48**, 178–182.

Alexander, G.B. (1957) The effect of particle size on the solubility of amorphous silica in water. *Journal of Physical Chemistry*, **61**, 1563–1564.

Anderko, A., and Pitzer, K.S. (1993a) Equation-of-state representation of phase equilibria and volumetric properties of the system NaCl-H_2O above 573 K. *Geochimica et Cosmochimica Acta*, **57**, 1657–1680.

Anderko, A., and Pitzer, K.S. (1993b) Phase equilibria and volumetric properties of the systems KCl-H_2O and NaCl-KCl-H_2O above 573 K. *Geochimica et Cosmochimica Acta*, **57**, 4885–4897.

Atkinson, B.K. (1984) Subcritical crack growth in geological materials. *Journal of Geophysical Research*, **89**, 4077–4114.

Bird, G., Boon, J., and Stone, T. (1986) Silica transport during steam injection into oil sands. 1. Dissolution and precipitation kinetics of quartz: New results and review of existing data. *Chemical Geology*, **54**, 69–80.

Bons, P.D. (2000) The formation of veins and their microstructures. *Stress, Strain and Structure,* Journal of the Virtual Explorer, **2**.

Bons, P.D. (2001) The formation of large quartz veins by rapid ascent of fluids in mobile hydrofractures. *Tectonophysics*, **336**, 1–17.

Brace, W.F., and Kohlstedt, D.L. (1980) Limits on lithospheric stress imposed by laboratory experiments. *Journal of Geophysical Research*, **85**, 6248–6252.

Brantley, S.L., Kubicki, J.D., and White, A.F. (2007) *Kinetics of Water-Rock Interaction.* Springer Inc., USA, 834 pp.

Byerlee, J.D. (1978) Friction of rocks. *Pure and Applied Geophysics*, **116**, 615–626.

Cady, S.L., and Farmer, J.D. (1996) Fossilization processes in siliceous thermal springs: trends in preservation along thermal gradients (proceedings). *the CIBA Foundation Symposium*, Wiley, Chichester, U.K., **202**, 150–173.

Carroll, S., Mroczek, E., Alai, M., and Ebert, M. (1998) Amorphous silica precipitation (60 to 120 °C): comparison of laboratory and field rates. *Geochimica et Cosmochimica Acta*, **62**, 1379–1396.

Connolly, J.A.D. (1997) Mid-crustal focused fluid movement: thermal consequences and silica transport. *Fluid flow and transport in rocks*, Chapman & Hall, London, 235–250.

Conrad, C.F., Icopini, G.A., Yasuhara, H., Bandstra, J.Z., Brantley, S.L., and Heaney, P.J. (2007) Modeling the kinetics of silica nanocolloid formation and precipitation in geologically relevant aqueous solutions. *Geochimica et Cosmochimica Acta*, **71**, 531–542.

Console, R., and Rossini, R. (1998) Non-double-couple microearthquakes in the geothermal field of larderello, central Italy. *Tectonophysics*, **289**, 203–220.

Cox, S.F. (1987) Antitaxial crack-seal vein microstructures and their relationship to displacement paths. *Journal of Structural Geology*, **9**, 779–787.

Cunneen, R., and Sillitoe, R.H. (1989) Paleozoic hot spring sinter in the Drummond Basin, Queensland, Australia. *Economic Geology*, **84**, 135–142.

Doi, N., Kato, O., Ikeuchi, K., Komatsu, R., Miyazaki, S., Akaku, K., and Uchida, T., (1998) Genesis of the plutonic-hydrothermal system around quaternary granite in the Kakkonda geothermal system, Japan. *Geothermics*, **27**, 663–690.

Duan, Z.H., Moller, N., and Weare, J.H. (1995) Molecular dynamics equation of state for nonpolar geochemical fluids. *Geochimica et Cosmochimica Acta*, **59**, 1533–1538.

Duan, Z.H., Moller, N., and Weare, J.H. (2003) Equation of state for the NaCl-H_2O-CH_4 system and the NaCl-H_2O-CO_2-CH_4 system: Phase equilibria and volumetric properties above 573 K. *Geochimica et Cosmochimica Acta*, **67**, 671–680.

Dunning, J.D., Petrovski, D., Schuyler, J., and Owens, A. (1984) The effects of aqueous chemical environments on crack propagation in quartz. *Journal of Geophysical Research*, **89**, 4115–4123.

Durney, D.W., and Ramsay, J.G. (1973) Incremental strains measured by syntectonic crystal growths. *Gravity and Tectonics*, Wiley, New York, 67–96.

Ehara, S., Fujimitsu, Y., Yamakawa, S., and Baba, H. (2001) Development of a Hydrothermal System by Conductive Cooling of the Heat Source A Case Study of Kakkonda Geothermal System, Japan. *Journal of the Geothermal Research Society of Japan*, **23**, 11–23.

Ellis, A.J., and Mahon, W.A.J. (1977) *Chemistry and Geothermal Systems*. Academic Press, New York, 392 pp.

Fisher, D.M., and Brantley, S.L. (1992) Models of quartz overgrowth and vein formation: deformation and episodic fluid flow in an ancient subduction zone. *Journal of Geophysical Research*, **97**, 20043–20061.

Fournier, R.O. (1991) The transition from hydrostatic to greater than hydrostatic fluid pressure in presently active continental hydrothermal systems in crystalline rock. *Journal of Geophysical Research Letters*, **18**, 955–958.

Fournier, R.O. (1999) Hydrothermal Processes related to movement of fluid from plastic into brittle rock in the magmatic–epithermal environment. *Economic Geology*, **94**, 1193–1211.

Fournier, R.O., and Potter, R.W.II. (1982) An equation correlating the solubility of quartz in water from 25 °C to 90 °C up to 10,000 bars. *Geochimica et Cosmochimica Acta*, **46**, 1969–1979.

Fournier, R.O., and Rowe, J.J. (1966) Estimation of underground temperatures from the silica content of water from hot springs and steam wells. *American Journal of Science*, **264**, 685–697.

Frank, F.C. (1965) On dilatancy in relation to seismic sources. *Reviews of Geophysics*, **3**, 485–503.

Freiman, S.W. (1984) Effects of Chemical Environments on Slow Crack Growth in Glasses and Ceramics, *Journal of Geophysical Research*, **89**, 4072–4076.

Frondel, C. (1962) Silica Minerals. *The System of Mineralogy of James Dwight Dana and Edward Salisbury Dana, Yale University, 1837–1892. 7th Edition*, Wiley, New York, **3**, 1813–1895.

Fujimoto, K., Takahashi, M., Doi, N., and Kato, O. (2000) High permeability of Quaternary granites in the Kakkonda geothermal area, northeast Japan (proceedings). *World Geothermal Congress 2000*, Kyushu, Japan.

Garrels, R.M. (1982) Chemical equilibrium in sedimentary systems. *Estudios Geologicos*, **38**, 289–294.

Graetsch, H. (1994) Structural characteristics of opaline and microcrystalline silica minerals. *Reviews in Mineralogy and Geochemistry*, **29**, 209–232.

Grasso, J.R. (1992) Mechanics of seismic instabilities induced by the recovery of hydrocarbons. *Pure and Applied Geophysics*, **139**, 507–534.

Griggs, D.T., and Blacic, J.D. (1965) Quartz-anomalous weakeness of synthetic crystals. *Science*, **147**, 292–295.

Grindley, G.W., and Browne, P.R.L. (1976) Structural and hydrological factors controlling the permeabilities of some hot-water geothermal fields (proceedings). *2nd U.N. Symposiumon Development and Use of Geothermal Resources*, New York, 377–386.

Guidry, S.A., and Chafetz, H.S. (2003) Siliceous shrubs in hot springs from Yellowstone National Park, Wyoming, U.S.A. *Canadian Journal of Earth Science*, **40**, 1571–1583.

Hanano, M. (1998) A Simple Model of a Two-Layered High-Temperature Liquid-Dominated Geothermal Reservoir as a Part of a Large-Scale Hydrothermal Convection System. *Transport in Porous Media*, **33**, 3–27.

Hanano, M., and Takanohashi, M. (1993) Review of recent development of the Kakkonda deep reservoir, Japan (proceedings). *Eighteenth Workshop on Geothermal Reservoir Engineering*, Stanford University, Stanford, California.

Hasegawa, A., N. Umino, and S. Hori (2001) Seismic activity and heterogeneity of the crust in the Nagamachi-Rifu fault zone. *Monthly Chikyu*, **263**, 313–320.

Herdianita, N.R., Browne, P.R.L., Rodgers, K.A., and Campbell, K.A. (2000) Mineralogical and textural changes accompanying ageing of silica sinter. *Mineralium Deposita*, **35**, 48–62.

Hinman, N.W., and Lindstrom, R.F. (1996) Seasonal changes in silica deposition in hot spring systems. *Chemical Geology*, **132**, 237–246.

Hiraga, T., Nishikawa, O., Nagase, T., Akizuki, M., and Kohlstedt, D.L. (2002) Interfacial energies for quartz and albite in politic schist. *Contributions to Mineralogy and Petrology*, **143**, 664–672.

Ikeuchi, K., Doi, N., Sakagawa, Y., Kamenosono, H., and Uchida, T. (1998) High temperature measurements in well WD-1a and the thermal structure of the Kakkonda geothermal system, Japan. *Geothermics*, **27**, 591–607.

Iler, R.K. (1973) Effect of adsorbed alumina on the solubility of amorphous silica in water. *Journal of Colloid and Interface Science*, **43**, 399–408.

Ingebritsen, S.E., and Manning, C.E. (2002) Diffuse fluid flux through orogenic belts: implications for the world ocean (proceedings). *the National Academy of Sciences, USA*, **99**, 113–116.

Ingebritsen, S.E., and Manning, C.E. (2010) Permeability of the continental crust: dynamic variations inferred from seismicity and metamorphism. *Geofluids*, **10**, 193–205.

Iwamori, H. (2007) Transportation of H_2O beneath the Japan arcs and its implications for global water circulation. *Chemical Geology*, **239**, 182–198.

Johnson, J.W., Oelkers, E.H., and Helgeson, H.C. (1992) SUPCRT92: a software package for calculating the standard modal thermodynamic properties of minerals, gases, aqueous species, and reactions from 1 to 5000 bar and 0 to 1000 °C. *Computers & Geosciences*, **18**, 899–947.

Jones, B., and Renaut, R.W. (2003) Petrography and genesis of spicular and columnar geyserite from the Whakarewarewa and Orakeikorako geothermal areas, North Island, New Zealand. *Canadian Journal of the Earth Sciences*, **40**, 1585–1610.

Jourdan, A.L., Vennemann, T.W., Mullis, L., Ramseyer, K., and Spiers C.J. (2009) Evidence of growth and sector zoning in hydrothermal quartz from Alpine veins. *European Journal of Mineralogy*, **21**, 219–231.

Kanisawa, S., Doi, N., Kato, O., and Ishikawa, K. (1994) Quaternary Kakkonda Granite underlying the Kakkonda Geothermal Field, Northeast Japan. *Journal of mineralogy, petrology and economic geology*, **89**, 390-407 (in Japanese).

Kasai, K., Sakagawa, Y., Komatsu, R., Sasaki, M., Akaku, K., and Uchida, T. (1998) The origin of hypersaline liquid in the quaternary Kakkonda granite, sampled from well WD-1a, Kakkonda geothermal system, Japan. *Geothermics*, **27**, 631–645.

Kato, O., Doi, N., and Muramatsu, Y. (1993) Neo-granitic pluton and geothermal reservoir at the Kakkonda geothermal field, Iwate prefecture, Japan. *Journal of the geothermal research society of Japan*, **15**, 41–57.

Kato, O., Doi, O., Sakagawa, Y., and Uchida, T. (1998) Fracture systematics in and around well WD-1a Kakkonda geothermal field, JAPAN. *Geothermics*, **27**, 609–629.

Kirby, S.H. (1980) Tectonic stress in the lithosphere: Constraints provided by the experimental deformation of rock. *Journal of Geophysical Research*, **85**, 6353–6363.

Kirschner, D.L., Sharp, Z.D., and Masson, H. (1995) Oxygen-isotope thermometry OF quartz-calcite veins - unraveling the thermal-tectonic history of the subgreenschist facies morcles nappe (Swiss-Alps). *Geological Society of America Bulletin*, **107**, 1145–1156.

Koshiya, S., Okami, K, Kikuchi, Y., Hirayama, T., Hayasaka, Y., Uzawa, M., Honma, K., and Doi, N. (1993) Fracture System Developed in the Takinoue Geothermal Area. *Journal of the Geothermal Research Society of Japan*, **15**, 109–139 (in Japanese).

Laidler, K.J. (1987) *Chemical Kinetics*. Harper & Row, Publishers, Inc., New York, 490 pp.

Lasaga, A.C. (1998) *Kinetic Theory in the Earth Sciences*. Princeton University Press, 811 pp.

Lowell, R.P., Van Cappellen, P., and Germanovich, L.N. (1993) Silica precipitation in fractures and the evolution of permeability in hydrothermal upflow zones. *Science*, **260**, 192–194.

Lynne, B.Y., Campbell, K.A., Moore, J., and Browne, P.R.L. (2008) Origin and evolution of the Steamboat Springs siliceous sinter deposit, Nevada, USA. *Sedimentary Geology*, **210**, 111–131.

Manning, C.E. (1994) The solubility of quartz in H_2O in the lower crust and upper mantle. *Geochimica et Cosmochimica Acta*, **58**, 4831–4839.

Matsushima, J., Okubo, Y., Rokugawa, S., Yokota, T., Tanaka, K., Tsuchiya, T., and Narita, N. (2003) Seismic reflector imaging by prestack time migration in the Kakkonda geothermal field, Japan. *Geothermics*, **32**, 79–99.

Mason, B., and Moore, C.B. (1982) *Principles of Geochemistry*. John Wiley, New York, 344 pp.

Meissner, R., and Strehlau, J. (1982) Limits of stresses in continental crusts and their relation to the depth-frequency distribution of shallow earthquakes. *Tectonics*, **1**, 73–89.

Mitsuhata, Y., Ogawa, Y., Mishina, M., Kono, T., Yokokura, T., and Uchida, T. (2001) Electromagnetic heterogeneity of the seismogenic region of 1962 M6.5 Northern Miyagi Earthquake, northeastern Japan. *Geophysical Research Letter*, **28**, 4371–4374.

Mizutani, S. (1970) Silica minerals in early stage of diagenesis. *Sedimentology*, **15**, 3–4.

Miyoshi, N., Yamaguchi, Y., and Makino, K. (2005) Successive zoning of Al and H in hydrothermal vein quartz. *American Mineralogist.* **90**, 310–315.

Monecke, T., Kempe, U., and Götze, J. (2002) Genetic significance of the trace element content in metamorphic and hydrothermal quartz: A reconnaissance study. *Earth and Planetary Science Letters*, **202**, 709–724.

Morita, T., Kusano, K., Ochiai, H., Saitow, K., and Nishikawa, K. (2000) Study of inhomogeneity of supercritical water by small-angle x-ray scattering. *The Journal of Physical Chemistry*, **112**, 4203–11.

Morohashi, K., Okamoto, A., Satish-Kumar, M., and Tsuchiya, N. (2008) Variations in stable isotope compositions ($\delta^{13}C$, $\delta^{18}O$) of calcite within exhumation-related veins

from the Sanbagawa metamorphic belt. *Journal of Mineralogical and Petrological Sciences*, **103**, 361–364.

Muramatsu, Y., Komatsu, R., Sawaki, T., Sasaki, M., and Yanagiya, S. (2000) Geochemical study of fluid inclusions in anhydrite from the Kakkonda geothermal system, northeast Japan. *Geochemical Journal*, **34**, 175–193.

Muraoka, H., Uchida, T., Sasada, M., Yagi, M., Akaku, K., Sasaki, M., Yasukawa, K., Miyazaki, S., Doi, N., Saito, S., Sato, K., and Tanaka, S. (1998) Deep geothermal resources survey program: Igneous, metamorphic and hydrothermal processes in a well encountering 500 °C at 3729 m depth, Kakkonda, Japan. *Geothermics*, **27**, 507–534.

Nakajima, J., Matsuzawa, T., and Hasegawa, A. (2001) Seismic imaging of arc magma and fluids under the central part of northeastern Japan. *Tectonophysics*, **341**, 1–17.

Neagu, R.C., Tinivella, U., Volpi, V., Rebesco, M., and Camerlenghi, A. (2009) Estimation of biogenic silica contents in marine sediments using seismic and well log data: Sediment Drift 7, Antarctica. *International Journal of Earth Sciences*, **98**, 839–848.

NEDO (1996) *Summary of Deep-Seated Geothermal Resources Survey, FY 1995*. New Energy and Industrial Technology Development Organization, Tokyo, Japan, 887 pp. (in Japanese).

Newton, R.C., and Manning, C.E. (2008) Solubility of corundum in the system Al_2O_3-SiO_2-H_2O-NaCl at 800 °C and 10 kbar. *Chemical Geology*, **249**, 250-261.

Nicholson, R. (1991) Vein morphology, host rock deformation and the origin of the fabrics of echelon mineral veins. *Journal of Structural Geology*, **13**, 635–641.

Nishida, I., Shimada, Y., Saito, T., Okaue, Y., and Yokoyama, T. (2009) Effect of aluminum on the deposition of silica scales in cooling water systems. *Journal of Colloid and Interface Science*, **335**, 18–23.

Nur, A., and Walder, J. (1990) Time-dependent hydraulics of the Earth's crust. *The Role of Fluids in Crustal Processes*. National Academy Press. Washington, D.C., 113–127.

Ohmi, S. and Obara, K. (2002) Deep Low-Frequency Earthquakes beneath the Focal Region of the Mw 6.7 2000 Western Tottori Earthquake, *Geophysical Research Letters*, **29**, 1807.

Oliver, N.H.S., and Bons, P.D. (2001) Mechanisms of fluid flow and fluid–rock interaction in fossil metamorphic hydrothermal systems inferred from vein–wallrock patterns, geometry and microstructure. *Geofluids*, **1**, 137–162.

Okada, T., Umino, N., and Hasegawa, A. (2010) Deep structure of the Ou mountain range strain concentration zone and the focal area of the 2008 Iwate-Miyagi Nairiku earthquake, NE Japan-seismogenesis related with magma and crustal fluid. *Earth Planets Space*, **62**, 347–352.

Okamoto, A., Kikuchi, T., and Tsuchiya, N. (2008) Mineral distribution within polymineralic veins in the Sanbagawa belt, Japan: implications for mass transfer during vein formation. *Contributions to Mineralogy and Petrology*, **156**, 323–336.

Okamoto, A., and Sekine, K. (2011) Textures of syntaxial quartz veins synthesized by hydrothermal experiments. *Journal of Structural Geology*, **33**, 1764–1775.

Okamoto, A., and Tsuchiya, N. (2009) Velocity of vertical fluid ascent within vein-forming fractures. *Geology,* **37**, 563–566.

Okamoto, A., Saishu, H., Hirano, N., and Tsuchiya, N. (2010) Mineralogical and textural variation of silica minerals in hydrothermal flow-through experiments: Implications for quartz vein formation. *Geochimica et Cosmochimica Acta*, **74**, 3692–3706.

Parry, W.T. (2000) *ASME International Steam Tables for Industrial Use*, American Society of Mechanical Engineers, 283 pp.

Parks, G.A. (1984) Surface and interfacial energy of quartz. *Journal of Geophysical Research*, **89**, 3997–4008.

Paterson, M.S., and Weaver, C.W. (1970) Deformation of Polycrystalline MgO Under Pressure. *Journal of the American Ceramic Society*, **53**, 463–471.

Phillips, W.J. (1972) Hydraulic fracturing and mineralisation. *Journal of the Geological Society of London*, **128**, 337–359.

Reed M. H. (1982) Calculation of multicomponent chemical equilibria and reaction processes in systems involving minerals, gases, and an aqueous phase. *Geochimica et Cosmochimica Acta*, **46**, 513–528.

Reed, M.H. (1998) Calculation of simultaneous chemical equilibria in aqueous-mineral-gas systems and its application to modeling hydrothermal processes, *Techniques in Hydrothermal Ore Deposits Geology*, *Reviews in Economic Geology*, **10**, 109–124.

Reed, M.H., Spycher, N.F., and Palandri, J. (2010) *SOLVEQ-XPT: A Computer Program for Computing Aqueous-Mineral-Gas Equilibria*, Department of geological sciences, University of Oregon, 43 pp.

Renders, P.J.N., Gammons, C.H., and Barnes, H.L. (1995) Precipitation and dissolution rate constants for cristobalite from 150 to 300 °C. *Geochimica et Cosmochimica Acta*, **59**, 77–85.

Rimstidt, J.D., and Barnes, H.L. (1980) The kinetics of silica–water reactions. *Geochimica et Cosmochimica Acta*, **44**, 1683–1699.

Robie, R.A., Hemingway, B.S., and Fisher, J.R. (1978) Thermodynamic properties of minerals and related substances at 298.15 °K and 1 bar (10^5 Pascals) pressure and at higher temperatures. *Journal of Colloid and Interface Science*, **71**, 533–559.

Rothbaum, H.P., and Rohde, A.G. (1979) Kinetics of silica polymerization and deposition from dilute-solutions between 5-degrees-C and 180-degrees-C. *Journal of Colloid and Interface Science*, **71**, 533–559.

Rudnick, R.L., and Gao, S. (2005) Composition of the continental crust. *The Crust. Treatiseon Geochemistry*, Elsevier, Amsterdam, **3**, 1–64.

Rusk, B., and Reed, M.H. (2002) Scanning electron microscope–cathodoluminescence analysis of quartz reveals complex growth histories in veins from the Butte porphyry copper deposit, Montana. *Geology*, **30**, 727–730.

Rusk, B., Heather, A., Lowers, H.A., and Reed, M.H. (2008) Trace elements in hydrothermal quartz: Relationships to cathodoluminescent textures and insights into vein formation. *Geology*, **36**, 547–550.

Sasaki, M., Fujimoto, K., Sawaki, T., Tsukamoto, H., Kato, O., Komatsu, R., Doi, N., and Sasada, M. (2003) Petrographic features of a high-temperature granite just newly solidified magma at the Kakkonda geothermal field, Japan. *Journal of Volcanology and Geothermal Research*, **121**, 247–269.

Scholz, C.H. (1968) Microfracturing and the inelastic deformation of rock in compression, *Journal of Geophysical Research*, **73**, 1417–1432.

Scholz, C.H. (2002) *The Mechanics of Earthquakes and Faulting (2nd edition).* Cambridge University Press, Cambridge, 471 pp.

Schröder, H.C., Wang, X.H., Tremel, W., Ushijima, H., and Müller, W.E.G. (2008) Biofabrication of biosilica-glass by living organisms. *Natural Product Reports,* **25**, 455–474.

Sherlock, R.L., Tosdal, R.M., Lehrman, N.J., Graney, J.R., Losh, S., Jowett, E.C., and Kesler, S.E. (1995) Origin of the McLaughlin Mine sheeted complex: metal zoning, fluid inclusion and isotopic evidence. *Economic Geology*, **90**, 2156–2181.

Sibson, R.H. (1982) Fault zone models, heat flow, and the depth distribution of earthquakes in the continental crust of the United States. *Bulletin of the Seismological Society of America,* **68**, 1421–1448.

Sibson, R.H. (1990) Conditions for fault-valve behaviour. *Deformation Mechanisms, rheology and Tectonics*. Geological Society Special Publication, **54**, 15–28.

Sibson, R.H. (1992) Implications of fault-valve behavior for rupture nucleation and recurrence. *Tectonophysics,* **211**, 283–293.

Siever, R. (1962) Silica solubility 0°–200 °C and the diagenesis of aqueous sediment. *Journal of Geology*, **70**, 127–150.

Shimamoto, T. (1994) Rheology of lithosphere: Current status and future perspectives. *The journal of the Tectonic Research Group of Japan*, **39**, 147–152 (in Japanese).

Smith, D.K. (1998) Opal, cristobalite, and tridymite: Noncrystallinity versus crystallinity, nomenclature of the silica minerals and bibliography. *Powder Diffraction***, 13**, 2–19.

Steefel, C.I., and Van Cappellen, P. (1990) A new kinetic approach to modeling water–rock interaction: The role of nucleation, precursors, and Ostwald ripening. *Geochimica et Cosmochimica Acta.*, **54**, 2657–2677.

Swanson, P.L. (1984) Subcritical crack growth and other time- and environment-dependent behavior in crustal rocks. *Journal of Geophysical Research*, **89**, 4137–4152.

Takashima, I., Honda, S., and Tetsu Wada, T. (1987) Geothermal History and Hydrothermal System of the Kakkonda Omatsukurazawa and Adjacent Areas, Hachimantai Geothermal Field, Northeast Japan Application of Thermoluminescence Dating of Altered Rocks to Geothermal Exploration. *Journal of the Geothermal Research Society of Japan*, **9**, 43–55 (in Japanese).

Tamanyu, S., and Lanphere, M.A. (1983) Volcanic and geothermal history at the Hachimantai geothermal field in Japan-on the basis of K-Ar age. *Journal of Geological Society of Japan*, **89**, 501–510.

Tamanyu, S., and Suto, S. (1978) Stratigraphy and geochronology of Tamagawa welded tuff in the western part of Hachimantai, Akita Prefecture. *Bulletin of the Geological Survey of Japan*, **29**, 159–172 (in Japanese).

Tosha, T., Sugihara, M., and Nishi, Y. (1998) Revised hypocenter solutions for microearthquakes in the Kakkonda geothermal field, Japan. *Geothermics*, **27**, 553–571.

Trewin, N.H. (1994) Depositional environment and preservation of biota in the Lower Devonian hot-springs of Rhynie, Aberdeenshire, Scotland. *Transactions of the Royal Society of Edinburgh-Earth Sciences*, **84**, 433–442.

Tsuchiya, N., and Hirano, N. (2007) Chemical reaction diversity of geofluids revealed by hydrothermal experiments under sub- and supercritical states. *Island Arc*, **16**, 6–15.

Urai, J.L., Williams, P.F., and van Roermund, H.L.M. (1991) Kinematics of crystal growth in syntectonic fibrous veins. *Journal of Structural Geology*, **13**, 823–836.

Uriz, M.J., Turon, X., and Becerro, M.A. (2000) Silica deposition in demosponges: spiculogenesis in Crambe crambe. *Cell and Tissue Research*, **301**, 299–309.

Volpi, V., Camerlenghi, A., Hillenbrand, C.D., Rebesco, M., and Ivaldi, R. (2003) Effects of biogenic silica on sediment compaction and slope stability on the Pacific margin of the Antarctic Peninsula. *Basin Research*, **15**, 339–363.

Walder, J., and Nur, A. (1984) Porosity reduction and crustal pore pressure development. *Journal of Geophysical Research*, **89**. 11539–11548.

Walter, M.R. (1976) Hot-springs sediments in Yellowstone National Park. *Stromatolites*. Elsevier, Amsterdam, 790 pp.

Walther, J.V., and Helgeson, H.C. (1977) Calculation of the thermodynamic properties of aqueous silica and the solubility of quartz and its polymorphs at high pressures and temperatures. *American Journal of Science*, **277**, 1315–1351.

Walther, J.V., and Orville, P.M. (1983) The extraction-quench technique for determination of the thermodynamic properties of solute complexes: Application to quartz solubility in fluid mixtures. *American Mineralogist*, **68**, 731–741.

Weaver, J.C., Pietrasanta, L.I., Hedin, N., Chmelka, B.F., Hansma, P.K., and Morse, D.E. (2003) Nanostructural features of demosponge biosilica. *Journal of Structural Biology*, **144**, 271–281.

Weis, P., Driesner, T., and Heinrich, C.A. (2012) Porphyry-copper ore shells form at stable pressure–temperature fronts within dynamic fluid plumes. *Science*, **338**, 1613–1616.

White, D.E., Brannock, W.W., and Murata, K.J. (1956) Silica in hot-spring waters. *Geochimica et Cosmochimica Acta*, **10**, 27–59.

White, S.P., and Mroczek, E.K. (1998) Permeability changes during the evolution of a geothermal field due to the dissolution and precipitation of quartz. *Transport in porous media*, **33**, 81–101.

White, N.C., Wood, D.G., and Lee, M.C. (1989) Epithermal sinters of Paleozoic age in north Queensland, Australia. *Geology*, **17**, 718–722.

Wilkinson, J.J., Boyce, A.J., Earls, G., and Fallick, A.E. (1999) Gold remobilization by low-temperature brines: Evidence from the Curraghinalt gold deposit, northern Ireland. *Economic Geology and the Bulletin of the Society of Economic Geologists*, **94**, 289–296.

Williams, L.A., and Crerar, D.A. (1985) Silica diagenesis; II, General mechanisms. *Journal of Sedimentary petrology*, **55**, 312–321.

Williams, L.A., Parks, G.A., and Crerar, D.A. (1985) Silica diagenesis; I, Solubility controls. *Journal of Sedimentary petrology*, **55**, 301–311.

Yanagisawa, N., Matsunaga, I., Sugita, H., Sato, M., and Okabe, T. (2008) Temperature-dependent scale precipitation in the Hijiori Hot Dry Rock system, Japan. *Geothermics*, **37**, 1–18.

Yokoyama, T., Sato, Y., Maeda, Y., Tarutani, T., and Itoi, R. (1993) Siliceous deposits formed from geothermal water: I. The major constituents and the existing states of iron and aluminum. *Geochemical Journal*, **27**, 375–384.

Zoback, M.D., and Harjes, H-P. (1997) Injection-induced earthquakes and crustal stress at 9 km depth at the KTB deep drilling site, Germany. *Journal of Geophysical Research*, **102**, 18477–18491.

PUBLISHED PAPERS

Okamoto, A., Saishu, H., Hirano, N., and Tsuchiya, N. (2010) Mineralogical and textural variation of silica minerals in hydrothermal flow-through experiments: Implications for quartz vein formation. *Geochimica et Cosmochimica Acta*, **74**, 3692–3706.

Saishu, H., Okamoto, A., and Tsuchiya, N. (2012) Mineralogical variation of silica induced by Al and Na in hydrothermal solutions. *American Mineralogist*, **97**, 2060–2063.

Saishu, H., Okamoto, A., and Tsuchiya, N. (in press) The significance of silica precipitation on the formation of the permeable–impermeable boundary within Earth's crust. *Terra Nova*.